University of Alberta

Numerical Study of Induced Charge Electroosmosis
And
Its Applications

by

Mranal Jain

A thesis submitted to the Faculty of Graduate Studies and Research
in partial fulfillment of the requirements for the degree of

Doctor of Philosophy
in
Chemical Engineering

Chemical and Materials Engineering

Spring 2011
Edmonton, Alberta

Examining Committee

Dr. Tony Yeung (Supervisor)
[Chemical & Materials Engineering, University of Alberta, Canada]

Dr. Krishnaswamy Nandakumar (Supervisor)
[Chemical Engineering, Louisiana State University, USA]
[Professor Emeritus, Chemical & Materials Engineering, University of Alberta, Canada]

Dr. Neda Nazemifard
[Chemical & Materials Engineering, University of Alberta, Canada]

Dr. Sushanta K. Mitra
[Mechanical Engineering, University of Alberta, Canada]

Dr. Shramik Sengupta
[Biological Engineering, University of Missouri, USA]

Dedicated
To
The Loving Memory of My Mother

(Late Mrs. Rekha Jain)

Abstract

Lab-on-a-chip (LOC) devices promises automation of conventional bio-analytical laboratory tests with little reagent/ sample usage. These devices however require pumping and mixing of samples/reagents in order to attain desired functionalities. Therefore, study of fluid flow at micron length scales, microfluidics, is critical for LOC devices. As the dimensions shrink, the relative importance of surface forces /effects increases with respect to volumetric forces. Due to smaller length scales, there exist several challenges such as: (a) mixing and pumping of fluids where conventional (macroscopic) techniques are not useful or applicable; (b) identifying innovative techniques for fluid manipulation which scales appropriately with the device dimensions. A variety of strategies have been developed for microscopic fluid manipulation. However, electrokinetics is the preferred flow driving mechanism owing to its non-mechanical nature and ease of flow control. On the downside, the plug flow type profile in electrokinetic flow results in poor mixing conditions. Mixing is a key step in realizing fast analysis time in many bio-chemical, biological and detection applications of LOC devices.

This dissertation deals with the study of induced charge electro-osmosis (ICEO) and its possible applications in microfluidic devices. ICEO is a non-linear variant of classical electrokinetics and deals with electrically induced fluid flow over polarizable surfaces. Initially, theoretical models were developed for induced charge electro-osmotic (ICEO) flow and validated against reported analytical results. A geometrically simple design is proposed for efficient micromixing using ICEO flows. The proposed device is further optimized using NURBS based shape optimization techniques. The transition of optimal shapes from a diffusive regime to an ICEO-dominant regime was demonstrated while identifying rectangular shape and right triangle shape as optimal for diffusive and ICEO dominant regime respectively. For comparison of various parallel flow micro-mixers, a new mixing performance index was developed based on normalized residence time. The proposed comparative mixing index (CMI) is utilized for characterization of various micro-mixing techniques and subsequently, limitations associated with existing mixing performance indicators were identified. Lastly, a concentration gradient generator device is designed based on ICEO flow. The proposed device was found to be superior to existing designs in terms of dynamic controllability due to ICEO flow characteristics. In general, this study demonstrates the use of ICEO for inducing localized variations in fluid flow and utilizes such tailored flow characteristics for attaining specific tasks such as mixing and gradient generation. The presented methodology would be useful in designing micro-devices as well as optimizing their performance.

Acknowledgements

I would like to express my sincere thanks and gratefulness to my academic supervisors Dr. Krishnaswamy Nandakumar and Dr. Tony Yeung during my doctoral research work. I would like to thank my supervisors for consistent encouragement and technical advice throughout this study. I am also thankful to both of them for being patient with me, especially during my unproductive times and for allowing me to learn from my mistakes. I have gained technical knowledge, self-confidence and maturity under their friendly guidance which is surely going to help me a lot in my future endeavors.

I was also fortunate to have a short stint as a research visitor in Dr. Hsueh-Chia Chang's Lab at the 'Center of Microfluidics and Medical Diagnostics', University of Notre Dame. I am extremely thankful to Dr. Hsueh-Chia Chang (University of Notre Dame) for supervising my research during my stay at University of Notre Dame. I would like to express my gratitude to Dr. Subir Bhattacharjee (Mechanical Engineering, University of Alberta) for technical discussions related to classical electrokinetics. Mr. Bob Barton and his team deserve special thanks for providing computational resource support throughout this study. I would also like to acknowledge the help and encouragement I received from my colleagues: Misha, Ali, Saeid, Veeramani, Srinath, Kushagra and other research group members. I enjoyed technical and non-technical discussions with all of them.

I thank Dr. Ram Mehta & family, Dr. Dinesh Rai & Family, and Mr. Mahendra Thaker & family for extending their help (especially during my initial days), love and support. I will always relish the friendliness and affection I received from Mridul, Charu, Japan, Sejal, Ashish, Sarthak, Jigar, Amit Jhala, Amit Singh, Rajesh, Hemant, Salokha, Ketul, Kruti, Hetal, Raghvendra, Rahul, Nischala, Pratik, Hari, Shankar, Varma and many more. I am extremely thankful to everyone for all the wonderful time we spent together.

I thank my whole family for their support at all times. My special thanks to my parents (Mr. Kailash Chand Jain and Late Mrs. Rekha Jain) and my brother (Mr. Amit Jain), without their love and efforts I would have never made up to this point. I would like to express my immeasurable gratitude to my spouse, Ritika Bhansali, for her endless love and unconditional support. I am especially thankful to her for taking excellent care of our lovely son, Aarush Jain.

Finally, I would like to acknowledge the financial assistance (funding, awards and scholarships) provided by my supervisors, Natural Sciences and Engineering Research Council of Canada (NSERC), Faculty of Graduate Studies and Research (FGSR), Graduate Students Association (GSA) and Chemical & Materials Engineering (CME) department during this study.

Table of Contents

List of Figures

List of Tables

List of Abbreviations

ACEO	AC Electroosmosis
CMI	Comparative Mixing Index
DEP	Dielectrophoresis
EDL	Electric Double Layer
EK	Electrokinetic(s)
EO / EOF	Electroosmosis / Electroosmotic Flow
EP	Electrophoresis
FCEO	Fixed Charge Electroosmosis
GA	Genetic Algorithms
ICEK	Induced Charge Electrokinetic(s)
ICEO / ICEP	Induced Charge Electroosmosis / Electrophoresis
LOC	Lab-On-a-Chip
MEMS	Micro-Electro-Mechanical Systems
MF	Microfluidics
NP	Nernst Planck
NS	Navier Stokes
NURBS	Non-Uniform Rational Basis Spline
PB	Poisson Boltzmann
PNP	Poisson Nernst Planck
μ-TAS	Micro Total Analysis System

Chapter 1

Introduction

1.1 Miniaturization and Lab-on-a-Chip (LOC) Devices

Miniaturization is the process of developing small-scale products, devices or components (mechanical, electrical etc.) with similar or better functionality as of their macroscopic counterparts. The advent of micro-electronics is one of the most successful examples of miniaturization. Electronic industry has delivered more efficient, reduced weight and cost-effective portable devices such as cell phones, computers, power supplies etc using micro-fabrication techniques. The ability to miniaturize mechanical/electrical components is the basis of MEMS (micro-electro-mechanical systems). The most commercially noted MEMS device is used in the automobile industry for airbag activation. The MEMS device incorporates electromechanical and electronic components on a silicon wafer for physical impact detection. The concept of miniaturization has been further extended to chemical, biological and bio-medical applications and such devices are termed as Lab-on-a-Chip (LOC) devices.

Lab-on-a-Chip (LOC) devices, also known as micro-total analysis systems (μ-TAS), are miniaturized devices capable of carrying out conventional analytical laboratory tests (Harrison et al. 1993; Manz et al. 1993). Like their larger counterparts, however, LOC systems require integration of various sub-components such as pumps, mixers, reactors, and dilution chambers. A typical schematic of a LOC device is shown in Figure 1, where different functional units are connected through microchannels. Such devices offer significant benefits over traditional macroscopic counterparts in terms of reduced size, sample/reagent usage and analysis time.

Lab-on-a-Chip has been identified as promising technology for applications in clinical diagnostics, environmental and defense monitoring, biomedical applications, chemical synthesis, drug delivery, drug discovery etc (Whitesides 2006; Dittrich and Manz 2006; Manz and Eijkel 2001; Sanders and Manz 2000; Chang 2006; deMello 2006; Janasek et al. 2006; Craighead 2006). LOC technology can revolutionize the healthcare systems by providing accessible, inexpensive, rapid diagnostic point-of-care devices. In particular, such point-of-care diagnostic systems will eliminate the need of trained technicians and expensive instrumentation and will be highly useful in developing countries as well as in remote conditions (Yager et al. 2006).

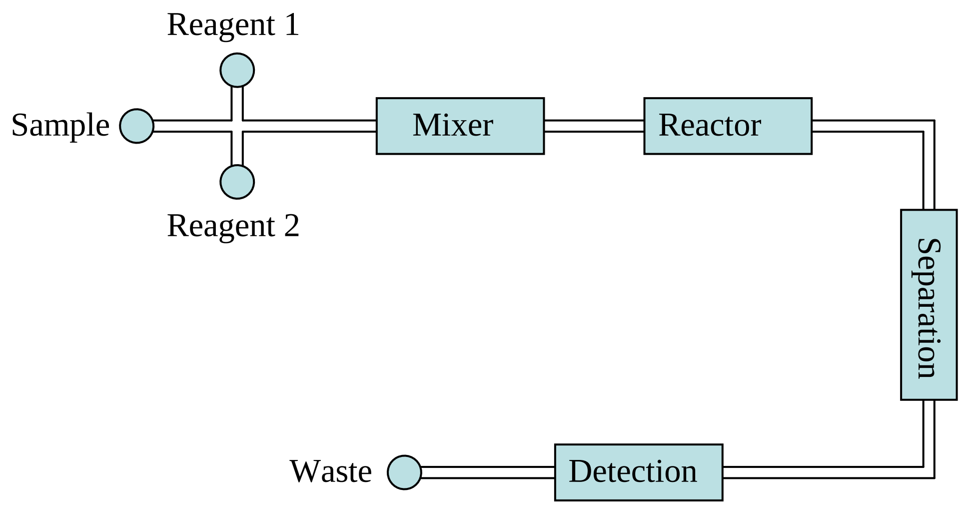

Figure 1.1: Schematic of typical Lab-on-a-Chip (LOC) device with various sub-components.

The development of LOC devices requires convergence of various disciplines such as chemistry, biology, medicine, material science and engineering (chemical, mechanical, electrical etc.). As these devices employ fluid flow in microscopic conditions, the study of fluid physics in miniaturized geometries—a field known as microfluidics—has become central to the development of LOC devices. With advances in micro-fabrication technologies (McDonald et al. 2000; Whitesides and Stroock 2001; Sia and Whitesides 2003), it is now possible to conduct microfluidic experimental studies in complex geometries. In addition, computational modeling is also instrumental in advancing the understanding of transport phenomena within the miniaturized devices as microscopic experimentation is non trivial and requires expensive instrumentation techniques.

For illustration purpose, I will briefly outline some examples of microfluidic devices/ miniaturization which have been found to be advantageous over their macroscopic counterparts. The first example is a microfluidic device devised for the forensic analysis of sexual assault samples (Norris et al. 2009). The current lab protocols take 4-8 hours, sometimes even 12 hours to separate male sperm cells and female epithelial cells from a sexual assault sample. The report claimed that such separation could be done in less than 15 minutes using microfluidic device based on acoustic differential extraction technique. Another study claims the use of 15 fold lesser reagent (enzyme in this case) and 30 times faster results than traditional lab methods in an enzymatic glucose assay study based on electrokinetically driven microfluidic device (Atalay et al. 2009). Various such examples of microfluidic devices for biological, environmental, biomedical and other applications are frequently reported in leading research journals such as *Nature, Science, Lab on a Chip, Analytical Chemistry* etc. Several groups are actively engaged in microfluidics research around the globe and it has been identified as one of ten technologies capable of revolutionizing the world (Tabeling 2005).

Another interesting concept is the development of micro-devices for traditional chemical engineering process e.g. chemical synthesis. The research efforts have already begun and results are promising due to favorable heat and mass transfer characteristics at smaller length scales. For example, Hessel et al. (2004) utilized micromixers within a micro-reactor for *Phenyl Boronic Acid* process and found 25 % higher yield, higher selectivity and less energy consumption compared to stirred tank process. While various studies have shown promising results for chemical synthesis on small scale, it is still impossible to miniaturize a mass chemical production facility due to sheer production volume. Massive parallelization of miniaturized systems (*numbering up*) is suggested as a possibility but integration and assembly of such system remains a challenge. If it can be achieved, it could possibly be the next milestone for miniaturization and present many advantages such as reduced cost of transportation, reduced risk of contamination, higher process safety etc (Tabeling 2005).

1.2 Role of Microfluidics (MF)

LOC devices require fluid manipulation at microscopic scale. Irrespective of the type of applications, study of microfluidics is critical for pumping, mixing, separation, particle manipulation etc. in LOC devices (Whitesides 2006). Although miniaturization offers various advantages such as reduced analysis time, reduced sample/ reagent usage; there are various challenges that need to be addressed in terms of fluid flow (Stone and Kim 2001). Due to the associated smaller length scales, the fluid flow in LOC devices is in laminar flow regime resulting in poor mixing conditions. Unlike macroscopic systems, rotating parts such as stirrers/ impellers cannot be employed for enhancing mixing in LOC devices due to cleavage and fabrication issues. Such challenges can be dealt by innovative fluid manipulation techniques and by tailoring flow patterns/characteristics within the micro-devices.

As we go down to smaller length scales, the relative importance of surface forces/effects increases as compared to volumetric forces. Therefore, another major consideration in LOC devices is the identification of an appropriate flow driving method. Various driving forces have been utilized for manipulating microfluidic flow such as pressure gradients, electric potential gradients, capillarity, surface tension gradients etc (Stone et al. 2004).

The most commonly used driving mechanism are pressure driven flow and electro-kinetically driven flow. The conventional pressure driven flow is well studied but has limitations in terms of integration with the LOC device. Typically syringe pump is utilized for pressure driven micro-fluid flow which needs to be hand connected and requires handling of leaky interconnects (Chang and Yang 2007). Moreover, the quadratic dependence of velocity on channel width/ radius results in lower velocities as dimensions shrink. On the other hand, electro-kinetics (EK) has been identified as the most viable option for microfluidic applications in LOC devices (Chang 2006; Stone et al. 2004). Electrokinetic pumping requires no external mechanical moving parts and usually velocity is independent of channel dimensions (details are outlined in next chapter). Electro-kinetic flow can be easily controlled through embedded electrodes together with an inserted power supply (or battery for portable systems) within the device. By suitable positioning of embedded electrodes, localized variations in flow can be attained. On the downside, high applied potentials are required for some applications owing to the linear dependence of velocity on electric field. Other problems include handling of electrochemical reactions at electrode and variations in surface properties due to pH change (Squires and Quake 2005). Another variant of electro-kinetics is induced charge electro-osmosis (ICEO), the study of electrokinetic flows over polarizable surfaces. ICEO could be used to attain high velocities using low applied potentials, since velocities scales quadratically with electric field in ICEO (Squires and Bazant 2004; Bazant and Squires 2004). Further, the induced surface charge could also be tuned/ controlled with electric field. Due to these advantages, ICEO has been considered as an attractive option for LOC devices (Squires 2009).

1.3 Scope and organization of dissertation

The primary goal of this research is to gain fundamental understanding of induced charge electro-kinetic (ICEK) flows through extensive mathematical modeling. I would further like to utilize the understanding of ICEK phenomenon to design innovative and novel micro-devices for different applications. Another objective is to develop specific design principles so as to guide experimentalists/ design engineers engaged in micro-fluidic research towards better/ optimal designs, thereby reducing additional costs, time and effort spent on designing micro-scale experiments/ devices.

The organization of this dissertation is as follows; the next chapter presents the theory for classical electro-kinetics (EK) and induced charge electro-kinetics (ICEK) including definitions, mathematical models with their limitations and assumptions. In chapter 3, a novel micro-mixer design based on ICEK flows is presented. The analysis presents the mixing mechanism and effect of various design parameters on mixing performance. The proposed micro-mixer design is further optimized using NURBS (Non-Uniform Rational B-Spline curves) based shape optimization technique in chapter 4. This part of the dissertation identifies optimal obstacle shape in ICEO mixer for diffusive as well as convection dominant regimes. Next chapter revisits the performance evaluation criteria for micro-mixers and proposes a new performance indicator based on residence time normalization for parallel flow type of micro-mixers. Several case studies are presented in chapter 5 which clearly demonstrate the usefulness of proposed mixing index over existing measures of micro-mixing performance. In chapter 6, ICEO based novel design is presented to generate concentration gradient for biological applications. Various parametric studies are presented to demonstrate the dynamic controllability aspect of the proposed design. In Chapter 7, the contributions of this dissertation are summarized and recommendations are made for future research.

Chapter 2

Basics of Electrokinetics

2.1 Introduction

Electrokinetics (EK) deals with the study of fluid flow or particle motion generated due to an interaction between electric field and charged surface in presence of a charged fluid such as electrolyte solution. The most routinely used electrokinetic processes are electro-osmosis (EO), electrophoresis (EP) and dielectrophoresis (DEP). The theory of electrokinetic transport was developed earlier for studying colloids and flow in porous system. There has been renewed interest in electrokinetics due to its applications in microfluidic devices.

Most of the microfluidic applications utilize the following electrokinetic phenomena; (a) electroosmosis: movement of ionized liquid relative to the stationary charged surface by an applied electric field., (b) electrophoresis: motion of the charged particle relative to the stationary ionized liquid by an applied electric field and (c) dielectrophoresis: motion of polarized particles subjected to non-uniform electric field. In addition to above phenomenon, I will also describe some variants of classical electrokinetics such as induced charge electroosmosis (ICEO) and AC electroosmosis (ACEO) which deals with the fluid flow generated due to the electrically induced charge on polarizable surface. Other electrokinetic phenomena such as streaming potential (inverse of electro-osmosis i.e. electric field created by the motion of ionized fluid along stationary charged surfaces) and sedimentation potential (inverse of electrophoresis i.e. electric field created by the motion of charged particles relative to a stationary liquid) are not commonly applied to microfluidic device. Hence streaming potential and sedimentation potential are not discussed here but can be related to electro-osmosis and electrophoresis respectively using Onsager symmetries (Masliyah and Bhattacharjee 2006).

The electric double layer (EDL) is the basis of electrokinetic transport and will be reviewed in the next section. Next, we will discuss the detailed mathematical models for electroosmotic flow (EOF) and induced charge electroosmosis (ICEO) as this dissertation is based on coupled EOF-ICEO flows. A brief qualitative description is also presented for other commonly used electrokinetic phenomena such as electrophoresis, dielectrophoresis and ACEO. The last section deals with the numerical modeling of electrokinetic phenomena and outlines some of the related numerical issues.

2.2 Electric Double Layer (EDL)

Most of the surfaces acquire electric charge in presence of aqueous solutions such as electrolyte. Some of the involved mechanisms are ionization of covalently bound surface groups or specific ion adsorption e.g. common glass, SiOH, when comes in contact with water acquires negative charge (SiO^-) due to ionization and releases a proton (Lyklema 1995; Hunter 1981). Once the surface is charged, ions in the solution redistribute to attain an equilibrium configuration by balancing diffusive and electrical forces. At equilibrium, charged ion layer in the solution along with the solid surface is known as electric double layer (EDL) as shown in Figure 2.1. The ionic charged layer in fluid bears a charge locally equal in amplitude and opposite in sign to the bound charge on the surface. The fluid side charged layer consists of two parts; (a) the stern layer and (b) the diffuse layer as shown in Figure 2.1. The ions in the stern layer are immobile while ions in the diffuse layer are free to move. With the exception of these charged layers, the fluid is electrically neutral and referred as bulk. The interface between stern and diffuse layer is known as shear plane and potential drop between this plane and bulk solution is known as zeta potential ζ. With the assumption of low potential drop within the stern layer, surface potential (ψ_s) is approximated as zeta potential where later can be measured experimentally.

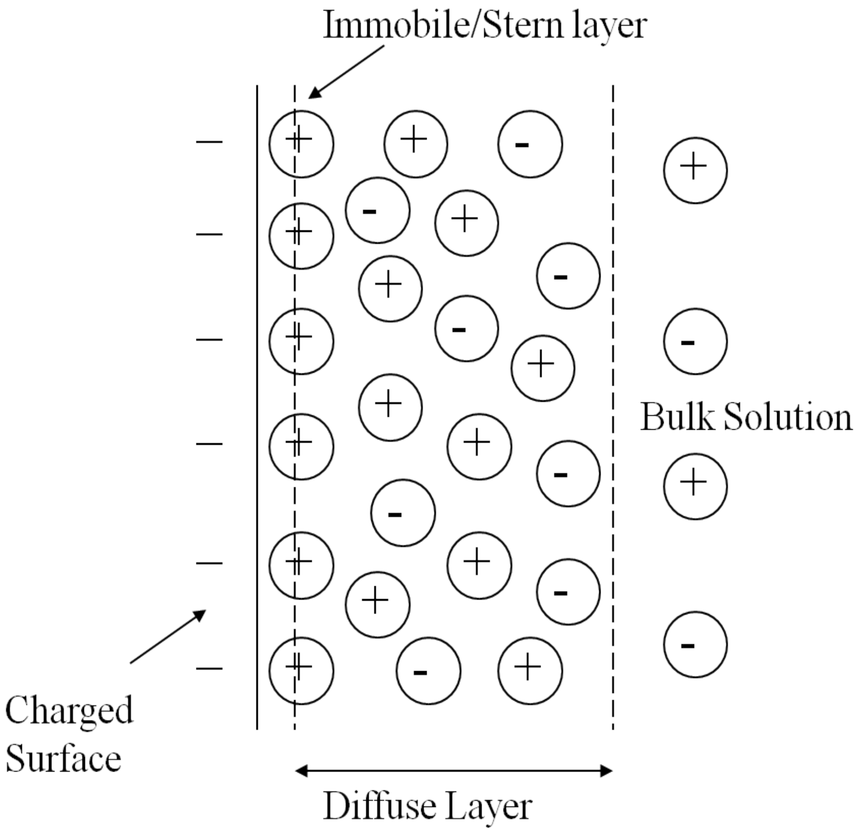

Figure 2.1: Schematic showing electric double layer (EDL).

The electrolyte solutions can be treated as leaky or lossy dielectrics with finite conductivity σ and finite permittivity ε. The Poisson equation describes the electrical potential in a dielectric medium as shown below:

$$\nabla^2\psi = -\frac{\rho_f}{\varepsilon_0\varepsilon_r} \tag{2.1}$$

In the above equation, ψ is the electrical potential, ρ_f is the free charge density, ε_0 is the permittivity of free space and ε_r is the dielectric constant for the medium. The above form of Poisson equation assumes a spatially invariant dielectric constant. In cases where there is no free charge in the solution, the Poisson equation reduced to the Laplace equation:

$$\nabla^2\psi = 0 \tag{2.2}$$

The equilibrium ion concentration is related to electrical potential by Boltzmann distribution:

$$n_i = n_{i\infty}\exp\left(-\frac{z_i e\psi}{k_B T}\right) \tag{2.3}$$

Here n_i and $n_{i\infty}$ are the ionic number concentration and bulk ionic number concentration for i^{th} ionic species, k_B is the Boltzmann constant, T is the absolute temperature, z is the valence of the electrolyte ions and e is the elementary electronic charge. The free charge density ρ_f can be written in terms of ion number concentration as follows:

$$\rho_f = \sum_{i=1}^{N} z_i e n_i \tag{2.4}$$

With the assumption of symmetric electrolyte ($z_+ = z_- = z$), combination of equation 2.1, 2.3 and 2.4 will yield the Poisson-Boltzmann (PB) equation:

$$\nabla^2 \psi = -\frac{2zen_\infty}{\varepsilon_0 \varepsilon_r} \sinh\left(\frac{z_i e \psi}{k_B T}\right) \tag{2.5}$$

When the surface potential ψ_s is small compared to thermal potential ($\psi_s << 0.025$ V), the following approximation, known as Debye-Hückel approximation, can be used:

$$\sinh\left(\frac{z_i e \psi}{k_B T}\right) \approx \left(\frac{z_i e \psi}{k_B T}\right) \quad \left[\because \ \frac{z_i e \psi}{k_B T} << 1\right] \tag{2.6}$$

Using equation 2.6, the linearized version of PB equation can be written as:

$$\nabla^2 \psi = \frac{2e^2 z^2 n_\infty}{\varepsilon_0 \varepsilon_r k_B T} \psi = \kappa^2 \psi \tag{2.7}$$

Here κ is the inverse of Debye length. The Debye length (κ^{-1} or λ) is the distance from the solid surface where the electric potential decays to 33.3 % of its surface potential. The linearized PB equation can be solved analytically for one-dimensional case of uniformly charged flat plate. The solution demonstrates exponential decay for electric potential as follows:

$$\psi = \psi_s \exp(-\kappa x) \tag{2.8}$$

For the one-dimensional case, full non-linear PB equation can be solved analytically and the solution is known as the Gouy-Chapman theory:

$$\psi = \frac{4k_B T}{ze} \tanh^{-1}\left[\tanh\left(\frac{ze\psi}{4k_B T}\right)\exp(-\kappa x)\right] \tag{2.9}$$

As evident, the equation 2.9 can be reduced to equation 2.8 using the Debye-Hückel approximation. Once the potential distribution is known the corresponding ion distribution can be estimated using Boltzmann distribution (equation 2.3). The analytical solutions are also reported for simple geometries such as sphere and cylinder using Debye-Hückel approximation. In the thin EDL limit, any arbitrary geometry could be related to flat plate case (assuming that EDL is much smaller than the curvature of surface) and equations 2.8 and 2.9 could be used. For arbitrary EDL thickness and complex shapes, it is impossible to obtain analytical solution for linear or non-linear PB and numerical modeling should be employed.

The presented equations utilize the following major assumptions: (a) the ions are considered as point charges and there is no upper limit on ion concentration. For example, in case of very high surface potential, owing to the exponential dependence, the ionic concentration could reach unrealistic values. (b) Secondly, the dielectric constant is assumed to be spatially invariant even in the vicinity of solid surface. Also, it should be noted that Poisson-Boltzmann equation and the presented solutions are derived for equilibrium condition. In presence of external gradients such as externally applied field or concentration gradients would result in deviation from above solutions. In case of weak external gradients the deviations from the equilibrium could be neglected (assuming quasi-equilibrium) and PB equation can still be used to model the system (Li 2004).

The ion concentration distribution, in presence of external gradients, can be modeled accurately using ion conservation equation:

$$\frac{\partial n_i}{\partial t} + \nabla . J_i = R_i \tag{2.10}$$

In the above equation, J_i is the number concentration flux and R_i is the production rate due to chemical reactions for i^{th} species. The ionic flux (based on number concentration) is given by the Nernst-Planck (NP) equation as shown below:

$$J_{ni} = n_i u - D_i \nabla n_i - \frac{z_i e D_i n_i}{k_B T} \nabla \psi \tag{2.11}$$

The above equation shows convective (first term on RHS), diffusive (second term on RHS) and electrical (third term on RHS) contributions to the total flux. In equilibrium conditions (convective contribution is nil), the Nernst-Planck equation can be analytically integrated to yield equilibrium Boltzmann ion distribution (equation 2.3). The NP equation can also be written in terms of molar flux (Masliyah and Bhattacharjee 2006) as shown below:

$$J_{ci} = c_i u - D_i \nabla c_i - \frac{z_i F D_i c_i}{RT} \nabla \psi \qquad (2.12)$$

In the above equation, c_i and D_i represent molar concentration and diffusivity of i^{th} species. Here F is the Faradays constant and R is the universal gas constant. In this study, ionic flux based on molar flux is utilized and denoted by J_i ($J_{ci} = J_i$).

2.3 Electro-osmosis and Electrophoresis

Electro-Osmosis (EO) is the flow of charged liquid, under the influence of electrical body force acting on the diffuse layer of Electric Double Layer (EDL). An external electric field causes free ions in the diffuse layer to migrate, which in turn drives the adjacent fluid layer and subsequently the bulk fluid due to fluid viscosity as shown in Figure 2.2. The velocity at the edge of the boundary layer (slip-velocity u_s) is proportional to the local electric field and the zeta potential ζ (potential difference between the bulk fluid and the wall). The velocity in the bulk is uniform (Figure 2.2) yielding a plug-flow type velocity profile with the exception of EDL.

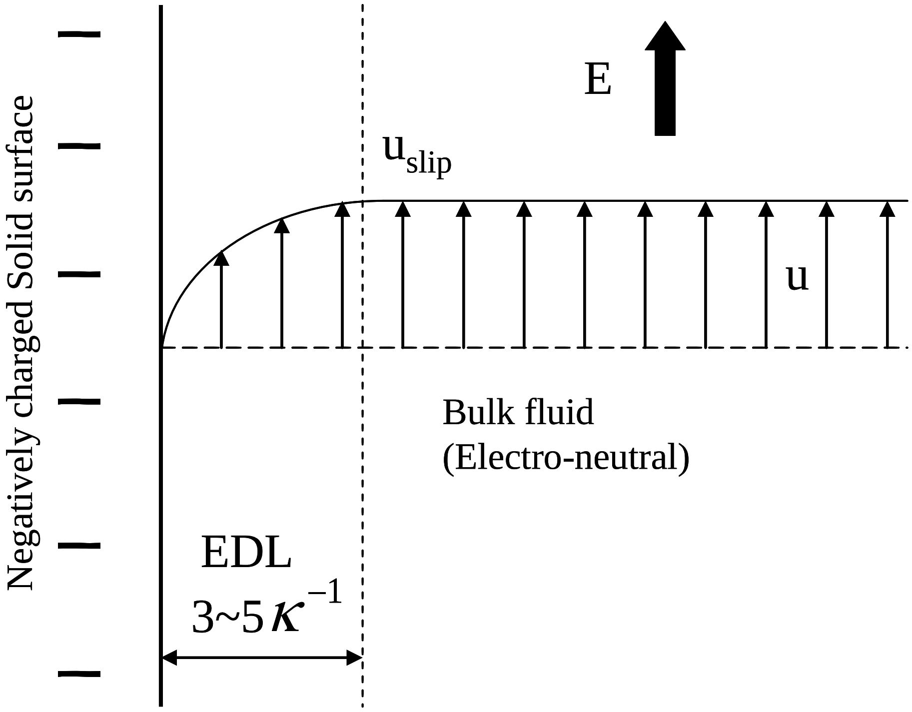

Figure 2.2: Schematic showing EOF on negatively charged surface. The velocity profile is similar to plug-flow with exception of flow in EDL.

The electro-kinetic fluid flow can be modeled by adding an electrical body force term in the momentum balance (Navier-Stokes (NS)) equation. The electrical body force term is given by (Saville 1997):

$$f_E = \rho_f E - \frac{1}{2} E.E \nabla \varepsilon + \frac{1}{2} \nabla \left[\left(\rho \frac{\partial \varepsilon}{\partial \rho} \right)_T E.E \right] \tag{2.13}$$

With the assumption of constant permittivity and incompressibility, the second and third term on the RHS can be neglected and the above equation reduces:

$$f_E = \rho_f E = -\rho_f \nabla \psi \tag{2.14}$$

Using the above equation, the Navier-Stokes (with the electrical body force term) can be written as:

$$\rho \frac{\partial u}{\partial t} + \rho (u.\nabla u) = -\nabla p + \mu \nabla^2 u + \rho g - \rho_f \nabla \psi \tag{2.15}$$

For steady state creeping flow, the transient term and the inertial term can be neglected. Further neglecting the gravitational force and assuming constant density, the NS equation along with continuity equation can be written as:

$$\begin{aligned} \nabla p &= \mu \nabla^2 u - \rho_f \nabla \psi \\ \nabla .u &= 0 \end{aligned} \tag{2.16}$$

The steady electro-osmotic flow (EOF) can be modeled using mathematical models of varying complexity. We will discuss the following models along with their advantages and limitations; (a) full PNP-NS model, (b) PB-NS model and (c) slip-velocity model for thin EDL limit.

The full PNP-NS model would utilize equations 2.1, 2.10-2.12 and 2.16 for resolving EDL (potential and electrolyte ion concentration) and fluid flow. In principle, it can be utilized for any arbitrary EDL thickness, any applied external field to capture any deviation from equilibrium EDL. On the downside, it is computationally expensive owing to the coupled non-linear nature of the model. The level of complexity increases with the decreasing Debye thickness and a very fine mesh is required to capture the gradients in the EDL.

The model complexity can be reduced by assuming equilibrium ion distribution in the EDL. Under weak applied fields such assumption is valid and PB equation (2.5) can be employed replacing PNP equations for potential and electrolyte ion distribution. Hence the PB-NS model consist of equation 2.5 and 2.16. It can be used for arbitrary EDL thickness and weak applied fields. In particular, it is often employed for analytical treatment of EOF problems in simple geometries. The EOF model can be further simplified in the thin EDL limit using Helmholtz-Smoluchowski slip velocity model. In this approach, the effect of EDL is accounted by incorporating slip-velocity boundary condition at fluid-solid interface. For thin EDL limit, the Helmholtz-Smoluchowski velocity is given by:

$$u_{slip} = \frac{\varepsilon_0 \varepsilon_r \zeta}{\mu} E \tag{2.17}$$

With the assumption of thin EDL, the excess free charge in the EDL can be neglected and the electrical potential distribution is give by the Laplace equation (equation 2.2). Hence equations 2.2, 2.16 and 2.17 can be employed for modeling steady EOF in the thin EDL limit (Burgreen and Nakache 1964; Rice and Whitehead 1965). Due to reduced complexity, this model has been widely used for modeling steady EOF in variety of microfluidic devices. As the surface charge/ zeta potential is assumed as a constant property, the classical EOF flow is also termed as fixed charge electro-osmosis (FCEO).

Another important consideration from modeling perspective is to account for Joule heating effects. In case of high electric field strengths or highly conductive buffer solutions, Joule heating effects are significant and results in increase and non-uniformity in the fluid temperature. The localized fluid temperature rise can be approximated using the order of magnitude analysis (Chang and Yeo, 2009) as:

$$\Delta T \sim \frac{\sigma V^2}{k} \tag{2.18}$$

In the above equation, σ and k represent the electrical conductivity and thermal conductivity of the electrolyte. For the simulation parameters used in this study, the average temperature rise ($\Delta T < 1$ K) is negligible. Hence the transport properties can be treated as constant for modeling electrokinetic flow. The experimental study by Tang et al. (2006) also confirms negligible Joule heating effects for typical parameters used in this work (dilute electrolytes (0.1 mM), channel width ~ 100 μm and E ~ 100 V/ cm).

Electrophoresis deals with the motion of charged particle under the effect of external electric field in presence of electrolyte solution. The electric double layer will be formed due to the presence of surface charge. In presence of uniform external electric field *E*, the particle's electrophoretic velocity is given by:

$$u_{ep} = \nu E \tag{2.19}$$

Here ν represents the electrophoretic mobility of the particle. Various forces acting on the particle are electrostatic force due to particle's charge, viscous drag and retarding electrostatic force due to counter-ions in EDL. The mobility can be estimated by balancing electrostatic force and hydrodynamic force where later can be estimated by integrating the hydrodynamic stress and Maxwell stress acting on the particle's surface. Therefore, by solving NS equation for momentum balance, Poisson equation for potential distribution and NP equation for ion distribution, electrophoretic mobility can be estimated. In the thin EDL limit, the electrophoretic velocity of spherical particle is exactly opposite to the EO velocity along a flat surface with same zeta potential (Anderson 1989). Therefore electrophoretic mobility of spherical particle with zeta potential ζ can be written as $\nu = \frac{\varepsilon_0 \varepsilon_r \varsigma}{\mu}$. In the other limit where EDL is much larger than the particle's radius, the mobility is given by $\nu = \frac{2\varepsilon_0 \varepsilon_r \varsigma}{3\mu}$. For arbitrary EDL thickness, mobility can be estimated using Henry's formula (Henry 1931).

2.4 Induced Charge Electro-osmosis (ICEO) & AC Electro-osmosis (ACEO)

Induced charge electro-osmosis (ICEO), is similar to FCEO except that the surface charges are induced on conducting or polarizable surface by an externally applied electric field. Initially, the electric field lines intersect the conducting surface at right angles and induce surface charge on the conducting surface (Figure 2.3a). When electrolyte solution is present, due to the nature of induced charges, an induced EDL is formed near the conducting surface. A fully charged induced EDL screens the induced charges and the electric field lines are expelled from the conducting surface (Figure 2.3b). At steady state, the distribution of induced charges over the conducting surface is non-uniform. The induced zeta potential at steady state is bipolar, with magnitude $\zeta_i \sim E\,a$ representing the potential drop of the external field E over the characteristic length scale of polarizable object (a). The net induced charge is zero and the conductor behaves effectively as an insulator. Similar to FCEO, the diffuse charge in the induced EDL is driven by external electric field and the resulting flow in termed as induce charge electro-osmosis (ICEO). The quadrupolar flow patterns are observed for ICEO flow near perfectly conducting cylindrical post in infinite medium (shown later in Figure 2.6a). In the thin EDL limit, the corresponding Smoluchowski slip velocity at the polarizable surface can be written as:

$$u_{slip-ICEO} = \frac{\varepsilon_0 \varepsilon_r \zeta_i}{\mu} E \sim \frac{\varepsilon_0 \varepsilon_r a}{\mu} E^2 \qquad (2.20)$$

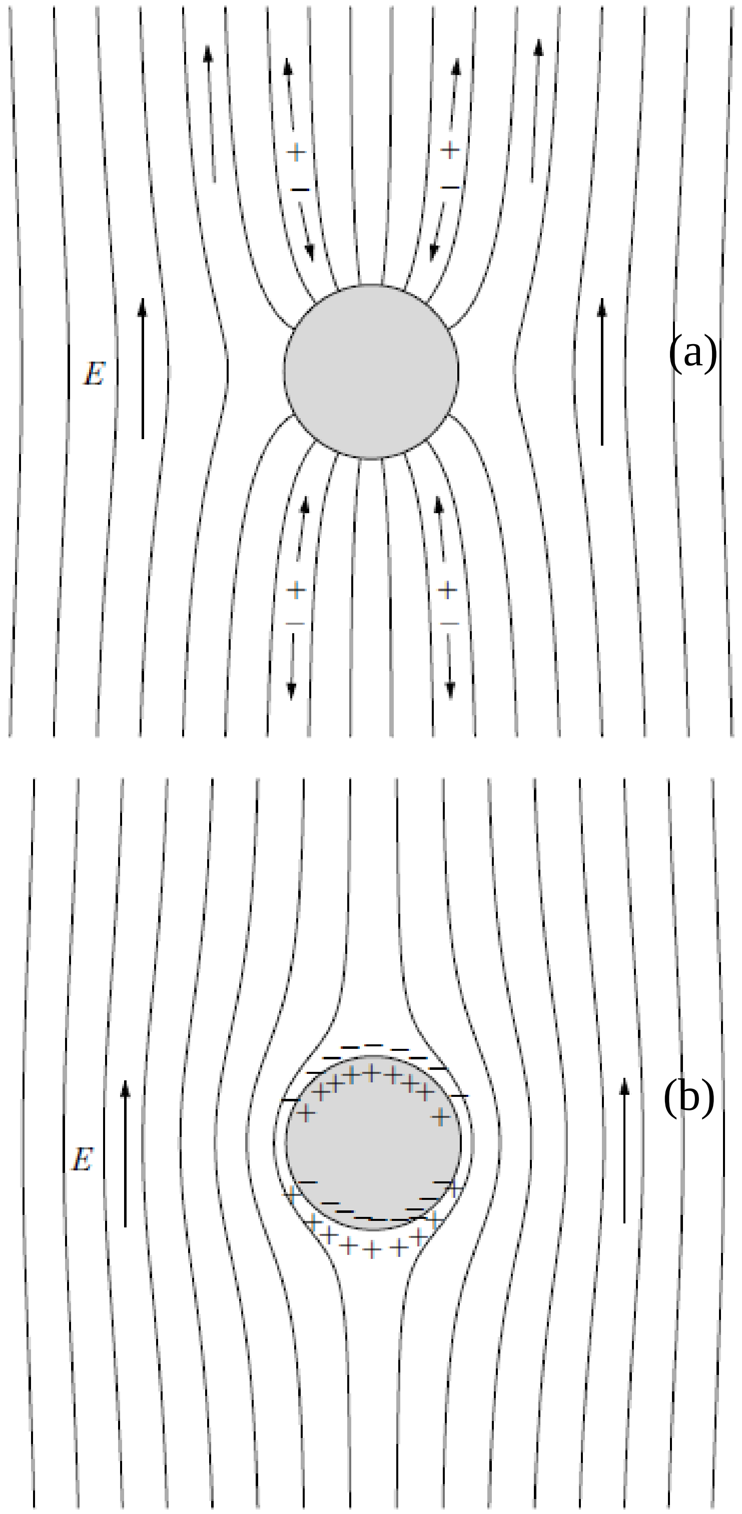

Figure 2.3: ICEO flow around an ideally polarizable cylinder (a) Electric field lines before EDL charging; (b) Electric field line after EDL charging (adapted with permission from Squires and Bazant 2004).

ICEO phenomena were initially investigated by the colloid scientists. Levich (1962) studied the effect of induced charge cloud around a metal colloid sphere on its electrophoretic mobility. He concluded that the electrophoretic mobility of metal colloid particle is similar to an insulating particle as at steady state induced charge cloud screens the induced charge. The non-linear flow fields around such polarizable colloids were investigated theoretically and experimentally by Dukhin Gamayunov, Murtsovkin, and coworkers (Gamayunov et al. 1986; Dukhin and Murtsovkin 1986; Murtsovkin and Mantrov 1991; Gamayunov et al. 1992; Murtsovkin 1996).

Recently, this phenomenon was studied with reference to the micro-fluidic by applying AC field directly on the micro-electrodes and the flow is termed as AC electro-osmosis (ACEO) as shown in Figure 2.4 (Ramos et al. 1999; Green et al. 2000a; Gonzalez et al. 2000b; Green et al. 2002b). Thus ACEO studies the fluid flow on electrodes which are also being used for generating AC electric field. On the other hand, ICEO deals with the fluid slip over polarizable surface where surface charges are induced by external field. The strength of ACEO flow is dependent upon the frequency of applied field. It can be observed as long as the frequency is low enough that induced charge clouds have time to form, but fast enough that electrodes (and the fields they establish) are not screened. The schematic shown in Figure 2.4 generates symmetric flow with net flow rate being zero (Ramos et al. 1999; Green et al. 2000b; Gonzalez et al. 2000a; Nadal et al. 2002; Green et al. 2002a).

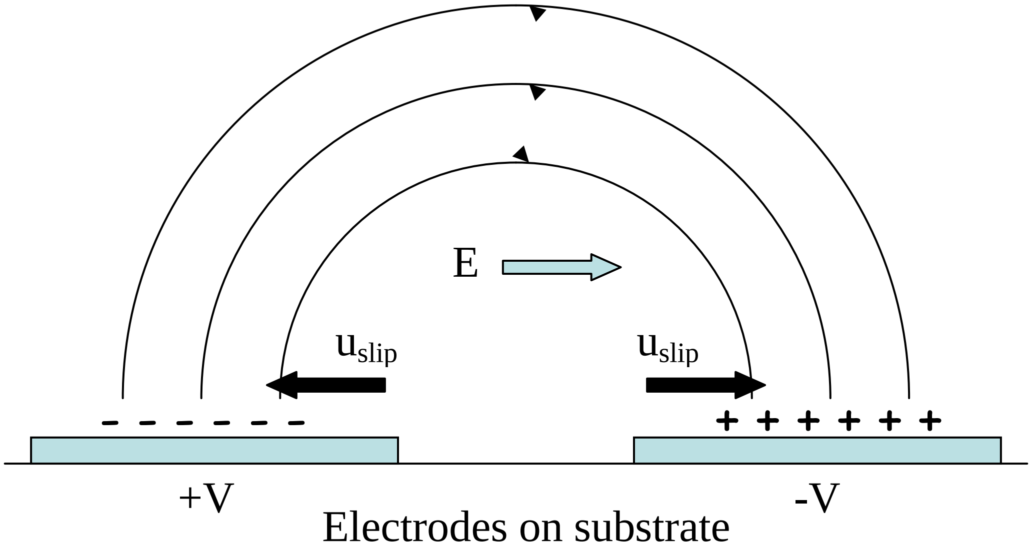

Figure 2.4: Schematic showing ACEO flow over microelectrode surface.

For ACEO pumping applications, it is essential to break the symmetry of electric field around a pair of electrodes to produce a unidirectional flow (Ajdari 2000; Ramos et al. 2003). The symmetry can be broken by using geometrically asymmetric electrodes with unequal width (Brown et al. 2001; Mpholo et al. 2003; Studer et al. 2002; Studer et al. 2004) or by inducing polarization asymmetry using biased AC field (Wu 2006). Apart from coplanar electrode structure as shown in Figure 2.4, Bazant and Ben (2006) proposed three dimensional (3D) electrode designs for ACEO pumping. In their study, numerical simulations predicted that their 3D design pumps can enhance the electro-osmotic pumping significantly (even by one order of magnitude i.e. achieving velocities of mm/sec scale with only a few volts). The theoretical proposition for 3D ACEO pumping was further investigated experimentally (Urbanski et al. 2006; Urbanski et al. 2007).

The term ‘induced charge electro-osmosis’ (ICEO) was first coined by Bazant and Squires (2004) and Squires and Bazant (2004) where they describe the physical mechanism of induced charge flows near a polarizable surface. They also acknowledged that the ICEO flows were studied earlier by Murtsovkin (1996) and Gamayunov et al. (1992) with reference to metallic colloids. Bazant, Squires and coworkers studied ICEO around a polarizable metal cylinder in AC and DC electric fields both theoretically (Bazant and Squires 2004; Squires and Bazant 2004) as well as experimentally (Levitan et al. 2005). In their theoretical study, Bazant and Squires (2004) identified ICEO as promising strategy for efficient pumping and mixing in microfluidic devices. Various studies have reported microfluidic devices based on ICEO for mixing (Zhao and Bau 2007a; Harnett et al. 2008; Wu and Li 2008a; Jain et al. 2009a; Wu and Li 2008b), flow regulation (Wu and Li 2008a), concentration gradient generation (Jain et al. 2010). The effect of hydrodynamic and electrostatic forces on polarizable cylindrical particles adjacent to wall was examined by Zhao and Bau (2007b). A recent review by Daghighi and Li (2010) outlines the basics of ICEO along with its recent applications. Although most of the reported studies are based on perfectly conducting (ideally polarizable) surface, ICEO flows can occur on any polarizable surface as observed by Thamida and Chang (2002), Yossifon et al. (2006). Induced charge electrophoresis (ICEP) deals with the movement of a conducting or polarisable particle due to the interaction of an applied electric field with the induced charge and induced EDL of the particle. In presence of external field, the non-uniform nature of the induced EDL results in non-uniform ICEO flow and vortices around the particle. In case of asymmetric particle shape, the complexity increases due to non-uniform induced-charge distribution and induced EDL around the particle, consequently affecting the characteristics of the ICEP. Recent ICEP research include study of particle-wall interaction (Zhao and Bau 2007b; Yariv 2009; Wu et al. 2009), particle-particle interaction (Wu and Li 2009; Saintillan 2008), and non-spherical particles (Yariv 2005; Yossifon et al. 2007; Squires 2009; Saintillan et al. 2006). A more detailed explanation and related references can be found elsewhere (Daghighi and Li 2010).

ICEO offers various advantages over FCEO flows for LOC devices. ICEO flow velocity varies quadratically with electric field (equation 2.19), ICEO flows persist in AC fields (Bazant and Squires 2004; Squires and Bazant 2004). Further strong flows can be obtained with low applied electric fields as ICEO velocity scales quadratically with electric field. Secondly, zeta potential on the polarizable surface can be controlled/ tuned with the magnitude of applied electric field (Squires 2009), which in turn could be used to generate variety of flow patterns within the micro-device.

The ICEO flow can also be analyzed using the mathematical models presented in previous section i.e. (a) full PNP-NS model, (b) PB-NS model and (c) slip-velocity model for thin EDL limit. The only difference would be the estimation of induced zeta potential or induced surface charge density at the solid-liquid interface. For steady ICEO flow, the standard electrostatic boundary condition which relates the jump in electrical displacement (*D*) to the surface charge density (q_s) can be used (Zhao and Bau 2007b) as shown below:

$$\left(D_2 - D_1\right).n = q_s \tag{2.21}$$

For slip-velocity model, induced zeta potential can be numerically estimated using the correction method proposed by Wu and Li (2008a) which is briefly described hereafter. At steady state, induced field on the conducting surface should be equal in magnitude and opposite in direction to the externally applied field, i.e.

$$E_i = -E \qquad \Rightarrow \qquad \nabla \varsigma_i = -\nabla \psi \tag{2.22}$$

Upon integration the above equation yields the following relation:

$$\varsigma_i = -\psi + \psi_c \tag{2.23}$$

Here ψ_c is the constant correction potential, which can be estimated using charge conservation on the conducting surface. Also the surface charge density q_s is linearly related to the small values of zeta potential as $q_s = \varsigma\, \varepsilon_0 \varepsilon_m \kappa$, where κ is the inverse of Debye length. Using the above relation, charge conservation equation for the conducting surface can be written as follows:

$$\int_s \varsigma_i dA = 0 \tag{2.24}$$

Using equations 2.23 and 2.24, we can obtain the following relation for correction potential ψ_c:

$$\psi_c = \frac{\int_s \psi \, dA}{A} \tag{2.25}$$

In the above equation, A represents the surface area of the conducting obstacle. The correction potential method is used for ICEO flow modeling in chapter 4.

2.5 Dielectrophoresis

Dielectrophoresis is the motion of polarizable particles that are suspended in an electrolyte and subjected to a spatially non-uniform electric field (Pohl 1978, Jones 1995). The electric field polarizes the particle and the suspending fluid and induced dipole moments. Due to non-uniform electric field, the poles of dipoles experience different field strengths resulting in net force which drives the particle motion. When the induced dipole moment on the particles is large than that of the fluid, the particles move toward the regions of high electric field density. This is known as positive dielectrophoresis. In the case of the fluids being more polarizable than the particles, the particles move away from the high electric field density, which is known as the negative dielectrophoresis.

The time average dielectrophoretic force on a sphere of radius '*a*' is proportional to ∇E_{rms}^2 (Pohl 1978, Jones 1995) and given by the following equation:

$$F_{DEP} = 2\pi a^3 \varepsilon_m \operatorname{Re}\left[f_{CM}\right] \nabla E_{rms}^2 \tag{2.26}$$

In the above equation, ε_m is the dielectric permittivity of the medium and $\operatorname{Re}\left[f_{CM}\right]$ indicates the real part of the Clausius-Mossotti factor. The Clausius-

Mossotti factor is a measure of the effective polarizability of the particle and is given by

$$f_{CM} = \frac{\varepsilon_p^* - \varepsilon_m^*}{\varepsilon_p^* + 2\varepsilon_m^*} \tag{2.27}$$

Here ε_p^* and ε_m^* represent the complex permittivities of the particle and the medium respectively. The complex permittivity of a material can be expressed as:

$$\varepsilon^* = \varepsilon - i\frac{\sigma}{\omega} \tag{2.28}$$

In the above equation ε is the permittivity, and σ is the conductivity of the material. The positive and negative dielectrophoresis (i.e. motion of particles towards or away from the large electric field gradients) are obtained when $\mathrm{Re}\left[f_{CM}\right] > 0$ and $\mathrm{Re}\left[f_{CM}\right] < 0$, respectively. These properties of dielectrophoresis enable highly controlled selective micro fluidic particle/cell separation methodologies. It is routinely used for biological LOC devices for cell sorting and separation (Pethig and Markx 1997; Morgan and Green 1997; Green et al. 1997; Green and Morgan 1997). A recent review outlines the theory and recent advances in applications of dielectrophoresis (Pethig 2010).

2.6 Numerical Model Validation using Standard Results

The analytical solutions for electrokinetic problems are limited to simple geometries and low surface potentials. For complex geometries, numerical simulations are employed to solve the governing equations discussed earlier in this chapter. To the best of our knowledge, there are no analytical solutions available to examine combined FCEO-ICEO flow in a single geometry. Therefore, we have utilized commercially available finite element solver ‘Comsol’ (earlier known as FemLab) for solving mixed FCEO-ICEO flow problems in complex geometries. There are many commercial PDE (partial differential equation) solvers are available commercially. However, Comsol is chosen due to its multi-physics simulation capability (ideal for electro-kinetic flow) and user-friendly interface. Using Comsol, various electrokinetic model problems were solved such as: electro-osmotic flow and mixing in a T-channel, electrophoresis of spherical particle, band dispersion in serpentine microchannels (including geometric optimization of design), ICEO around ideally polarizable cylinder etc. The obtained results were in agreement with the standard analytical solutions and some of the standard results, which would be useful for next chapters, are presented below.

The numerical results for FCEO velocity profile are compared to the analytical solution (Patankar and Hu 1998) for $\kappa W = 25$ & $\kappa W = 100$ in Figure 2.5a. The velocity profile is flat across the channel width, except the electric double layer region. Due to the plug-flow type, it is difficult to mix species in such conditions.

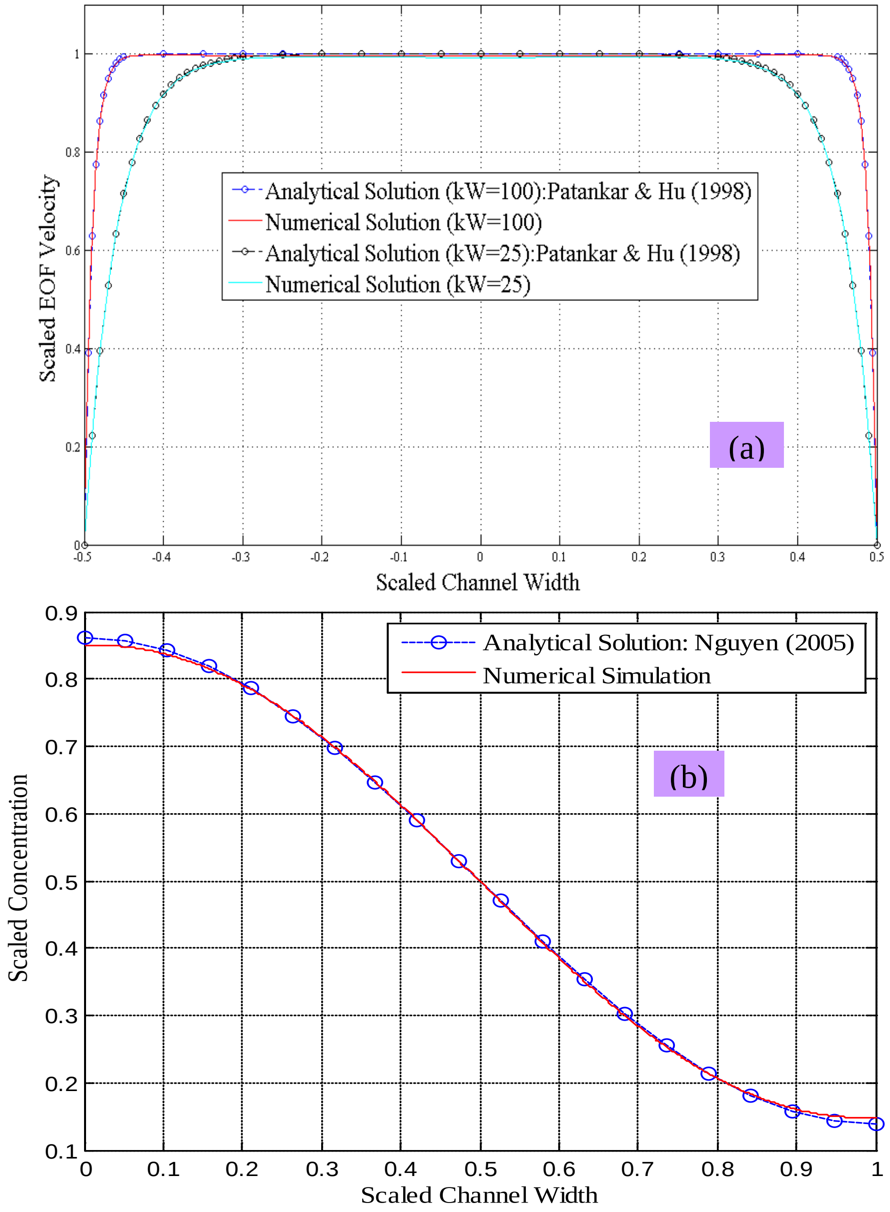

Figure 2.5: (a) Comparison of numerical & analytical solution for EO velocity profile for FCEO traditional mixer and (b) comparison of numerical & analytical solution of species concentration at exit for FCEO traditional mixer.

The most basic micro-mixer is a T-mixer where two confluent streams (with scaled concentration of 1 and 0 respectively) mix due to transverse diffusion. In Figure 2.5b, the numerical solution is presented for the exit species concentration and compared with the analytical solution for the T-mixer (Nguyen and Wu 2005). Next we present results for steady ICEO flow in the vicinity of ideally polarizable conducting cylinder in infinite medium (Bazant and Squires 2004; Squires and Bazant 2004). As discussed earlier in section 2.4, electric field act on the induced EDL to generate quadrupolar flow as shown through velocity surface plot and velocity streamlines in Figure 2.6a. The analytical solution for the velocity field, in the thin EDL limit, suggests that the scaled maximum slip velocity (u_s/U_{ref} at $\theta = 45^o$) should reach a value of 2 for very thin EDL (Squires and Bazant 2004) as suggested by the following equations:

$$\begin{aligned} u_s &= 2\frac{\varepsilon_0\varepsilon_r E^2 a}{\mu}\sin 2\theta \\ U_{ref} &= \frac{\varepsilon_0\varepsilon_r E^2 a}{\mu} \end{aligned} \tag{2.29}$$

The scaled slip velocity w.r.t EDL thickness is plotted in Figure 2.6b, while maximum velocity location is marked in Figure 2.6a. In Figure 2.7, surface plot for excess charge α ($\alpha = \bar{c}_1 - \bar{c}_2$ i.e. the difference between positively and negatively charged electrolyte ion concentrations) is shown for κa ~ 25. The variable α takes on positive and negative values at the left and right half of the semi-cylinder, respectively (due to induced charges).

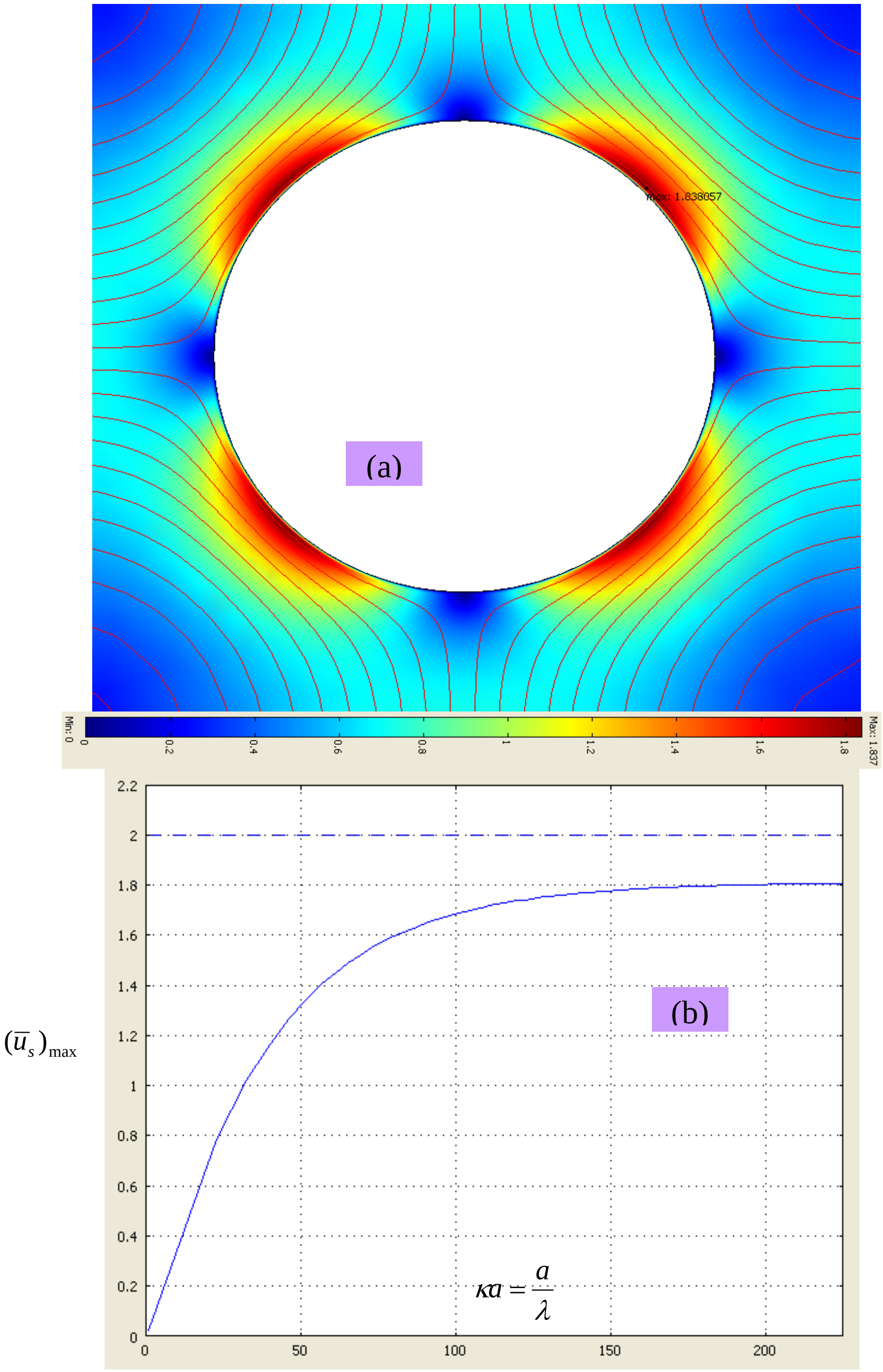

Figure 2.6: (a) Velocity surface plot and streamlines around conducting cylinder in infinite medium for $\kappa a \sim 225$. The maximum slip velocity is observed at $\theta = 45^o$) and (b) maximum slip velocity dependence on *ka* for ICEO flow around a cylinder in infinite medium.

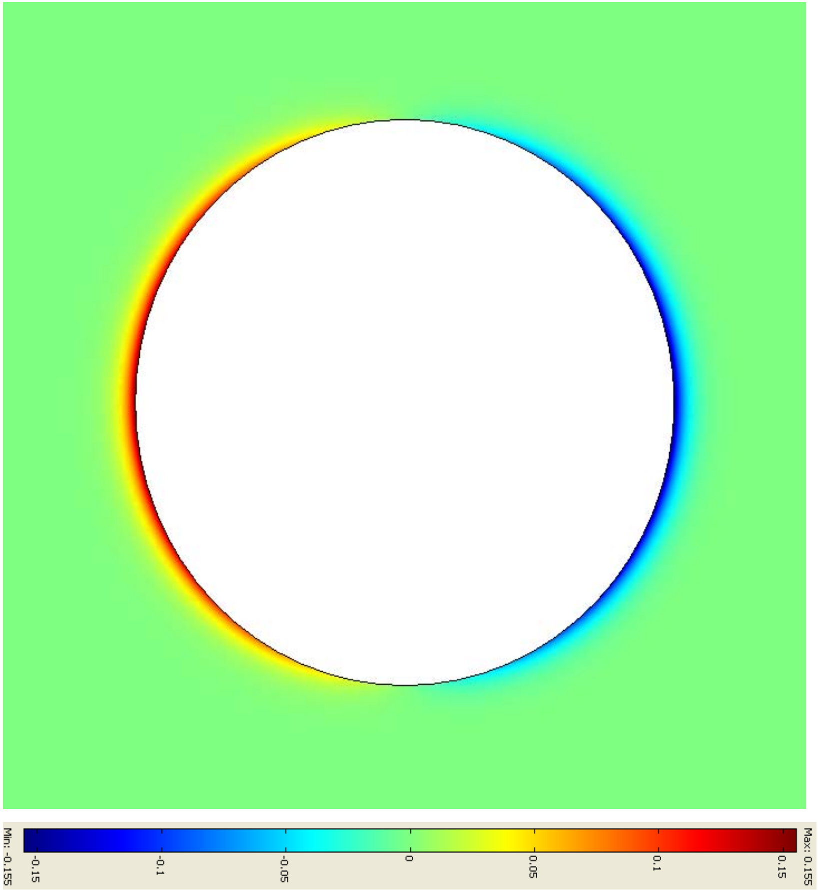

Figure 2.7: Surface plot for α around the conducting cylinder of radius a in infinite medium for $\kappa a \sim 25$.

The presented numerical results are in agreement with the standard analytical solutions presented for FCEO & ICEO, which demonstrates that the modeling procedures adopted in this work are valid and provide reliable results. Therefore, we apply a similar modeling approach for modeling FCEO-ICEO in forthcoming chapters. In general, fine meshes are utilized near interfaces (more details are provided in next chapters). The numerical analysis was repeated with various mesh sizes to ensure the mesh-independency of the obtained results.

2.7 Summary

The basic concepts related to classical electro-kinetics and non-linear induced charge electro-kinetics (ICEK) were presented. First, the electric double layer and related models were discussed. Thereafter, detailed mathematical equations and different models were outlined for electro-osmotic flow followed by qualitative description for electrophoresis, AC electro-osmosis (ACEO) and dielectrophoresis (DEP). Lastly, some numerical results were validated against the standard analytical solutions for FCEO & ICEO flow. The provided theoretical framework would be helpful in understanding the studies presented in following chapters.

Chapter 3

Efficient Micromixing using Induced Charge Electro-Osmosis[#]

3.1 Introduction

Micro-mixers are often a vital component in LOC devices as mixing efficiency may directly affect the performance of the LOC device. The micro-mixing applications can be categorized as (a) biological applications for micro-total analysis systems; and (b) chemical applications (Hardt et al. 2005; Chew et al. 2007; Jeong et al. 2010). The micromixing technologies have been successfully applied to a variety of biological applications such as enzyme assays (Atalay et al. 2009; Schilling et al. 2002; Hadd et al. 1997), DNA analysis (Liu et al. 2008; Liu et al. 2004; Lee et al. 2005), protein folding (Bilsel et al. 2005), biochemical detection (Yea et al. 2005; Dittrich and Manz 2006; Chang 2006) etc. Besides biological analysis, another vital application field of micromixing technology is in

---

[#] A version of this chapter has been published. [M. Jain, A. Yeung and K. Nandakumar, JMEMS, 18(2), 376-384 (2009)] micro-reactor. The microscopic length scale associated with LOC devices favors heat transfer and allows the better control of chemical reactions. Various studies have reported micro-reactor (with micro-mixer) based chemical synthesis applications with better yield and selectivity as compared to traditional reactor systems (Nagaki et al. 2005; Hessel et al. 2004).

Under most operating conditions, the flow in a micro-device is viscosity dominant within the laminar regime. In particular, when the fluid transport is due to FCEO, the velocity profile is effectively plug flow (except for a thin "boundary layer" adjacent to the wall). Such low Reynolds number flow patterns are, by nature, very difficult to mix and the predominant mechanism of equalizing concentration differences is often diffusion — a relatively slow form of mass transfer. Various techniques have been proposed to enhance micromixing based on chaotic advection (Stroock et al. 2002; Lee et al. 2001; Xia et al. 2005; Chew et al. 2005), AC or DC electrokinetics (Deval et al. 2002; Feng et al. 2007; Wu and Li 2008a; Chang and Yang 2007; Huang et al. 2006; Wang et al. 2006; Kutter et al. 1997), magnetohydrodynamics (Bau et al. 2001; Wen et al. 2009), acoustics (Frommelt et al. 2008; Yang et al. 2001; Liu et al. 2002), pressure and temperature effects (Glasgow and Aubry 2003; Glasgow et al. 2004; Okkels and Tabeling 2004; Niu and Lee 2003) etc. The mixers used in microdevices can be categorized into active and passive mixers (Nguyen and Wu 2005). Active mixers utilize external energy—via pressure, electrokinetic disturbance etc.—to induce secondary transverse flows. On the other hand, diffusion and chaotic advection are the dominant mixing mechanisms in passive mixers achieved by modification in geometry/ surface of the micro-channel. An excellent review of various micro-mixer types and their comparison is provided by Nguyen and Wu (2005). Other reviews which focus on electrokinetic mixing techniques and passive mixers are due to Chang and Yang (2007) & Hardt et al. (2005) respectively. We will review some of the active as well as passive micromixers designs within the framework of parallel flow electrokinetic micromixers.

In this chapter, we exploit ICEO for mixing improvement in the T-mixer design by introducing a semi-cylindrical conducting obstacle embedded in the channel wall. The design concept is based on the observed quadrupolar flows around ideally polarization cylinder in infinite medium (Bazant and Squires 2004). A similar methodology for enhancing mixing is proposed by Wu et al. (Wu and Li 2008a) via use of conducting triangle hurdles and was later verified experimentally (Wu and Li 2008b). They proposed numerical correction method for the estimation of induced zeta potential and thereafter utilized slip-velocity approach to model steady state ICEO flows. Other studies utilizing ICEO for micromixing includes microfluidic chaotic stirrer (Zhao and Bau 2007a) and usage of conductive metallic coating on channel walls (Harnett et al. 2008). The following section reviews the most notable parallel flow type electrokinetic micro-mixers reported in the literature. Next, we present the mathematical model along with the qualitative analysis of the proposed geometric design. Finally, the effect of design parameters on mixing performance is analyzed in the Results section.

3.2 Parallel Flow Electrokinetic Micro-mixers

The most basic micro-mixer is a T-mixer or Y-mixer, where two confluent streams mix due to transverse diffusion (Ismagilov et al. 2000; Kamholz et al. 1999). Various studies have examined T-mixer theoretically and experimentally. Due to diffusion limitation, T-mixer requires longer time ($t_m \sim w^2/D$) and long channel lengths ($L_m \sim Pe_* w$) to realize complete mixing. To enhance micro-mixing, several modifications of T-mixers are reported such as sequential injection of samples in T-mixer, heterogeneously charged walls, grooves on the channel base, geometric variations by introducing physical constrictions etc. Typically, such designs provide effective mixing either by reducing the diffusion length or by increasing the interfacial contact area for mass transfer within the microchannel.

Passive mixing in electrokinetically driven flow can be achieved by utilizing lamination, focusing or chaotic mixing. Hence, parallel lamination mixing generally refers to the inlet mixing stream being split into two or more sub-streams. In the case of lamination, the inlet stream typically being split into *n* sub-streams, and then recombined horizontally in a single stream so as to reduce the diffusion length (Hadd et al. 1997; Jacobson et al. 1999). Another variation involving reduction of diffusion length in multiple stream inlets is flow focussing or hydrodynamic focusing. In flow focussing, the sheath flows from the side inlets are used to focus the sample stream (usually the central inlet) to reduce the effective sample width (Jacobson and Ramsey 1997; Yang et al. 2005; Lin et al. 2002; Wu and Yang 2006). However uniform mixing cannot be achieved through out the cross-section using focussing methods (Frommelt et al. 2008). Mixing performance can also be improved marginally by introducing non-conducting obstacles embedded on the micro-channel wall. The mixing performance can be significant increased with the use of heterogeneously charged obstacles (Chen and Cho 2007; Chang and Yang 2004).

In chaotic mixing, the interfacial contact area is greatly increased and the diffusion length is reduced by means of the repeated stretching and folding of the fluids in a microchannel. Typically it is achieved by the stimulation of secondary/ transverse flows in the channel. Johnson and coworkers (Johnson et al. 2002; Johnson and Locascio 2002) used slanted grooves to generate helical flows within the microchannel to augment mixing performance. The same group (Johnson and Locascio 2002) also investigated the numerical effect of the design parameters such as groove angle relative to the channel axis, the groove depth, and the zeta potential (i.e. surface charge density) ratio of groove to main channel on electro-osmotic flow mixing over periodic slanted grooves. Typical design of staggered herringbone mixer (SHM) is shown in Figure 3.1, where Stroock et al. 2002 utilized similar design to achieve chaotic mixing with pressure driven flows.

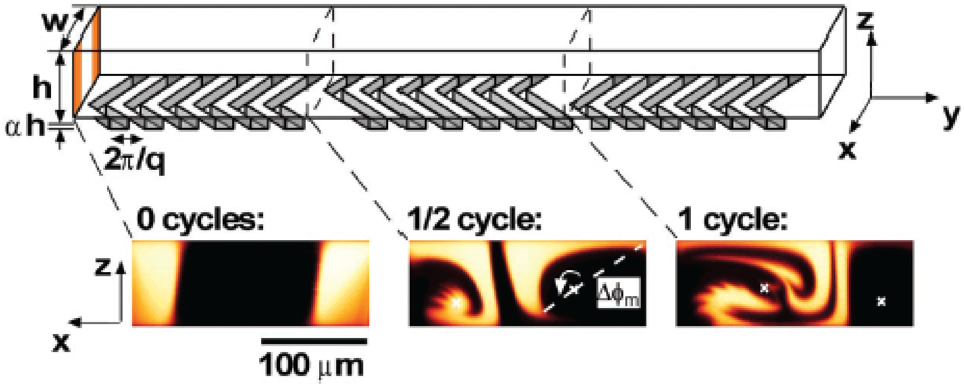

Figure 3.1: Staggered Herringbone Mixer (SHM) design and the corresponding fluorescence distribution due to helical flow (adapted with permission from Stroock et al. 2002).

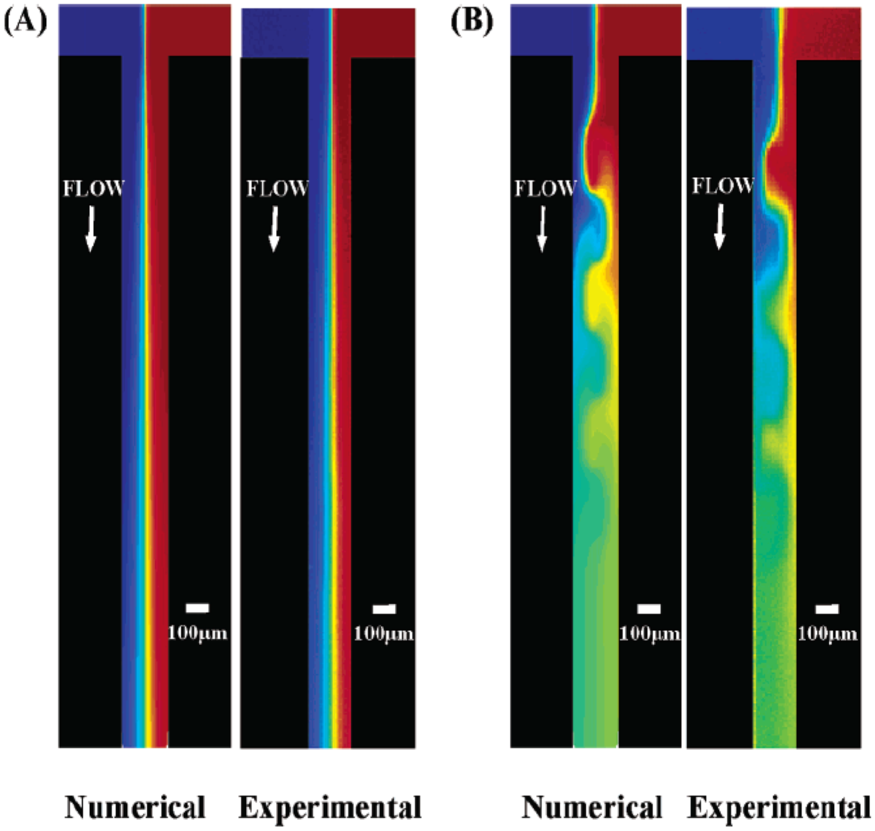

Figure 3.2: (a)Numerical and experimental results for T-mixer and (b) Numerical and experimental results for heterogeneously charged bottom mixer at E = 280 V/ cm (adapted with permission from Bidiss et al. 2002).

As the surface properties of the microchannel governs the electro-osmotic flow characteristics (Stroock and Whitesides 2003), surface heterogeneity (non-uniform zeta potentials) can be exploited to generate vortices or specific flow structures to improve the mixing performance. Ajdari (1995) theoretically investigated the generation of recirculation regions within the bulk flow near the heterogeneously charged region and this phenomenon was validated experimentally (Stroock et al. 2000). Several other studies utilized non-uniform heterogeneous zeta potential distribution (Chang and Yang 2004; Erickson and Li 2002; Fushinobu and Nakata 2005) to achieve enhanced micromixing at the expense of reduced flow rate (Tian et al. 2005). Later, Biddiss et al. (2004) demonstrated superior mixing in T-mixer with a non-uniform zeta potential distribution on the bottom of the T- microchannel, as shown in Figure 3.2.

Beside geometric and surface variations, modifications in the sample injection strategy have also been utilized to enhance the mixing performance. Several studies have identified pulsing/ perturbation in velocities as an efficient active mixing scheme for pressure driven flows (Glasgow and Aubry 2003; Glasgow et al. 2004; Niu and Lee 2003; Dodge et al. 2005). In electrokinetic mixing, similar idea was studied by Fu et al. (2005) using periodic injection of samples from four inlets. Another study based on similar idea involves sequential injection of samples followed by expansion chamber (Coleman et al. 2006; Coleman and Sinton 2005) as shown in Figure 3.3. Recently, Lim et al. (2010) have shown mixing improvement with periodic EOF in T-mixer with a physical constriction

(Figure 3.4). All of these mixing schemes increase the interfacial contact area by generating alternate bands of solute and sample in series, as shown in Figures 3.3 and 3.4. Several other electrokinetic micro-mixers were reported based on DC electrokinetic instability (Oddy et al. 2001; Lin et al. 2004), dielectrophoresis (Lee et al. 2001; Deval et al. 2002), AC electro-osmosis (Lastochkin et al. 2004; Wang et al. 2006), electro-wetting on dielectric (Paik et al. 2003a; Paik et al. 2003b) etc. An excellent description of electrokinetic mixing techniques is available in a recent review (Chang and Yang 2007).

3.3 Proposed Design & Mathematical Model

The top view of the proposed design is shown in the Figure 3.5, where Ω_1 & Ω_2 represent the fluid and metallic domain, respectively. The design consists of *n* pairs of metallic half-cylinders, of radius *a*, embedded on opposite sides of the channel wall. The metallic half-cylinders are assumed to be uncharged and ideally polarizable, so that Faradaic reactions (electro-chemical reactions at the metal-electrolyte interface where electrons are transferred between the two phases by reduction or oxidation of ions in the electrolyte medium) at the interface are negligible. Further, the shape of the conducting obstacle is arbitrarily chosen to demonstrate the mixing enhancement using ICEO. As the induced zeta potential is dependent on the geometry of obstacle, the shape of the obstacle does influence the mixing performance and optimization problem can be formulated for obtaining optimal obstacle shape.

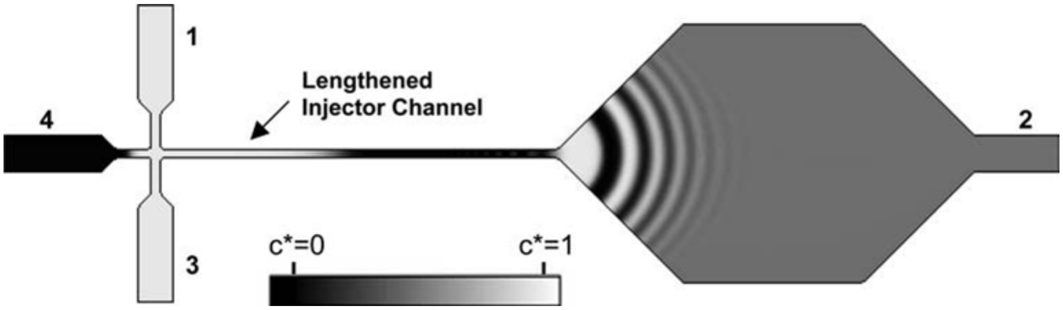

Figure 3.3: Sequential injection followed by expansion chamber (adapted with permission from Coleman and Sinton 2005).

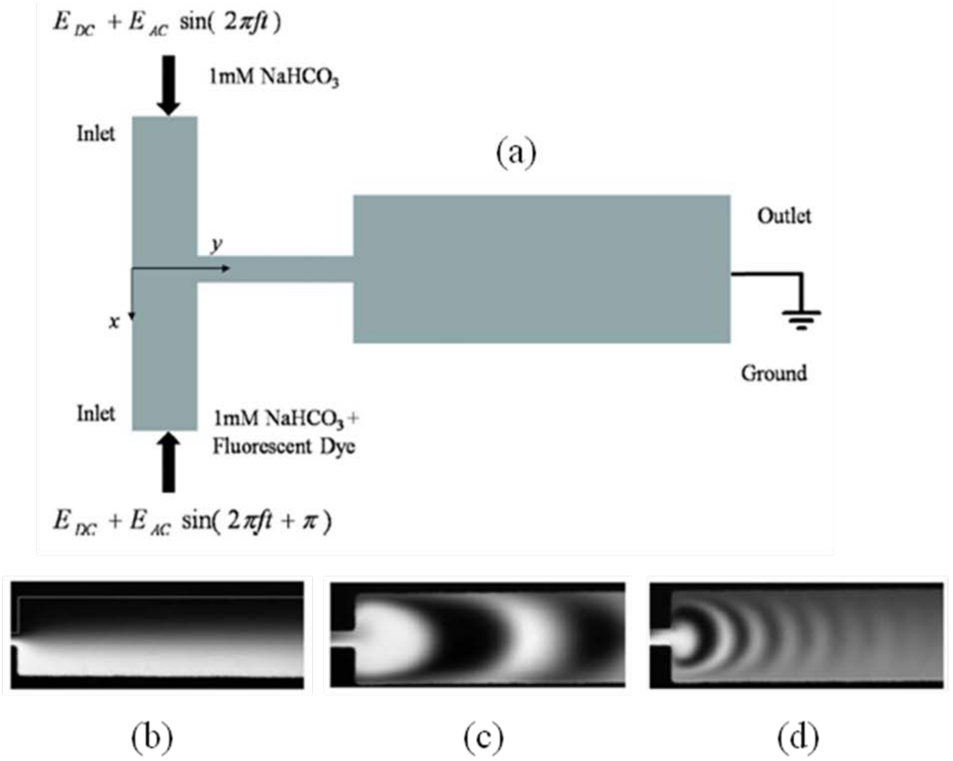

Figure 3.4: (a) Schematic for generating periodic EOF through microchannel with constriction; (b) With DC field (E_{dc} = 258 V/cm); (c) with E_{ac} = 4/3 times of E_{dc} and frequency = 2.1 Hz and (d) with E_{ac} = 4/3 times of E_{dc} and frequency = 8.1 Hz (adapted with permission from Lim et al. 2010).

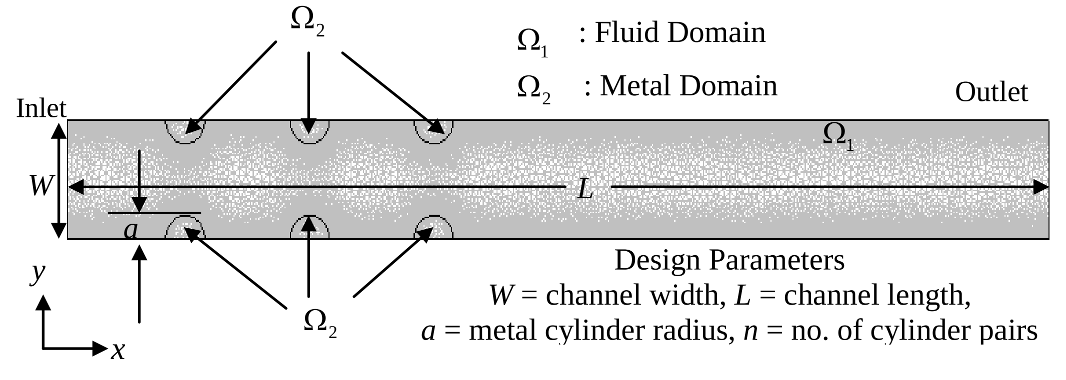

Figure 3.5: Top-view of the proposed design.

As pointed out earlier, proposed design is directly influenced by the observation of transverse flow and vortices in the vicinity of polarizable conducting cylinder (Bazant and Squires 2004). The FCEO and ICEO flow characteristics can be understood by considering a schematic of the proposed design as shown in Figure 3.6. If we apply an electric field in the axial direction, there will be induced charges proportional to the magnitude of the applied field on the metal surface as shown in the Figure 3.6. The fixed negative charge on the non-conducting wall will cause axial flow, while the electric field will act on the induced charges to generate flow in the transverse direction due to ICEO.

The FCEO/axial flow is dictated by the value of fixed zeta potential ς_{fix} whereas the ICEO/ transverse flow is dependant upon the magnitude of induced zeta potential ς_{ind}. Therefore any design parameter which enhances the ICEO flow component or induced charge/induced potential on the metal surface will result in better mixing performance. Also the surface charge density q_s is related to the small values of zeta potential (fixed or induced) as follows:

$$q_s = \varsigma \, \varepsilon_0 \varepsilon_m \kappa \tag{3.1}$$

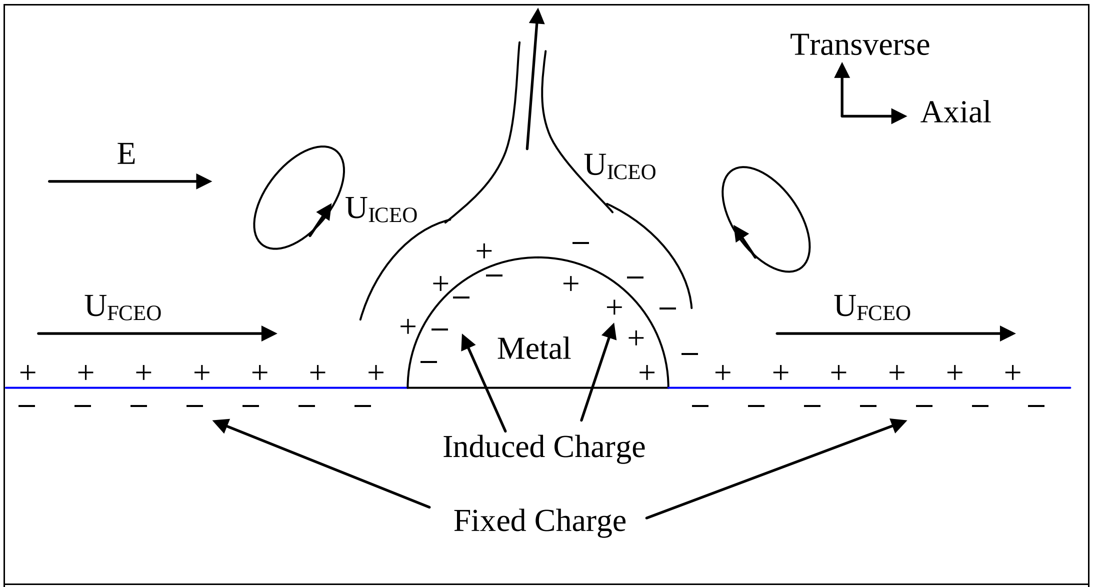

Figure 3.6: Schematic showing charge distribution and flow for a sub-section of proposed ICEO mixer.

A 1:1 electrolyte is used in the simulation with constant diffusivity D for both types of ions. Also, the solution is assumed to be an incompressible Newtonian fluid with constant dielectric constant ε_r, viscosity μ and density ρ. The channel walls are negatively charged, and the metal surface will acquire surface charge as an electric field is applied in the *x* direction. Unless otherwise specified, all default parameter values used in the simulation are summarized in the Table 3.1.

To describe the mathematical model, we introduce the following reference quantities and dimensionless variables:

$$L_{ref} = W,\ \psi_{ref} = \frac{K_b T}{ze},\ c_{ref} = c_{0,}\ \ E_{ref} = \frac{\psi_{ref}}{L_{ref}},\ u_{ref} = \frac{\varepsilon_0 \varepsilon_r \psi_{ref}}{\mu} E_{ref} \quad \&$$

$$\bar{x} = \frac{x}{L_{ref}},\ \bar{y} = \frac{y}{L_{ref}},\ \bar{\psi} = \frac{\psi}{\psi_{ref}},\ \bar{c}_i = \frac{c_i}{c_{ref}},\ \bar{u} = \frac{u}{u_{ref}},$$

$$\bar{E} = \frac{E}{E_{ref}},\ \bar{p} = \frac{p}{\rho u_{ref}^2},\ \bar{q}_s = \frac{q_s L_{ref}}{\varepsilon_0 \varepsilon_r \psi_{ref}},\ \bar{t} = \frac{t u_{ref}}{L_{ref}}$$

In the fluid domain, the Poisson equation is used to relate the electric potential ψ to the charge densities. In its non-dimensional form, the Poisson equation is:

$$\bar{\nabla} \cdot (-\bar{\nabla} \bar{\psi}) = \frac{1}{2} \kappa^2 W^2 (\bar{c}_1 - \bar{c}_2) \tag{3.2}$$

The above equation relates the electric potential to the volumetric charge densities. In the above equation, $\overline{\nabla}$ is the dimensionless gradient operator, *W* is the channel width, $\overline{c}_1$ and $\overline{c}_2$ are the scaled concentration of positive and negative electrolyte ion respectively and κ is the inverse of Debye length given by

$$\kappa = \left(\frac{2z^2 e^2 N_A c_0}{\varepsilon_0 \varepsilon_r K_b T} \right)^{\frac{1}{2}} \tag{3.3}$$

In equation 3.3, *z* is the valence of the electrolyte ions, *e* is the elementary charge, N_A is the Avogadro number, c_0 is the bulk electrolyte concentration and K_b, T, ε_0 represent Boltzmann constant, absolute temperature and permittivity of free space.

As the electrolyte ions cannot penetrate inside the metal cylinders, the electric potential distribution is given by the Laplace equation inside the metal domain:

$$\overline{\nabla} \cdot (-\overline{\nabla}\,\overline{\psi}) = 0 \tag{3.4}$$

The flow field in the fluid domain is governed by the continuity and Navier-Stokes equations. These equations, in their dimensionless forms, are:

$$Re(\overline{\boldsymbol{u}} \cdot \overline{\nabla}\overline{\boldsymbol{u}}) = -\overline{\nabla}\overline{p} + \overline{\nabla} \cdot (\overline{\nabla}\overline{\boldsymbol{u}}) - \frac{1}{2}\kappa^2 W^2 (\overline{c}_1 - \overline{c}_2)\overline{\nabla}\,\overline{\psi} \tag{3.5a}$$

$$\overline{\nabla} \cdot \overline{\boldsymbol{u}} = 0 \tag{3.5b}$$

In the equation 3.5a, the rightmost term is due to the electrical body force within EDL and *Re* is the Reynolds number (ratio of inertial forces to viscous forces) and can be written as:

$$Re = \frac{L_{ref} u_{ref} \rho}{\mu} = \frac{\varepsilon_0 \varepsilon_r W K_b T \rho}{ze\mu^2} \tag{3.6}$$

A steady state ion conservation equation can be written for electrolyte ions in domain 1, with the Peclet number P_e (ratio of convective transport to diffusive transport) appearing with the convective term as

$$Pe(\overline{\boldsymbol{u}} \cdot \overline{\nabla} \overline{c}_i) = \overline{\nabla} \cdot (\overline{\nabla} \overline{c}_i) + \overline{\nabla} \cdot (\overline{c}_i \overline{\nabla}\, \overline{\psi}) \tag{3.7}$$

The Peclet number is defined as

$$Pe = \frac{u_{ref} L_{ref}}{D} = \frac{\varepsilon_0 \varepsilon_r (K_b T)^2}{\mu D (ze)^2} \tag{3.8}$$

Further, the steady transport of the species is governed by the convection-diffusion equation and can be written in dimensionless form as:

$$(\overline{u} \cdot \overline{\nabla} \overline{c}_s) = \overline{\nabla} \cdot (\overline{\nabla} \overline{c}_s) \frac{D_s}{u_{ref} L_{ref}} \tag{3.9}$$

In the above equation, $\bar{c}_s$ and D_s represent species concentration and diffusion coefficient, respectively.

The above model is solved using the direct (UMFPACK) solver available within the commercial finite element method package, COMSOL 3.2. The boundary conditions used in the simulation are shown with the help of Figure 3.5. At the channel inlet, a constant potential V_0 relative to the outlet potential is applied, giving rise to a steady electric field E in the x direction. Also, a constant surface charge density q_s is imposed on the non-conducting channel walls and potential continuity is applied at the metal-fluid interface. Considering an initially uncharged cylinder, the interfacial boundary condition can be written as $n.(D_1\text{-}D_2) = 0$, as used by Zhao and Bau (2007b). For fluid flow, zero pressure conditions are imposed at the inlet and outlet, while the no slip condition is imposed at fluid-solid boundaries. Similarly, zero flux condition is imposed at the channel walls including metal surface for electrolyte ions. For species transport, a constant concentration condition is imposed at the channel inlets (i.e. scaled concentration of 1 and 0 at inlet 1 and inlet 2 respectively). The aforementioned condition is implemented at the inlet boundary using a smoothed Heaviside function (with continuous second derivative). Further, it is assumed that species concentration is sufficiently low such that it doesn’t affect the flow profile. At the conducting surfaces and non-conducting channel walls, zero flux condition is imposed for the species, while convective-flux only boundary condition is applied at the channel outlet.

The mixing performance is quantified using the following mixing index; it is usually calculated based on the concentration profile at any particular cross-section, as done by various authors (Coleman and Sinton 2005):

$$\eta = \left[1 - \frac{\sqrt{\frac{1}{N} \sum_{1}^{N} \left(\overline{c}_s - \overline{c}_s^{*} \right)^2}}{\sqrt{\frac{1}{N} \sum_{1}^{N} \left(\overline{c}_s^{0} - \overline{c}_s^{*} \right)^2}} \right] \tag{3.10}$$

In the above equation, N is the number of points in the cross-section used for estimation of the mixing index. The variable $\overline{c}_s$ represents the scaled local concentration, while $\overline{c}_s^{0}$ and $\overline{c}_s^{*}$ are the scaled concentration at each point if the solutions were unmixed and perfectly mixed (i.e. 0.5), respectively. Also, it should be noted that the variable $\overline{c}_s^{0}$ takes on a values of 0 or 1 at any point across the channel width, resulting in a constant denominator value of 0.5 in equation 3.10. The cross-sectional plot in Figure 3.5(a) shows the concentration profile at the channel inlet. Intermediate values of η are shown with corresponding concentration profiles in Figure 3.7 (b). On the other hand, a value of $\eta = 1$ represents perfect mixing, where the concentration is 0.5 everywhere across the channel width as shown in Figure 3.7 (c). Based on the mixing index definition (equation 3.10), the theoretical limits for η is between zero and one.

For the cases where perfect mixing are achieved at lengths less than the channel length, the above index is not appropriate as it does not account for mixing length L_{mix}. Here L_{mix} is assumed to be the length where 99% mixing is achieved, i.e. the length at which $\eta > 0.99$. Therefore, we propose the use of a modified mixing index as described by the equation below:

$$\eta' = \begin{cases} \left[1 - \dfrac{\sqrt{\frac{1}{N}\sum_{1}^{N}\left(\overline{c}_s - \overline{c}_s^*\right)^2}}{\sqrt{\frac{1}{N}\sum_{1}^{N}\left(\overline{c}_s^0 - \overline{c}_s^*\right)^2}} \right]_L, when\ L_{mix} > L \\ \left[1 - \dfrac{\sqrt{\frac{1}{N}\sum_{1}^{N}\left(\overline{c}_s - \overline{c}_s^*\right)^2}}{\sqrt{\frac{1}{N}\sum_{1}^{N}\left(\overline{c}_s^0 - \overline{c}_s^*\right)^2}} \right]_L * \dfrac{L}{L_{mix}}, when\ L_{mix} < L \end{cases} \tag{3.11}$$

The modified mixing index incorporates the mixing length into the conventional definition. For example a value of $\eta' = 2$ represents $L_{mix} = 0.5L$, i.e. desired mixing is achieved at half of the channel length. Based on the above definitions, the theoretical limits for η is from zero to one; for η', the limits are from zero to infinity. Therefore a value of η' greater than 1 suggests that 99% mixing is achieved in less than L and there is a scope of length reduction/ chip portability without sacrificing mixing performance. The usefulness of the modified mixing index is demonstrated through case studies presented in the results section.

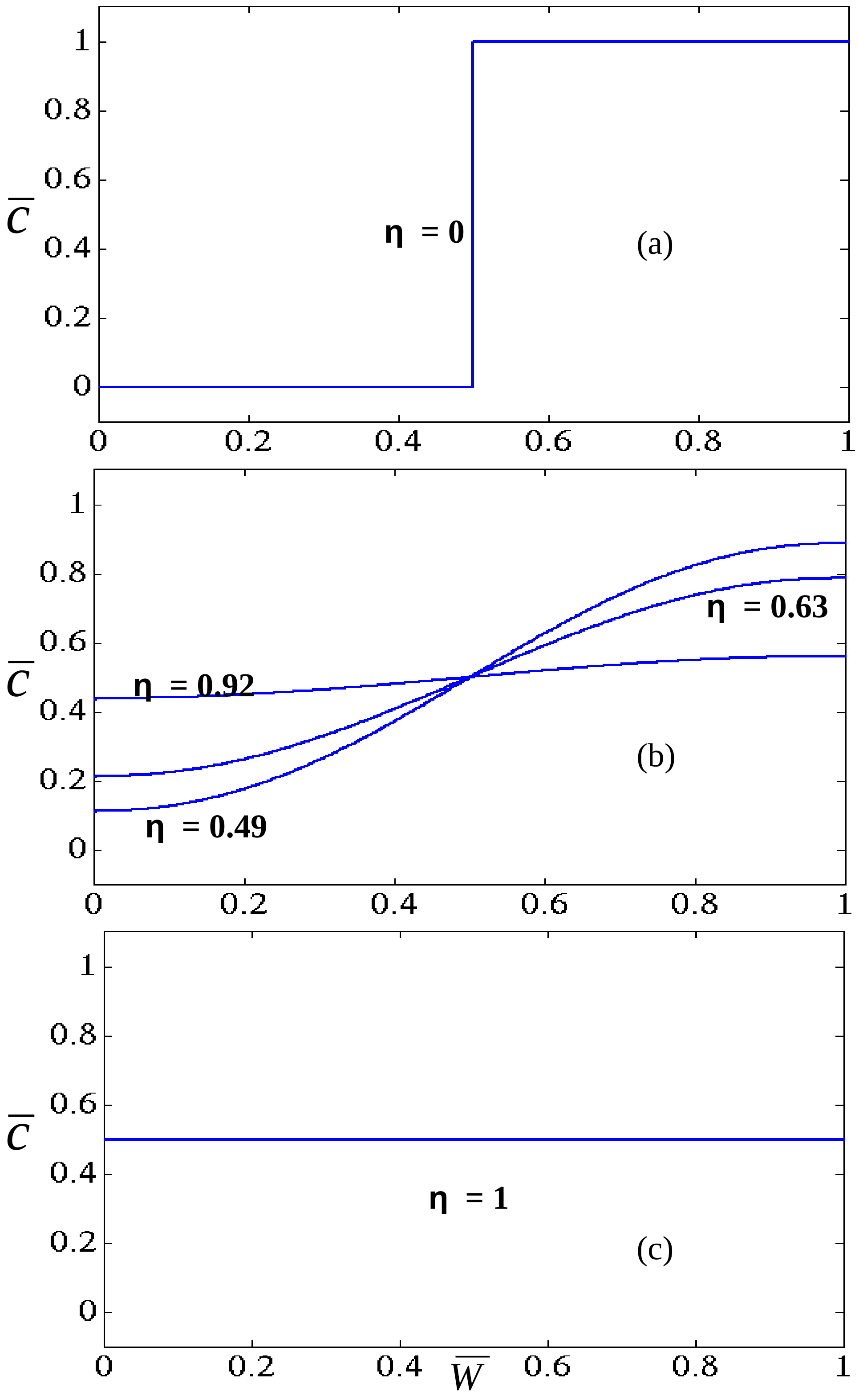

Figure 3.7: Concentration profiles for various η values (a) $\eta = 0$ corresponds to perfectly unmixed state; (b) Intermediate states & (c) $\eta = 1$ corresponds to perfectly mixed state.

Table 3.1: Simulation Parameters (default values)

Parameter	**Value**	**Description**
W	10 μm	Width of the microchannel
L_c	100 μm	Length of microchannel
ς_f	In range of −5 *mv* to −50 *mv*	Fixed zeta potential on non-conducting channel walls
κ^{-1}	100 *nm*	Debye length
D	1e−9 m^2/s	Diffusivity of electrolyte ions
D_s	1e−11 m^2/s	Diffusivity of species to be mixed
E	125 *V/cm*	Applied electric field

3.4 Results and Discussion

We begin with the study of electrolyte-ion concentration and velocity profile in the proposed design. Figure 3.8 presents the case with $\overline{q}_s$ = 20 (which corresponds to ς_{fix}~5mv) and ς_{ind}~25mv. Based on the discussion presented earlier, with induced zeta potential higher than the fixed zeta potential, the ICEO flow will dominate in the vicinity of conducting semi-cylinder.

Figure 3.8a shows the surface plot of α, where $\alpha = \overline{c}_1 - \overline{c}_2$ (i.e. the difference between positively and negatively charged electrolyte ion concentrations. The variable α represents the excess charge and takes on positive and negative values at the left and right half of the semi-cylinder, respectively (due to induced charges). Also, a cross-sectional plot for α is shown in Figure 3.8b for the line shown in Figure 3.8a. As evident from Figure 3.8b, the value of α goes to zero outside the EDL, confirming electro-neutrality outside the EDL. The Figures 3.8c shows the velocity streamlines near the conducting obstacle. The above-mentioned figures suggest that the ICEO flow is dominant as compared to FCEO flow under these operating conditions.

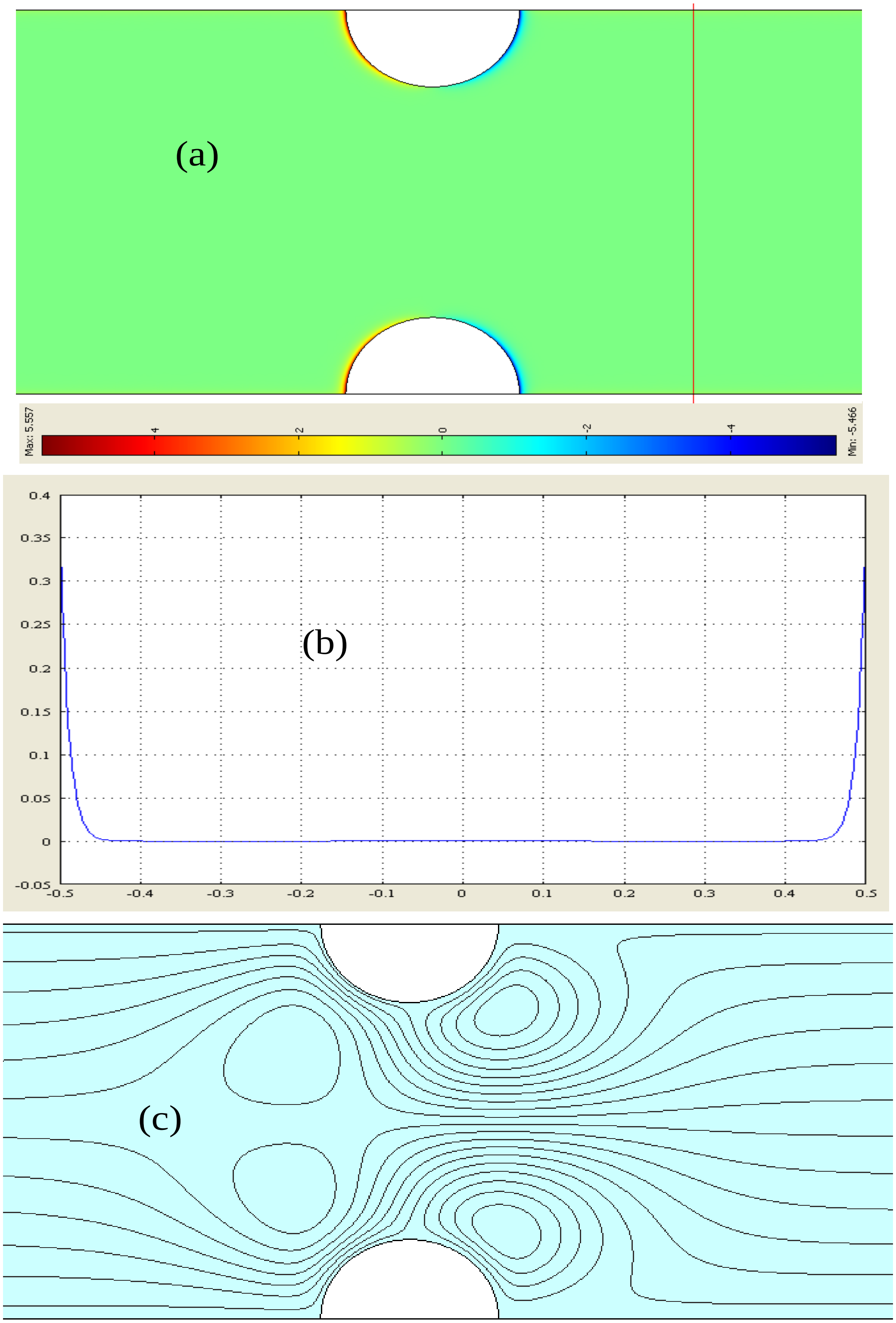

Figure 3.8: (a) α surface plot (b) α cross-section plot and (c) velocity streamlines around the metal cylinder pairs for $\overline{q}_s$ = 20 and ς_{ind} ~25mv (default parameters).

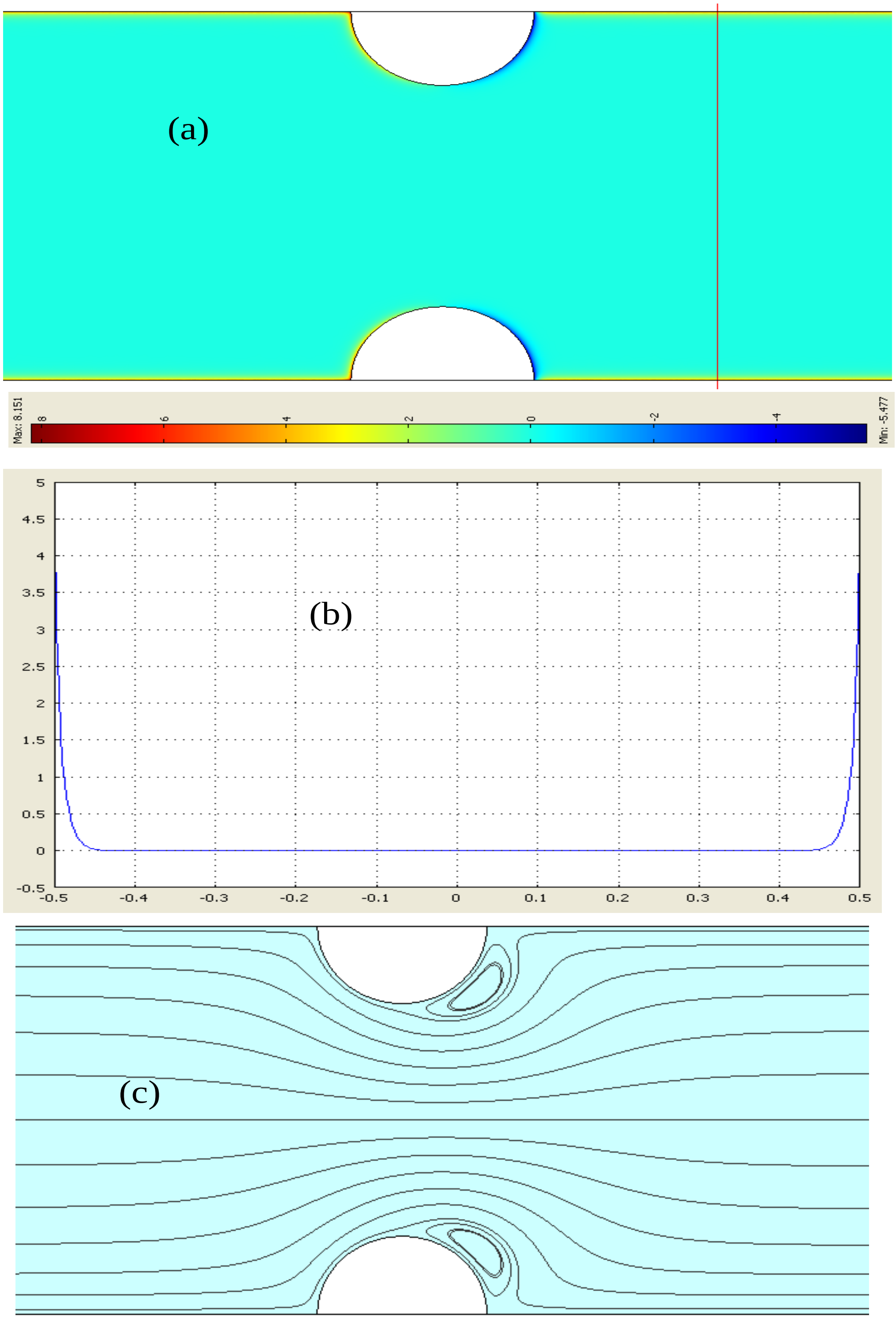

Figure 3.9: (a) α surface plot (b) α cross-section plot and (c) velocity streamlines around the metal cylinder pairs for $\overline{q}_s$ = 200 and ς_{ind} ~25mv (default parameters).

Figures 3.9a to 3.9c show plots similar to Figure 3.8 under comparable conditions except for $\overline{q}_s$, which is equal to 200 (10 times higher than the previous value). By increasing the fixed surface charge density, we are essentially enhancing the FCEO flow, which is evident from the velocity streamline plot shown in Figure 3.9c. By comparing Figure 3.8 to Figure 3.9, we can conclude that with increasing FCEO flow, the ICEO vortices reduce in size and the vortices on the left of the semi-cylinder disappear due to increased axial flow.

Next, we will analyze the effect of various parameters on the mixing index. Figure 3.10 shows the effect of cylinder radius *a* on mixing performance. As we increase the radius (with all other parameters kept constant), the induced potential on the metal surface increases (as shown in Figure 3.11), which in turn enhances the transverse flow in the channel. Therefore, while the modified mixing index is 1.03 for traditional channel, η' = 1.42 (corresponding to L_{mix} = 7.04) and η' = 6.66 (corresponding to L_{mix} = 1.50) for a = 0.2W and a = 0.4W, respectively. The proposed modified mixing index is found to be adequate and insightful for characterizing mixing. The modified mixing index for different metal cylinder radius is also calculated using correction method so as to facilitate the comparison with Wu's approach. For a = 0.2W, 0.3W and 0.4W, the modified mixing index (using correction method) is found to be 1.40, 3.25 and 6.74 respectively. The above result indicate good agreement between the full Poisson-Nernst-Planck approach and slip-velocity approach.

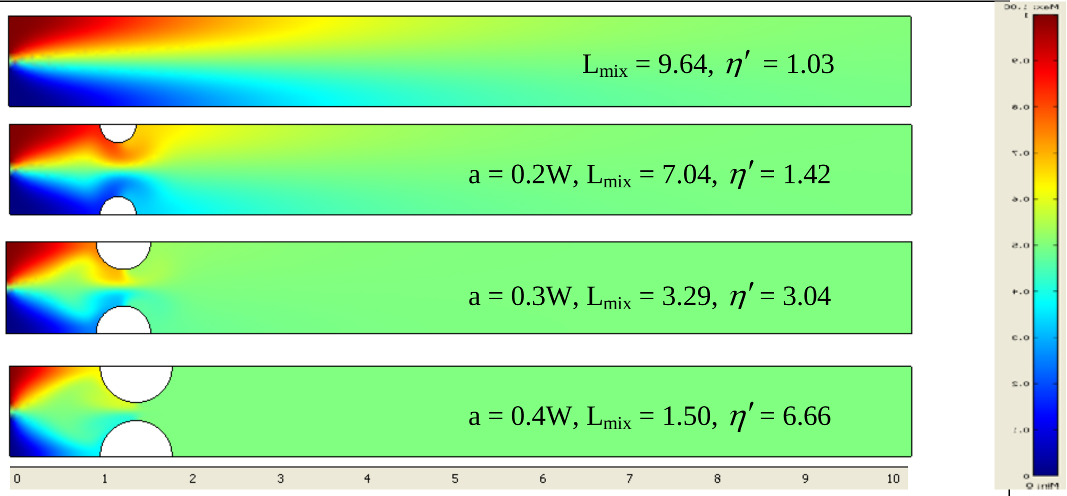

Figure 3.10: Effect of metal cylinder radius on mixing performance index at $\bar{q}_s$ = 20 (E = 62.5 *V/cm* and default parameters).

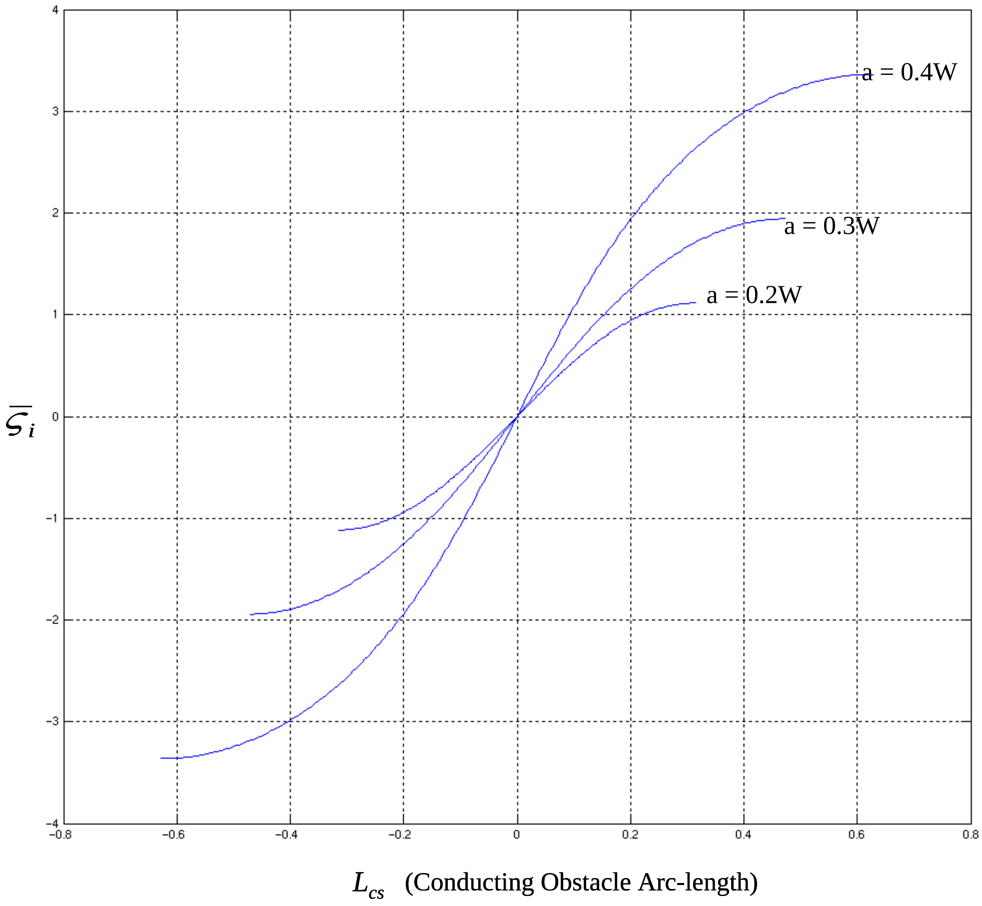

Figure 3.11: Variation of induced zeta potential with metal cylinder radius.

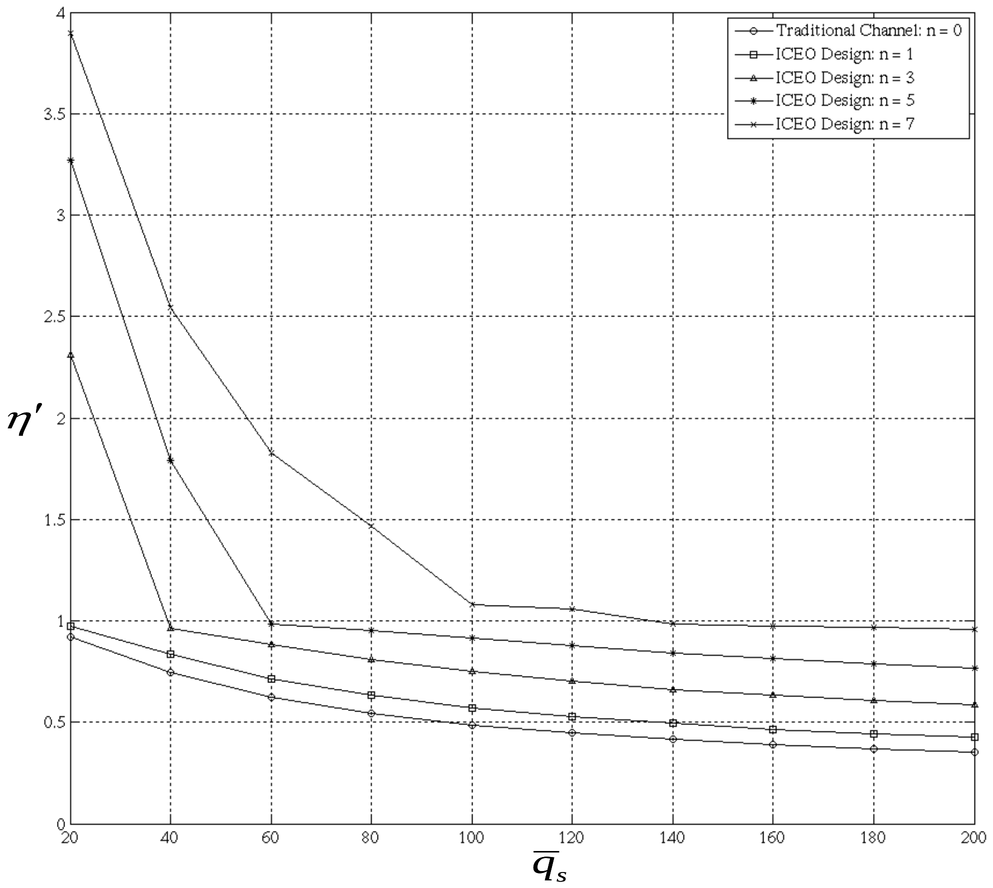

Figure 3.12: Effect of number of cylinder pairs on mixing performance index at various fixed surface charge density (default parameters).

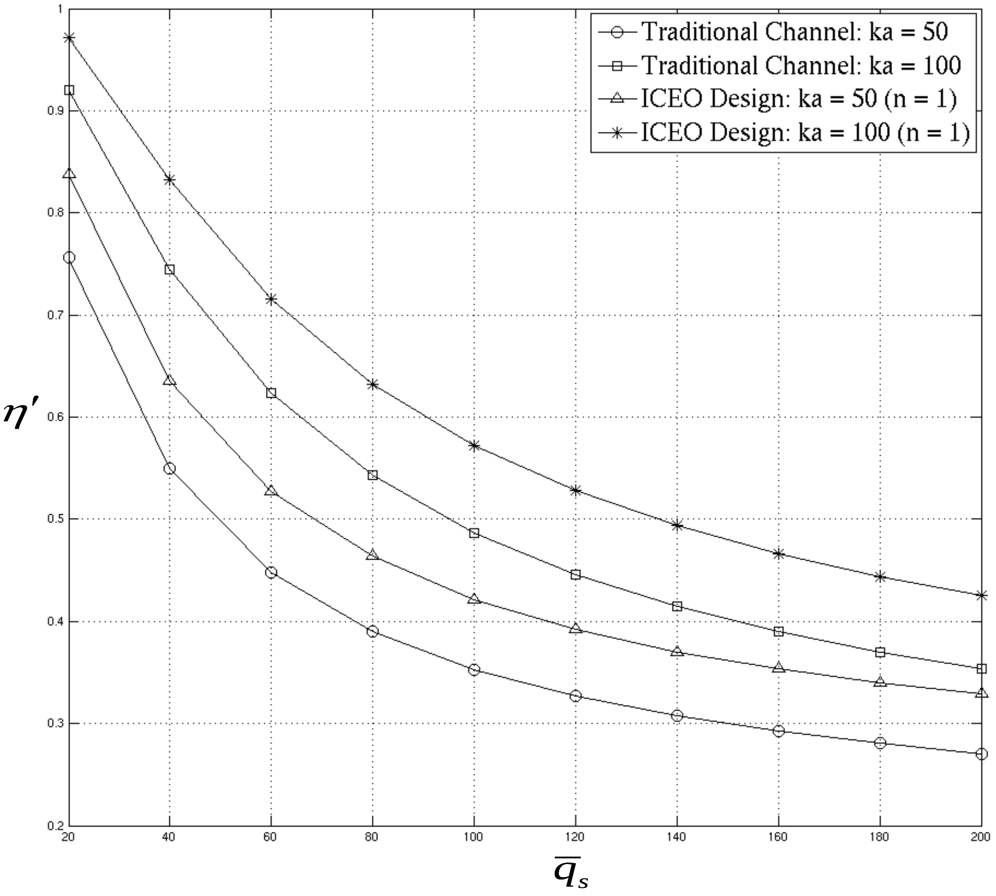

Figure 3.13: Effect of EDL thickness on mixing performance at various fixed surface charge density (default parameters).

In Figure 3.12, we show the effect of increasing the number of cylinder pairs on the mixing index. By increasing the number of cylinder pairs, the number of mixing units in the channel is effectively increased. Therefore mixing will be enhanced with the number of cylinder pairs as shown in Figure 3.12. Next, the effect of EDL thickness on mixing performance is explored. With a fixed surface charge density, if we increase the EDL thickness, the corresponding zeta potential increases (equation 3.1). Therefore, mixing performance deteriorates as we go from κW = 100 to κW = 50, as shown in Figure 3.13. However, in both cases, the ICEO mixer performs better than the traditional mixer with a = 0.2W, and performance will enhance with the increase of a.

3.5 Summary

A novel strategy for mixing in micro-devices, which utilizes induced charge electro-osmosis (ICEO), is proposed. We have demonstrated via numerical simulation that ICEO offers a promising technique for localized charge variation/control and can be exploited to generate various kinds of flow patterns in micro-devices. In this particular study, micro-vortices can be generated in the micro-channel which enhances mixing performance. The effect of design parameters on mixing performance is analyzed for the proposed design. Also, a modified mixing index is introduced and is shown to be useful for case studies where perfect mixing is achieved within the lengths less than the channel length. In all cases that were explored, the proposed ICEO - based mixer proved to be a better design as compared to the T-mixer.

Chapter 4

Induced Charge Electro-Osmotic Mixer: Obstacle Shape Optimization[#]

4.1 Introduction

Efficient Mixing is difficult to achieve in miniaturized devices due to the nature of low Reynolds number flow. Mixing can be intentionally induced, however, if conducting or non-conducting obstacles are embedded within the micro-channel. In case of conducting obstacles, vortices can be generated in the vicinity of the obstacle due to induced charge electro-osmosis (ICEO) which enhances mixing of different streams as shown in the previous chapter. The performance of microdevices including micro-mixers can be optimized using geometric optimization techniques (Griffiths and Nilson 2001; Johnson and Locascio 2002; Lynn and Dandy 2007; Gregersen et al. 2009). In case of ICEO mixers, mixing performance is dependent upon the obstacle shape. The obstacle shape affects the

---

[#] A version of this chapter has been published. [M. Jain, A. Yeung and K. Nandakumar, Biomicrofluidics, 3, 022413 (2009)] induced zeta potential on the conducting surface, which in turn influences the flow profile near the obstacle. In this extension of previous chapter, we seek the optimal shape for a conducting obstacle which provides the best mixing performance. The obstacle boundary is parametrically represented by non-uniform rational B-spline (NURBS) curves. The genetic algorithms (GA) are employed to arrive at the optimal obstacle shape, which maximizes the mixing for given operating conditions. The organization of this chapter is as follows: The following section provides a brief description of the NURBS (non-uniform rational B-spline) curves. Next, the mathematical model and optimization approach used for this numerical study is described. In the results section, the optimal obstacle shape is presented and compared with the other geometric shapes. Finally, the effect of obstacle shape on the tradeoff between flow rate and mixing performance is examined.

4.2 Basics of NURBS

NURBS (non-uniform rational B-spline) curves are the generalization of both Bézier curves and B-splines. It is a piecewise polynomial curve which evolves in a one-variable parametric space, with the parameter typically denoted by u. Any NURBS curve is defined by three components: (a) control points, (b) polynomial degree or curve order, and (c) knot vector. The knot vector divides the parametric space into intervals known as knot spans. A p^{th} degree NURBS curves is defined as follows:

$$C(u) = \sum_{i=1}^{k} \frac{N_{i,p}(u) w_i}{\sum_{j=1}^{k} N_{j,p}(u) w_j} P_i \qquad a \le u \le b$$

$$U = [\underbrace{a,......,a}_{p+1}, u_{p+1}, ..., u_{m-p-1}, \underbrace{b,......,b}_{p+1}] \tag{4.1}$$

In the above equation, k is the number of control points P_i, w_i are the corresponding weights, and $\{N_{i,p}(u)\}$ are the p^{th} degree B-spline basis functions defined on the non-uniform knot vector U. Here, non-uniformity refers to the unequal spacing of the knots u_i within the knot vector. The number of knots in a knot vector (m) is always equal to the number of control points (k) plus the order of the curve, where curve order is defined as the polynomial degree (p) plus one.

From an optimization perspective, NURBS curves are an excellent option as it can represent a variety of shapes with the minimum number of parameters. Other very interesting property of NURBS is the control it offers in attaining the desired degree of smoothness and discontinuity. A NURBS curve can represent smooth surfaces, sharp corners, etc., depending upon the values in the knot vector and control points. A number of same-value knots in the knot vector are referred as a knot with a certain *multiplicity*; this has implications on the continuity of the resulting curve and its higher derivative. The other properties of NURBS curves are *local control*, *strong convex hull property*, etc. Some of the NURBS properties are demonstrated with the help of various figures in the next paragraph.

An extensive description of NURBS curves, their mathematical properties, and examples of application can be found in Piegl and Tiller (1997).

Consider a NURBS curve represented by quadratic polynomials with control points (marked as square) in Figure 4.1(a). The knot vector for Figure 4.1(a) is given by $\{U = [0, 0, 0, 0.2, 0.4, 0.5, 0.6, 0.8, 1, 1, 1]\}$. The NURBS curve in Figure 4.1(a) is smooth, however if we introduce knot multiplicity in the knot vector as follows: $\{U = [0, 0, 0, 0.2, 0.2, 0.5, 0.8, 0.8, 1, 1, 1]\}$, the resulting curve is shown in Figure 4.1(b). The sharp corners are visible near 3rd and 6th control points in Figure 4.1(b). It should be noted, however, that knot multiplicity does not always cause discontinuities in the curve (Piegl and Tiller, 1997). Another property of *local control* of NURBS curve is demonstrated in Figure 4.2. The control point P_7 is moved from (2.9,1) to (3,1) and the resulting NURBS curve is modified locally only as opposed to a Bézier curve where the change in control point leads to a change in the entire curve. This local modification property is also important for shape optimization and it can be used to fine tune the shape locally without changing the shape in a global way. Another approach to fine tune a NURBS curve is to alter the weights associated with the control points.

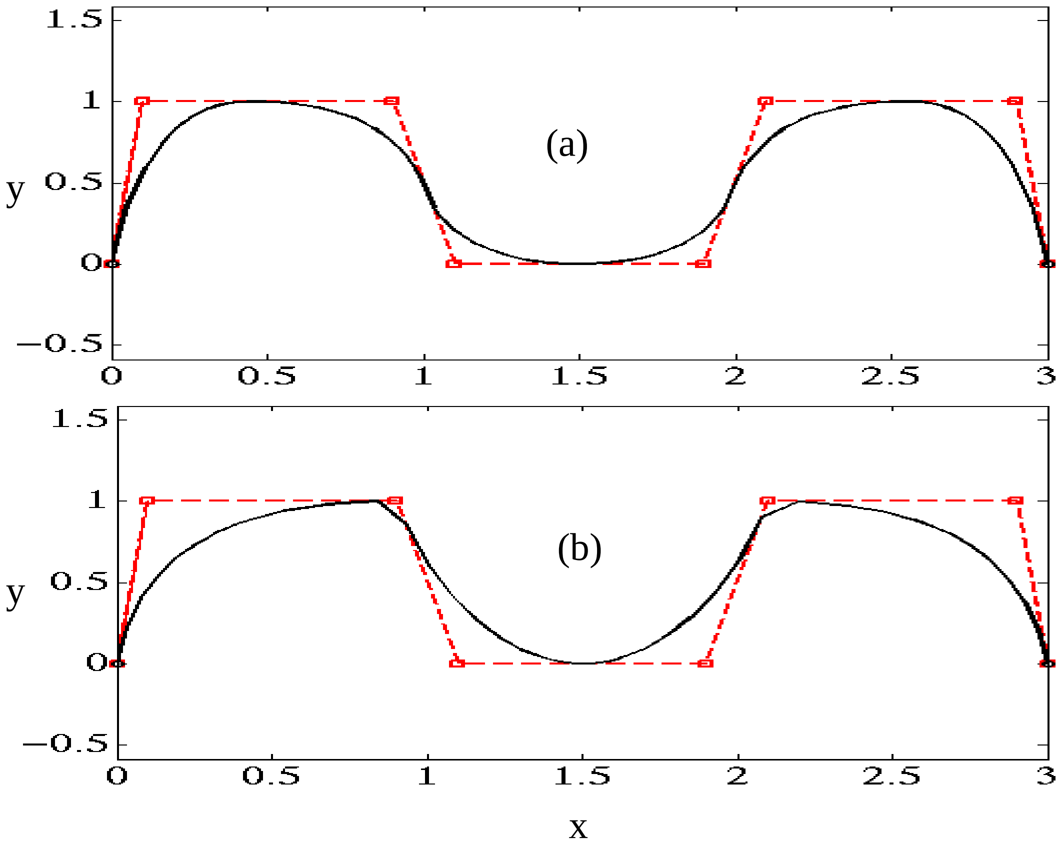

Figure 4.1: Effect of knot multiplicity on NURBS curve (a) smooth curve (b) non-smooth curve with sharp corners around P_3 and P_6 control points.

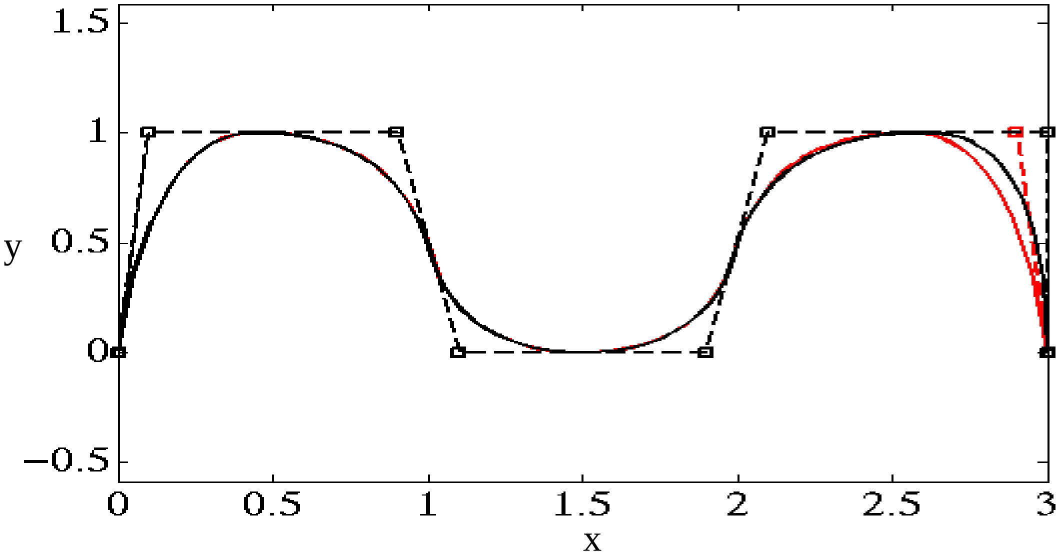

Figure 4.2: Local control property for a NURBS curve demonstrated as local modification is observed when control point P_7 is moved from (2.9,1) to (3,1).

4.3 Optimization Approach & Mathematical Model

The ICEO micro-mixers can be modeled using either full PNP model or using slip velocity model as mentioned in previous chapter. The Poisson-Nernst-Planck (PNP) model resolves the electric double layer and solves for electrolyte ion concentration distributions. We utilized this in the last chapter for modeling steady ICEO flow. The Correction method, proposed by Wu and Li (2008a and b), is a numerical approach for estimating the induced zeta potential on a conducting surface and further utilizes it to estimate the slip velocity at a conducting surface (adopting the Smoluchowski limit for thin EDL). Though the Poisson-Nernst-Planck model can be used for both thin and thick EDL and accounts for surface conduction, it is very much computationally intensive as compared to the Correction method. Since optimization problem requires repeated solutions of ICEO flow problem, the Correction method proposed by Wu and Li (2008a) is used in this study. When compared to PNP model, correction method provides equivalent results for smaller field strengths/ induced zeta potential values. Recently, Wu and Li (2008b) reported a reasonable agreement between experimental data and numerical modeling results based correction potential modeling approach.

The problem domain can be reduced from a 3D problem to a 2D problem using the assumption of homogeneous non-conducting top and bottom channel walls (Wu and Li 2008a). The top view of the ICEO mixer design is shown in the Figure 4.3. The design consists of a pair of conducting obstacles embedded on opposite sides of the channel wall. The shape of the conducting surface is represented by the NURBS curve and it can take on any arbitrary shape within the envelope (shown by dashed lines in Figure 4.3). The end points of the NURBS curve are fixed, whereas the co-ordinates of other control points, their weights and knot vector values are chosen as parameters to be optimized. The details of the optimization methodology will be discussed later in this section.

The conducting surface is assumed to be uncharged and highly polarizable, so that Faradaic reactions (i.e. electro-chemical reactions at the metal-electrolyte interface where electrons are transferred between the two phases by reduction or oxidation of ions in the electrolyte) at the interface are negligible. Also, the solution is assumed to be an incompressible, Newtonian fluid with fixed dielectric constant ε_r, viscosity μ, and density ρ. The channel walls are negatively charged, and the metal surface will acquire surface charges as an electric field is applied in the *x* direction. Unless otherwise specified, all default parameter values used in the simulation are summarized in the Table 4.1.

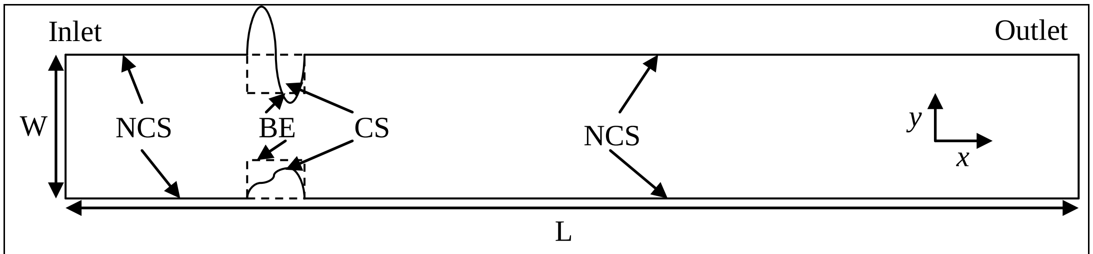

W: channel width, L: channel length, CS: conducting Surface (NURBS curve)
BE: bounding envelope for NURBS, NCS: non-conducting surface

Figure 4.3: Top-view of the proposed conducting obstacle micro-mixer design. The bounding envelope for NURBS curve is represented by dashed lines.

To describe the mathematical model, we introduce the following reference quantities and dimensionless variables:

$$L_{\text{ref}} = W, \quad \psi_{\text{ref}} = \frac{K_b T}{ze}, \quad c_{\text{ref}} = c_{0,} \quad E_{\text{ref}} = \frac{\psi_{\text{ref}}}{L_{\text{ref}}}, \quad u_{\text{ref}} = \frac{\varepsilon_0 \varepsilon_r \psi_{\text{ref}}}{\mu} E_{\text{ref}} \text{ , and}$$

$$\bar{x} = \frac{x}{L_{ref}}, \quad \bar{y} = \frac{y}{L_{ref}}, \quad \bar{\psi} = \frac{\psi}{\psi_{ref}}, \quad \bar{u} = \frac{u}{u_{ref}}, \bar{E} = \frac{E}{E_{ref}}, \quad \bar{p} = \frac{p}{\rho u_{ref}^2}, \quad \bar{t} = \frac{t\, u_{ref}}{L_{ref}}$$

Here K_b, T, ε_0 represent Boltzmann constant, absolute temperature and permittivity of free space whereas *z* is the valence of the electrolyte ions and *e* is the elementary charge.

Assuming thin EDL, the electric potential distribution at steady state can be described using the Laplace equation with the assumption of uniform bulk conductivity. In non-dimensional form, the Laplace equation is

$$\bar{\nabla}^2 \bar{\psi} = 0 \tag{4.2}$$

In the above equation, $\bar{\nabla}$ is the scaled gradient operator and $\bar{\psi}$ is the scaled electrical potential. At the channel inlet, a constant potential V_0 relative to the outlet potential is applied, giving rise to a steady electric field E in the *x* direction and at the channel as well as the obstacle surface, normal component of electric field is specified as zero i.e. $n.\nabla \psi = 0$.

The flow field in the computational domain is governed by the continuity and Navier-Stokes equations. These equations, in their dimensionless forms, are

$$Re(\overline{u} \cdot \overline{\nabla}\overline{u}) = -\overline{\nabla}\overline{p} + \overline{\nabla}^2\overline{u} \tag{4.3a}$$

$$\overline{\nabla} \cdot \overline{u} = 0 \tag{4.3b}$$

In the above equations, *Re* is the Reynolds number (ratio of inertial to viscous forces) and can be written as

$$Re = \frac{L_{ref} u_{ref} \rho}{\mu} = \frac{\varepsilon_0 \varepsilon_r W K_b T \rho}{ze\mu^2} \tag{4.4}$$

It should be noted that the electrical force term in the Navier-Stokes equation is accounted by the slip velocity boundary condition as given by the Smoluchowski's equation:

$$\overline{u} = \overline{\varsigma}\,\overline{E} \quad \text{where} \quad \left\{ \begin{array}{c} \overline{\varsigma} = \overline{\varsigma}_f \text{ at non - conducting surface} \\ \overline{\varsigma} = \overline{\varsigma}_i \text{ at conducting surface} \end{array} \right\} \tag{4.5}$$

In the above equation, ς_f is the fixed zeta potential on the non-conducting surface, whereas ς_i is the induced zeta potential on the conducting surface; the magnitude of ς_i is dependent on the applied electric field as well as on the obstacle shape. The steady state induced zeta potential is estimated using the

Correction method (Wu and Li 2008a) which is briefly described hereafter. At steady state, induced field on the conducting surface should be equal in magnitude and opposite in direction to the externally applied field, i.e.

$$E_i = - E \qquad \Rightarrow \qquad \nabla \varsigma_i = - \nabla \psi \tag{4.6}$$

Upon integration the above equation yields the following relation:

$$\bar{\varsigma}_i = -\overline{\psi} + \overline{\psi}_c \tag{4.7}$$

Here ψ_c is the constant correction potential, which can be estimated using charge conservation on the conducting surface. Also the surface charge density q_s is linearly related to the small values of zeta potential as $q_s = \varsigma\, \varepsilon_0 \varepsilon_m \kappa$, where κ is the inverse of Debye length. Using the above relation, charge conservation equation for the conducting surface can be written as follows:

$$\int_s \varsigma_i dA = 0 \tag{4.8}$$

Using equations 4.7 and 4.8, we can obtain the following relation for correction potential ψ_c:

$$\psi_c = \frac{\int_s \psi \, dA}{A} \tag{4.9}$$

In the above equation, *A* represents the surface area of the conducting obstacle.

The steady transport of species is governed by the convection-diffusion equation and can be written in dimensionless form as

$$Pe(\overline{u} \cdot \overline{\nabla} \overline{c}) = \overline{\nabla}^2 \overline{c} \tag{4.10}$$

The Peclet number Pe is defined as

$$Pe = \frac{u_{ref} L_{ref}}{D} = \frac{\varepsilon_0 \varepsilon_r \left(K_b T\right)^2}{\mu D (ze)^2} \tag{4.11}$$

The above model is solved using the direct (UMFPACK) solver available within the commercial finite element method package, COMSOL 3.3. For fluid flow, zero pressure conditions are imposed at the inlet and outlet, while Smoluchowski's slip condition is imposed at fluid-solid boundaries. For calculation of slip velocity, fixed zeta potential ς_f is imposed on the non-conducting channel walls, whereas induced zeta potential ς_i is calculated using equations 4.7 and 4.9. For species transport, a step input condition (as shown in Figure 4.4(a)) is imposed at the channel inlet, using a smoothed Heaviside function, while convective-flux only boundary condition is applied at the channel outlet. At the conducting and non-conducting surfaces, zero flux condition is imposed for the species.

Mixing performance is quantified using the mixing index shown below (details including graphical interpretation are given in section 3.3). It is usually calculated based on the deviations from perfectly mixed state at any particular cross-section (Coleman and Sinton 2005).

$$\eta = \left[1 - \frac{\sqrt{{}^{1}\!/_{N} \sum_{1}^{N} \left(\bar{c} \;\; - \bar{c}^{*} \right)^{2}}}{\sqrt{{}^{1}\!/_{N} \sum_{1}^{N} \left(\bar{c}^{0} - \bar{c}^{*} \right)^{2}}} \right] \tag{4.12}$$

Optimal obstacle shape refers to the shape which provides maximum mixing, i.e. the highest value of η for any given operating conditions. The optimization problem is formulated in terms of NURBS parameters (control point coordinate, weights and knot vector values) so as to minimize the following fitness function (also known as objective function):

$$f(\eta) = (1 - \eta)^{2} \tag{4.13}$$

As the maximum value η can take on is unity, the fitness function is always greater than or equal to zero. Genetic algorithm (GA) is used to arrive at the optimal parameter values. The modeling of ICEO mixer is done using COMSOL 3.3 while the optimization is performed using the GA Toolbox from Matlab. The numerical analysis is repeated with various mesh sizes to ensure mesh-independency of the obtained results. In particular, fine meshes are used near the obstacle surface, channel walls and channel centerline for obtaining accurate results near the interface.

Table 4.1: Simulation Parameters (default values)

Parameter	Value	Description
W	100 μm	Width of the microchannel
L_c	1 mm	Length of microchannel
ς_f	−50 mv	Fixed zeta potential on non-conducting channel walls
D_s	5e−11 m^2/s	Diffusivity of species to be mixed
E	100 V/cm	Applied electric field

4.4 Results and Discussion

The fitness function (equation 4.13) is minimized to obtain the optimal obstacle shape for the given conditions ς_f = –50mV, D = 5*10^{-11} m^2/s and E_0 = 100 V/cm. At these operating conditions, rectangular and semi-circular conducting hurdle yields mixing indices of 0.58 and 0.44, respectively. The optimal shape found to be an approximate right angle triangle, as shown in Figures 4.4(f) and 4.5(f). The mixing index with this optimal shape is 0.98 under the same operating conditions. Various shapes that the GA routine has evaluated at different iterative steps are shown in Figure 4.4 and Figure 4.5 with their corresponding mixing index. The diversity of shapes in Figure 4.5 demonstrates the efficacy of GA to search the parametric space and provide a global solution to the optimization problem. The electric field lines and fluid streamlines are plotted for various obstacle shapes in Figure 4.4 & Figure 4.5 respectively.

To further examine mixing performance, the cross-sectional concentration profile at the exit is plotted for various shapes and is shown in Figure 4.6(a). It is evident that under the same conditions, mixing performance of the optimal shape is much higher compared to the rectangular, semi-circular and triangular shapes. The corresponding surface concentration plots are presented in Figure 4.6(b). Further, the scaled induced zeta potential (for shapes in Figure 4.6(b)) is plotted in Figure 4.7 at externally applied electric field strength of 100 V/cm, where L_{cs} denotes the length of conducting surface. For the given field strength, the maximum induced zeta potential is observed for the rectangular shape.

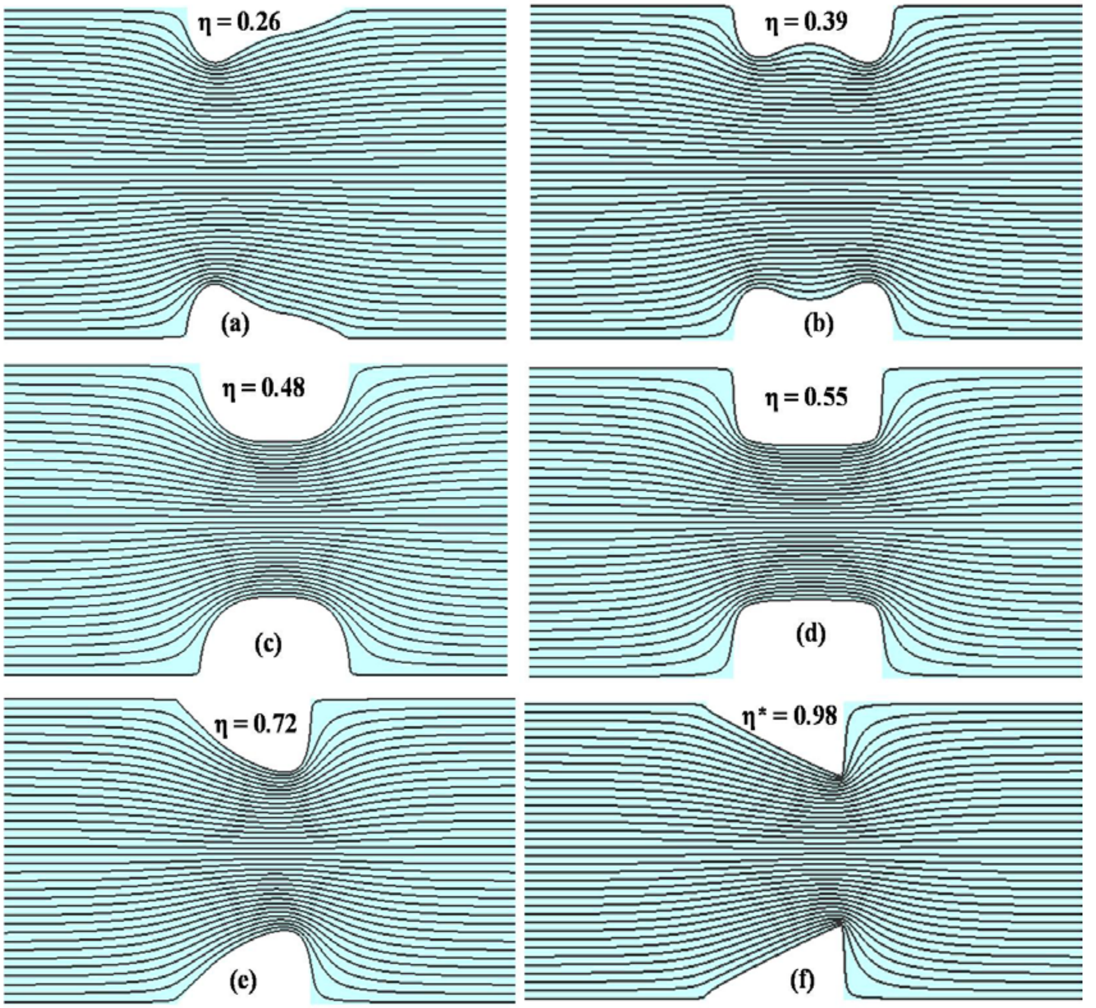

Figure 4.4: Electric field lines near the obstacle surface for various shapes evaluated by GA along with their mixing index.

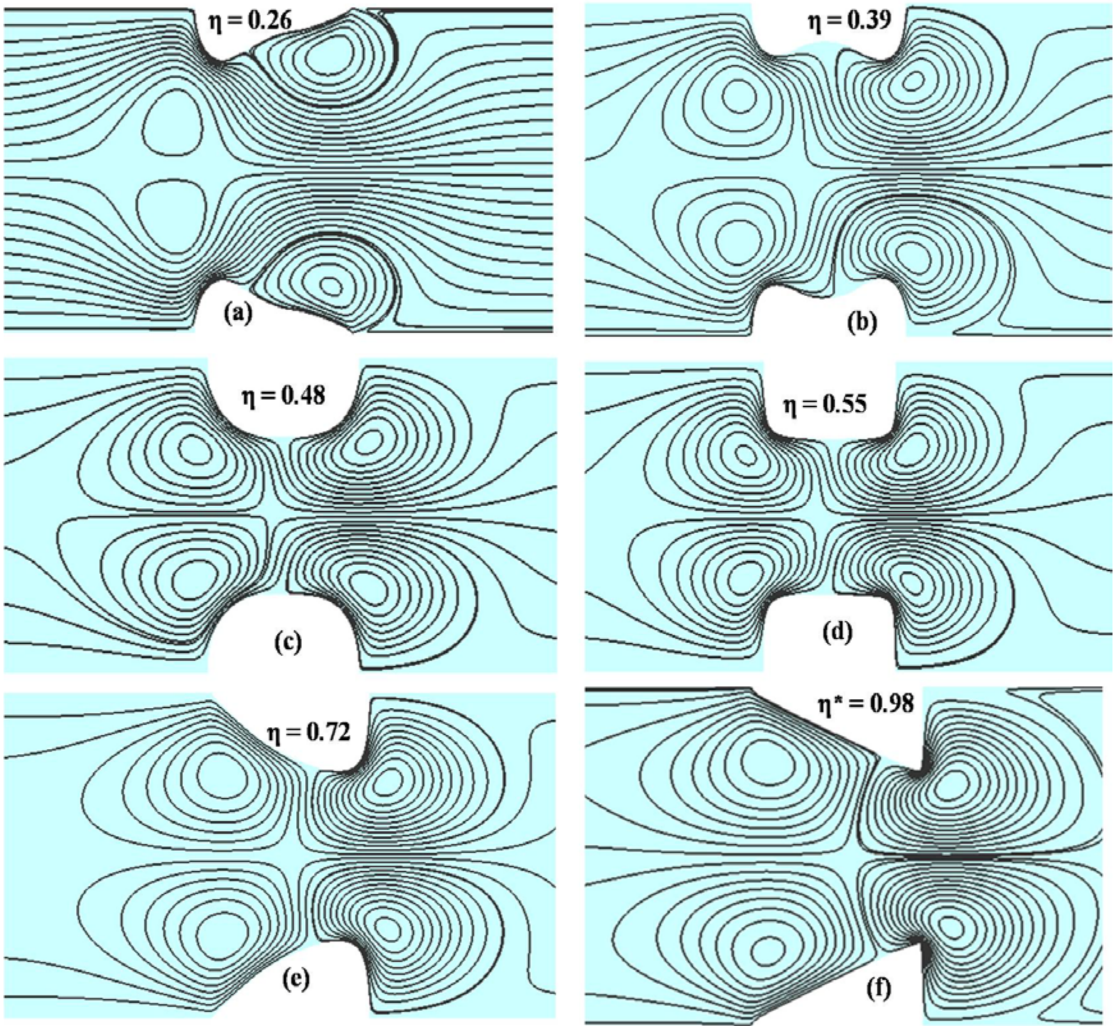

Figure 4.5: Fluid streamlines near the obstacle surface for various shapes evaluated by GA along with their mixing index.

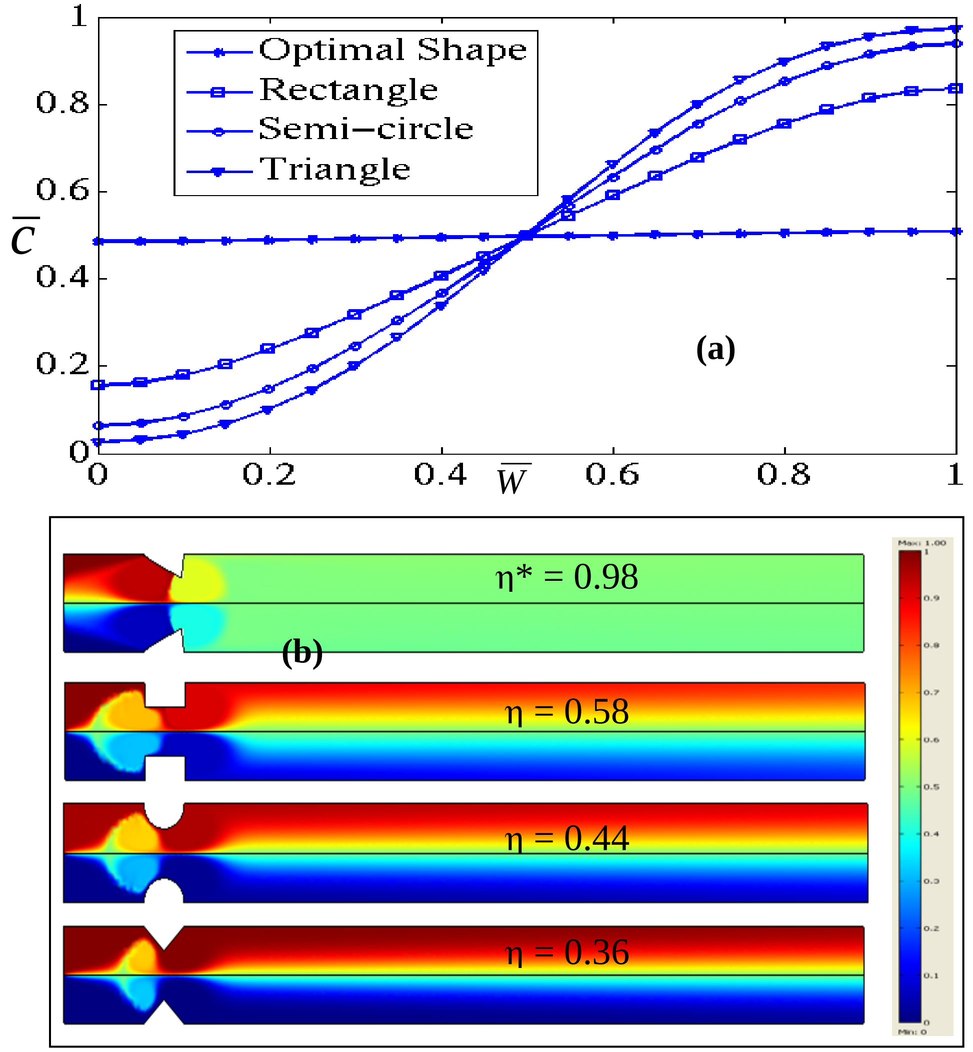

Figure 4.6: (a) Cross-sectional concentration profile at exit; (b) Concentration surface plot for various obstacle shapes.

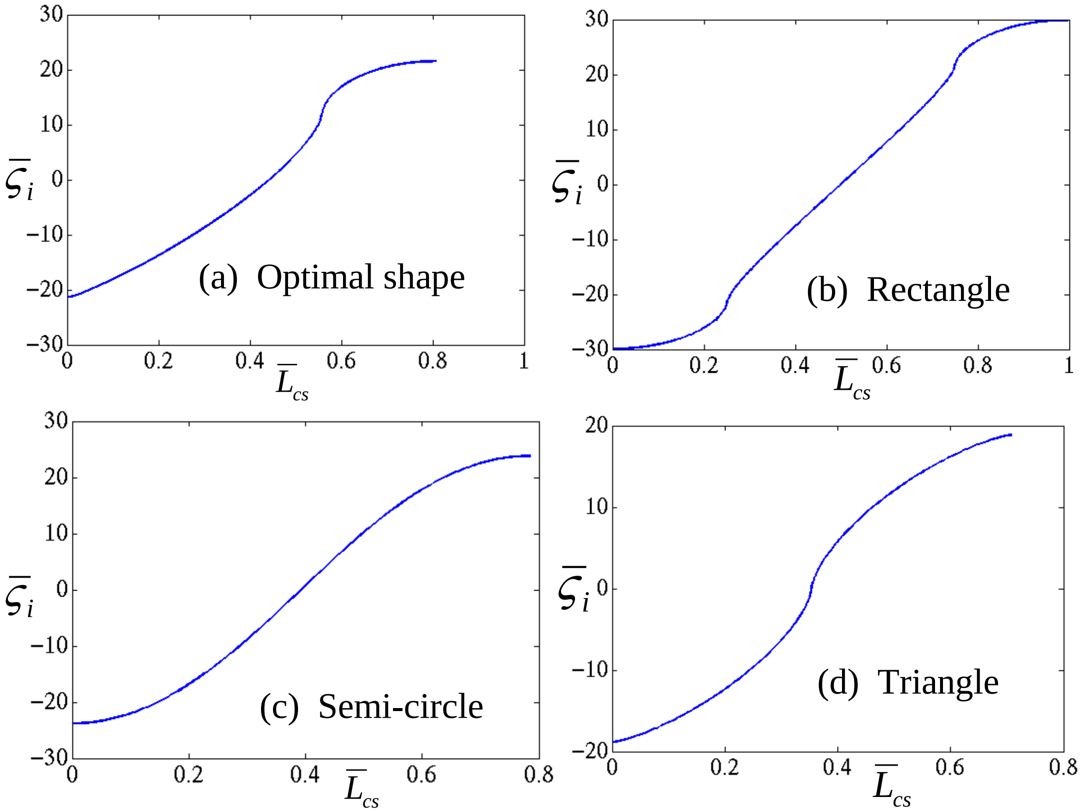

Figure 4.7: Scaled induced zeta potential for different obstacle shapes; note the (a) non-symmetric distribution for near right triangle (optimal) shape and (b), (c) and (d) symmetric distribution for other shapes.

After analyzing one set of operating conditions, the methodology is repeated for various operating conditions and results are presented in Figure 4.8 and Table 4.2. At low electric fields (in the diffusive mixing regime), rectangular shape provides best mixing whereas right triangle shape is the optimal shape for ICEO dominant mixing regime and the evolution of optimal shapes in the intermediate regime is shown in Figure 4.8. The optimality of rectangle shape in the diffusive regime is further validated by the qualitative analysis presented later in the article (Figure 4.12 and related discussion). Further, various conditions are explored in the ICEO dominant regime and the optimal shape is found to be the near right triangle. The mixing at these operating conditions is primarily due to the convective effects originated from ICEO flows and diffusion is not significant as compared to transverse convection as evident from case 3 & 4 in Table 4.2.

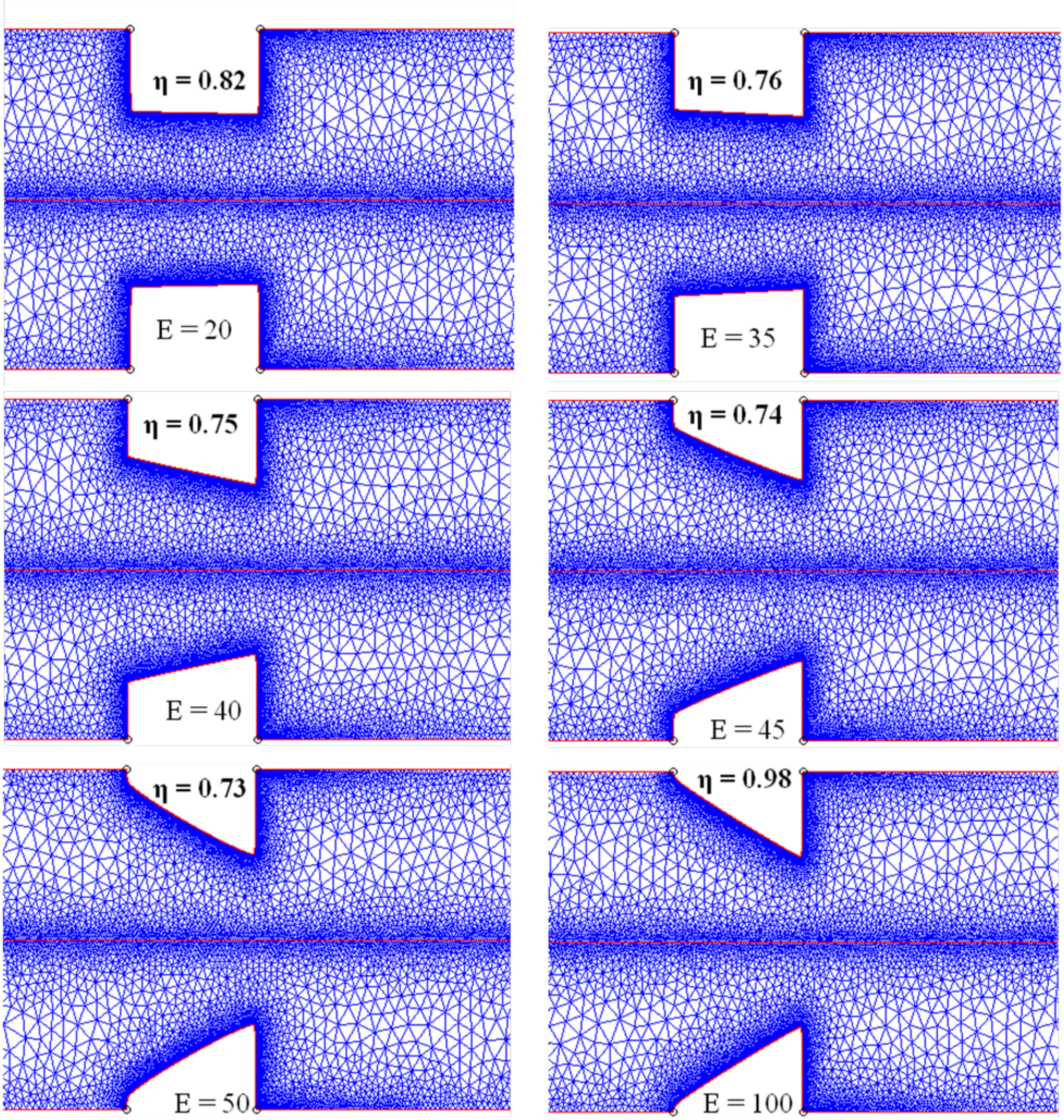

Figure 4.8: Evolution of optimal shapes from rectangular shape at low electric fields (diffusive regime) to right triangle shape at high electric fields (ICEO dominant regime). The optimal shapes in the intermediate regime is shown for electric field between 35-50 V/cm. (Unit for electric field is V/cm).

Table 4.2: Various operating conditions in ICEO dominant Regime

Case	D_t **(m^2/s)**	**E_0 (V/cm)**	ς_f **(mV)**	η	**Optimal Shape**
1.	$5{*}10^{-11}$	100	-50	0.98	Near right triangle
2.	$5{*}10^{-11}$	100	-75	0.67	Near right triangle
3.	$1{*}10^{-11}$	100	-50	0.97	Near right triangle
4.	$1{*}10^{-10}$	100	-50	0.99	Near right triangle
5.	$5{*}10^{-11}$	75	-50	0.84	Near right triangle

Next we analyze the mixing index performance (Figure 4.9) with respect to the applied electric field for ‘near right triangle’, and rectangular shape. For higher electric field strengths, where ICEO flow dominates, the ‘near right triangle’ is yielding superior mixing performance. The mixing performance for optimal shape decreases initially until a critical field E_c (Figure 4.9) is reached, where ICEO flow starts to become dominant as compared to diffusion, and further mixing increases with electric field. On the other hand, rectangular hurdle provides best mixing for low electric fields i.e. in the diffusion dominant regime. The flow rate behavior for both obstacle types is shown in Figure 4.10 where scaled flow rate $\overline{Q}$ is plotted against electric field. The flow rate, for rectangular shape varies linearly with electric field whereas for ‘near right triangle’ shape quadratic dependence on electric field is observed for higher electric fields which point towards the ICEO flow dominance. The tradeoff between mixing and flow rate is apparent from Figure 4.9 and Figure 4.10, which is also reported by Tian et al. (Tian et al. 2005) for heterogeneous microchannels with non-uniform surface potentials.

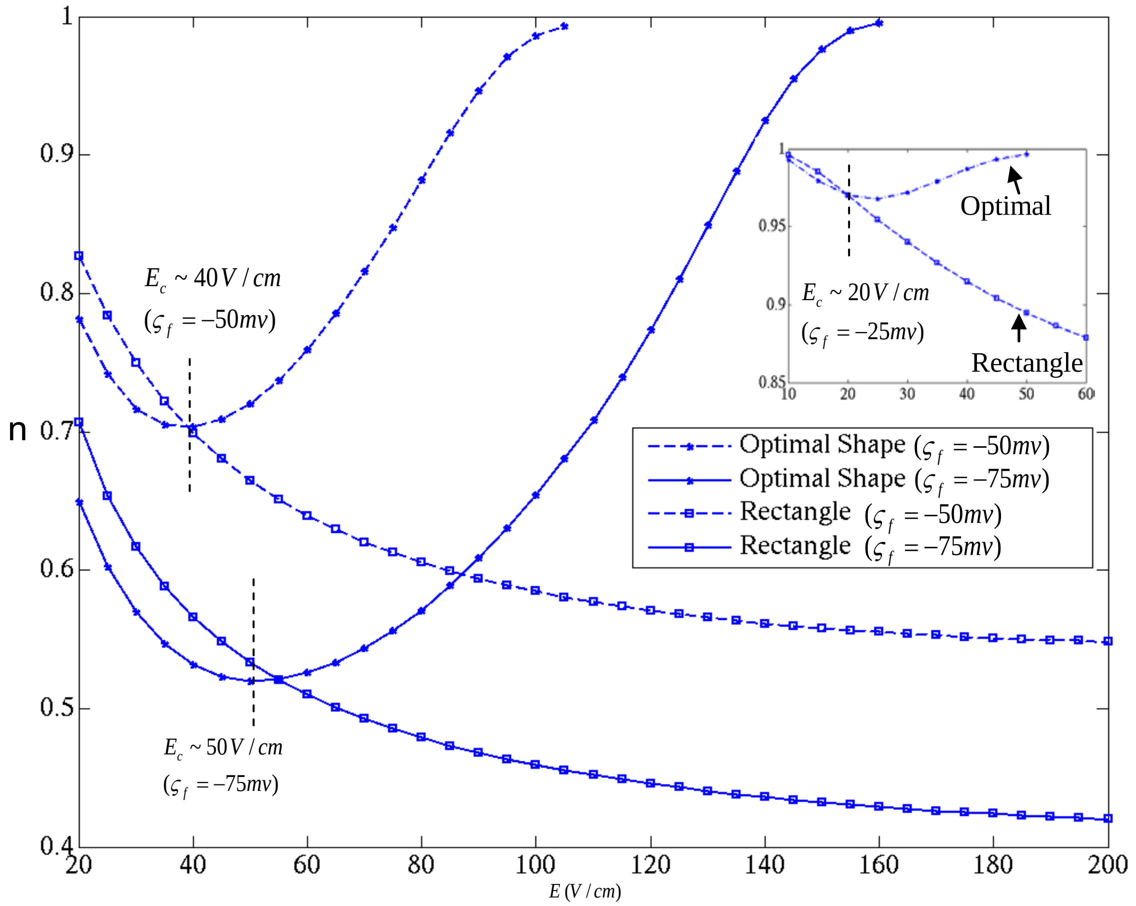

Figure 4.9: Mixing index behavior w.r.t. electric field for ς_f = -50 *mv* and ς_f = -75 *mv*. Mixing index decreases monotonically for rectangular shape whereas mixing performance increases after critical field strength E_c for near right triangle (optimal) shape. (Inset plot data corresponds to ς_f = -25 *mv*).

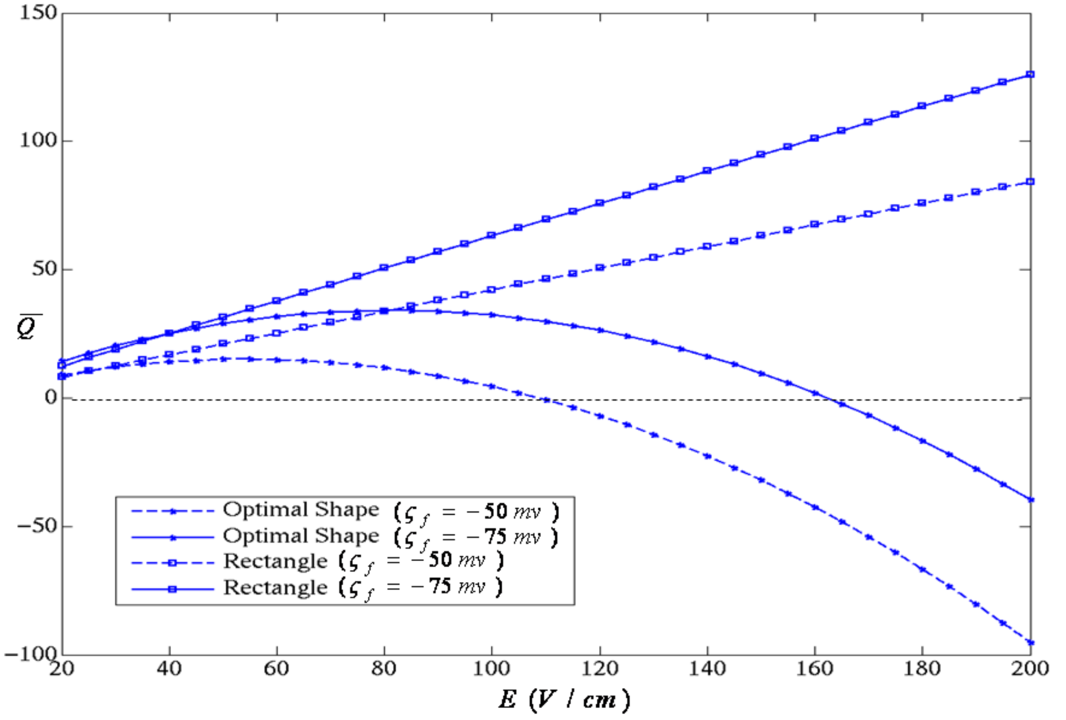

Figure 4.10: Flow rate dependence on electric field for ς_f = -50 *mv* and ς_f = -75 *mv*. Linear dependence is observed for rectangular (symmetric) shape whereas non-linear (quadratic) dependence is observed for optimal (non-symmetric) shape at higher electric fields with change in the flow direction.

The flow behavior for both designs is explained through a schematic (Figure 4.11). The total flow rate Q_T can be written as a sum of flow rates due to FCEO (Q_{FCEO}) and ICEO (Q_{ICEO}). Due to the non-uniform induced zeta potential, the ICEO flow Q_{ICEO} has two components; ICEO flow in the forward direction $(Q_{ICEO})_f$ and ICEO flow in the backward direction $(Q_{ICEO})_b$. For any symmetric conducting obstacle design (rectangular, semi-circular, symmetric triangular), due to symmetric induced zeta potential distribution (Figure 4.7b, 4.7c & 4.7d), $(Q_{ICEO})_f$ component balance out the $(Q_{ICEO})_b$ component and Q_T is solely dependent on Q_{FCEO} (Figure 4.11). However, with non-symmetric designs (near right triangle) the total flow rate Q_T is a function of Q_{FCEO} and Q_{ICEO} (Figure 4.11). For higher electric fields, when ICEO flows are dominant in comparison to FCEO flows, the direction of flow can be reversed using non-symmetric obstacles (Wu and Li 2008a), also seen in Figure 4.10 for 'near right triangle' shape.

We have shown that (Table 4.2 and Figure 4.8) 'near right triangle' shape is the optimal shape for ICEO dominant flow regime. The optimal shape induces transverse convection as well as significantly reduces the overall axial flow rate, due to non-symmetric shape. With significant ICEO generated backflow (overall reduced axial flow), the species retention time increases within the channel, which cause better mixing.

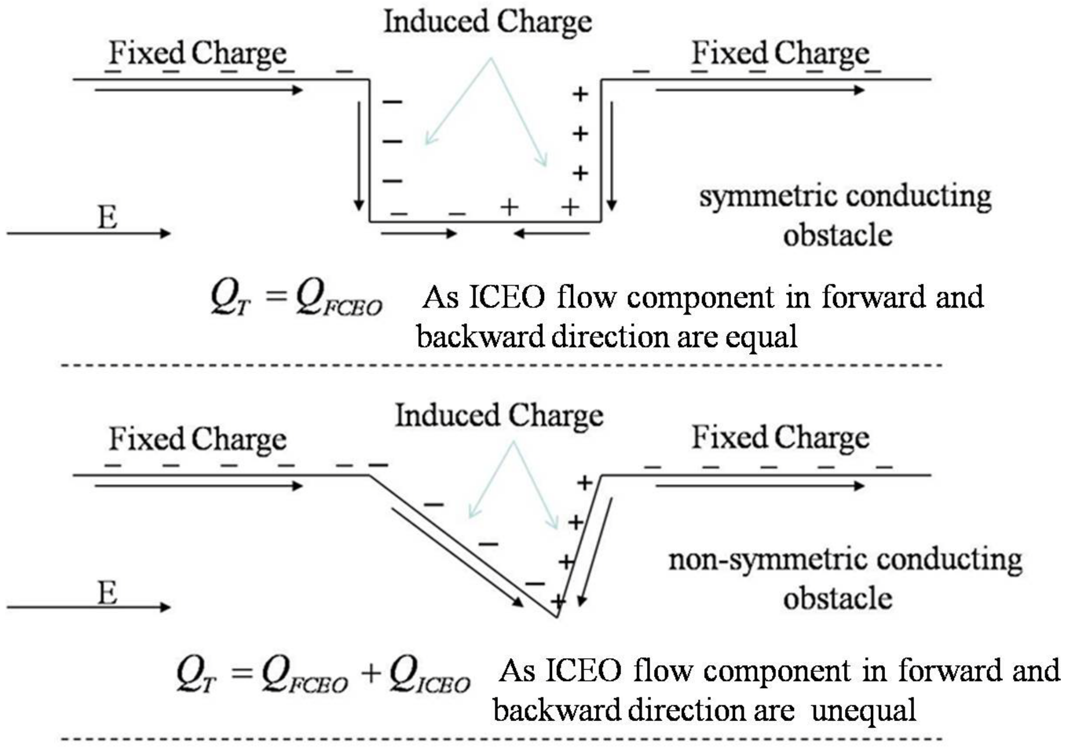

Figure 4.11: Schematic showing dependence of total flow rate on the ICEO flow component.

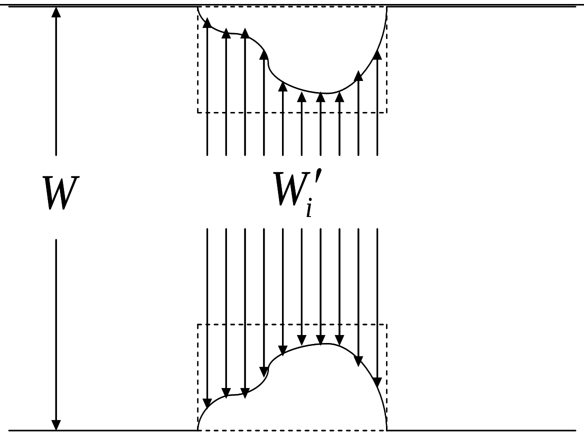

Obstacle within the Bounding Envelope (dashed lines)

W : channel width & W_i': effective channel width

Figure 4.12: Schematic for understanding mixing in diffusion dominant regime.

While, rigorous numerical optimization is employed for obtaining optimal shape for ICEO flow dominant regime, for diffusive mixing regime, optimal shape can be found out using a simple qualitative analysis, presented below. Consider an arbitrary shaped obstacle within the bounding envelope, as shown in Figure 4.12. At low electric fields, mixing is only due to transverse diffusion which in turn is dependent on the effective channel width W_i'. Therefore, the optimal shape, in diffusive mixing regime, is the one which minimizes the effective channel width over the entire obstacle length. It is evident from Figure 4.12 that rectangular obstacle satisfies the above condition and hence it is the optimal shape for diffusion dominant regime, which is observed in Figure 4.8 as well as reported in a previous study (Wu and Li 2008b).

4.5 Summary

NURBS-based shape optimization is performed for maximizing mixing performance of obstacle-based ICEO mixer. It is found that rectangular shaped obstacle provides optimal mixing in the diffusion dominant region i.e. for low electric field strengths. Upon further increase in electric field, ICEO flow become dominant and induces transverse convection within the microchannel. In the ICEO flows dominant regime (at higher electric fields), the optimal shape for conducting obstacle is found to be an approximate right angle triangle. The optimal design not only generates strong local flow vortices but also, due to non-symmetric shape, stimulates maximum backflow compared to any other shape, thereby reducing overall axial flow rate which causes mixing enhancement. The tradeoff between mixing performance and transport rate is observed and the mixing and flow rate curves are analyzed for symmetric and non-symmetric obstacles. The presented methodology can be utilized for optimizing performance in various Lab-on-a-Chip devices.

Chapter 5

Novel Index for Micromixing Characterization and Comparative Analysis[#]

5.1 Introduction

Micro-mixers are often a critical component of miniaturized diagnostic devices, as mixing is essential for fast analysis in many applications (e.g. biochemical analysis (Liu et al. 2008), complex enzyme reaction (Atalay et al. 2009)). Under practically all operating conditions, fluid flow in a micro-device is in the laminar regime. Such low Reynolds number flows are, by nature, very difficult to mix; the predominant mechanism of equalizing concentration differences is therefore often relegated to diffusion. The most basic type of passive micro-mixer is a T- or Y-mixer, where two confluent streams intermix due to transverse diffusion. Various modifications have been reported in the literature for enhancing mixing performance of such mixers. Some of these approaches include: sequential

---

[#] A version of this chapter has been published. [M. Jain and K. Nandakumar, Biomicrofluidics, 4, 031101 (2010); M. Jain**,** A. Yeung and K. Nandakumar, Micromachines, 1, 36-47 (2010)] injection of samples (Coleman and Sinton 2005; Coleman et al. 2006), patterned heterogeneous surface charge along the channel bottom (Biddiss et al. 2004), grooved patterns on the channel base (Stroock et al. 2002), instability mixing due to electrical conductivity gradients (Oddy et al. 2001; Lin et al. 2004), and the use of embedded conducting (Wu and Li 2008a; Wu and Li 2008b; Jain et al. 2009a; Jain et al. 2009b) or non-conducting (Chang and Yang 2004; Chen and Cho 2007) obstacles within the microchannel. Typically, such designs provide effective mixing either by reducing the diffusion length or by increasing the interfacial contact area for mass transfer within the microchannel. The mixing performance is further augmented by the reduced flow rate (Wu and Li 2008a; Wu and Li 2008b; Jain et al. 2009b; Chang and Yang 2004; Chen and Cho 2007) of such designs, which increases the species residence time within the micro-device. While an increased interfacial contact area or shortened diffusion length is favored in any improved design, mixing enhancement due to residence time effect is often not desirable. Therefore, it is important to normalize the effect of residence time when comparing different micro-mixer designs. Although many studies have noted the reduced flow rates for improved mixer designs (Tian et al. 2005; Chang and Yang 2007), the residence time effect has not been taken into consideration in micro-mixing performance evaluation. Most of the reported designs are evaluated against the T-mixer in terms of the deviation from perfectly mixed state and mixing length (device length required to achieve perfect mixing).

In this chapter, we propose a novel index, based on residence time, for micro-mixing characterization and comparative analysis. The proposed ‘comparative mixing index’ (CMI) evaluates mixing performance more appropriately by normalizing the effect of residence time among different designs. For any given mixer, CMI identifies the non-diffusive mixing enhancement w.r.t to the T-mixer. The performance of several mixing strategies are evaluated based on the CMI; these are mixer designs that incorporate (a) physical constrictions, (b) induced charge electro-osmotic (ICEO) effects, and (c) heterogeneously charged walls. The present analysis clearly identifies conditions under which a given mixer design is superior to a T-mixer. The proposed index is defined in the theory section followed by its graphical interpretation. Various case studies are presented to demonstrate the usefulness of proposed index in results section.

5.2 Comparative Mixing Index (CMI)

In a T- or Y-mixer, two different solutions flow adjacently in the same direction and mixing is primarily due to transverse diffusion. The inlet condition for T-mixer can be represented by step input as shown in Figure 5.1(a). Mixing performance, for such parallel flow type mixers, is quantified using the following mixing index (Coleman and Sinton 2005; Wu and Li 2008a; Jain et al. 2009a; Chen and Cho 2007; Erickson and Li 2002), which evaluates the deviation from perfectly mixed state as shown in Figure 5.1:

$$\eta = \left[1 - \frac{\sqrt{\frac{1}{N}\sum_{1}^{N}\left(\bar{c}_s - \bar{c}_s^*\right)^2}}{\sqrt{\frac{1}{N}\sum_{1}^{N}\left(\bar{c}_s^0 - \bar{c}_s^*\right)^2}} \right] \tag{5.1}$$

In the above equation, N is the number of points in the cross-section used for estimation of the mixing index. The variable $\bar{c}_s$ represents the scaled concentration value at that point, while $\bar{c}_s^0$ and $\bar{c}_s^*$ are the scaled concentration at each point if the solutions are unmixed and the concentration with perfect mixing (i.e. 0.5), respectively. Based on the mixing index definition (equation 5.1), the theoretical limits for η is between zero and one. The cross-sectional concentration profiles corresponding to η values of zero and one are plotted in Figure 5.1. Typically, the above index is evaluated at the channel exit and it has been extensively employed for comparative analysis between various micro-mixer designs. As stated earlier, the mixing index η estimate the deviation from perfectly mixed state and doesn't account for reduced flow rates or variation in residence time τ among different designs.

When comparing two different mixer designs, the residence time τ should be considered as it directly relates to the time available for diffusive mixing. Thus mixing performance evaluation based on η alone is insufficient and could lead to a false sense of improvement as shown in results section later.

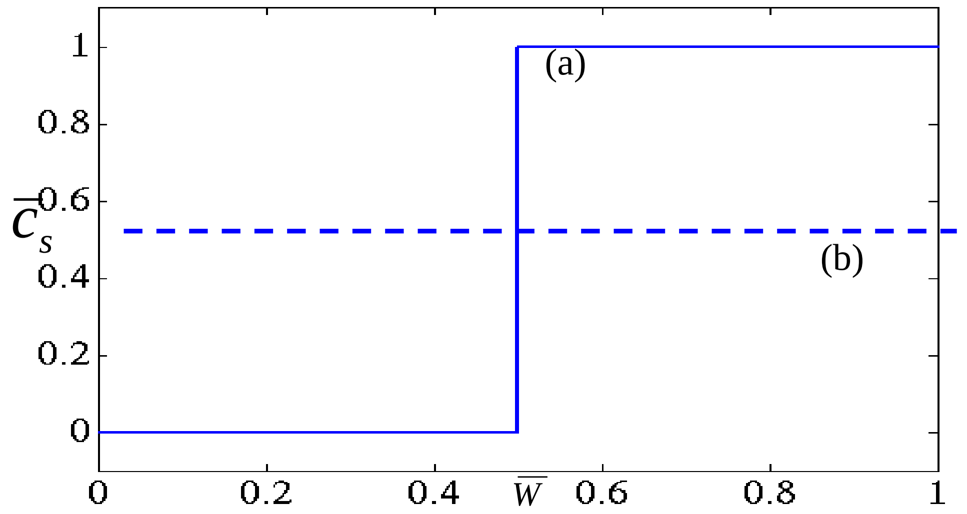

Figure 5.1: Cross-sectional concentration profiles for η values (a) $\eta = 0$ corresponds to perfectly unmixed state (inlet condition for T-mixer); (b) $\eta = 1$ corresponds to perfectly mixed state.

To accommodate the residence time in comparative analysis, a comparative mixing index (CMI) is proposed below:

$$\alpha_{A,B} = \frac{(\eta\ )_A\big|_{(L_c,\tau)}}{(\eta\ )_B\big|_{(L_c,\tau)}} \tag{5.2}$$

In the above equation, $\alpha_{A,B}$ is the comparative mixing index, which essentially evaluates the η values for design *A* & design *B* for same residence time. If any design *A* is evaluated against T-mixer, then the above index can be written as:

$$\alpha_{A,T-mixer} = \frac{(\eta\ )_A\big|_{(L_c,\tau)}}{(\eta\ )_{T-mixer}\big|_{(L_c,\tau)}} \tag{5.3}$$

Based on the mixing index definition (equation 5.3), the theoretical limits for $\alpha_{A,T-mixer}$ is between one and infinity. For given design *A*, values of CMI close to unity indicates its equivalency to T-mixer whereas higher values suggest better mixing performance with reference to T-mixer. Also, the term, $\alpha_{A,T-mixer} - 1$, identifies the non-diffusive mixing component for design *A*. Further any two arbitrary designs can be compared by benchmarking their mixing performance w.r.t to T-mixer using equation 5.3.

It is evident from equations 5.3 that proposed index would be useful in analyzing micro-mixing designs where residence time effects are significant. In particular, the proposed index would be beneficial for continuous, parallel flow type micro-mixers where static mixing element (conducting/ non-conducting obstacles, heterogeneous charged walls) also acts as a resistance to fluid flow. It is not applicable for batch-mode micro-mixers such as AC electro-osmosis (ACEO) based micro-mixers (Lastochkin et al. 2004) where enhanced micro-mixing is demonstrated in a reservoir (Wang et al. 2006) and in a micro-cavity (Feng et al. 2007). Further, if improved micro-mixing is achieved via increase in interfacial contact area (sequential injection strategy (Coleman and Sinton 2005), pulsed flow techniques (Liu et al. 2008; Glasgow and Aubry 2003), using periodic EOF (Lim et al. 2010)) without significantly affecting residence time or resistance to fluid flow then CMI and η would provide similar results.

For better understanding, the graphical illustration for the proposed index CMI is presented in Figure 5.2. Consider Figure 5.2, where η and τ are plotted w.r.t to electric field for T-mixer and any arbitrary design A. It is observed, especially in the case of electrokinetic micro-mixers (Coleman and Sinton 2005; Wu and Li 2008a; Jain et al. 2009a; Chen and Cho 2007; Erickson and Li 2002), that higher η values are obtained at the expense of reduced flow rate i.e. higher residence time (Figure 5.2).

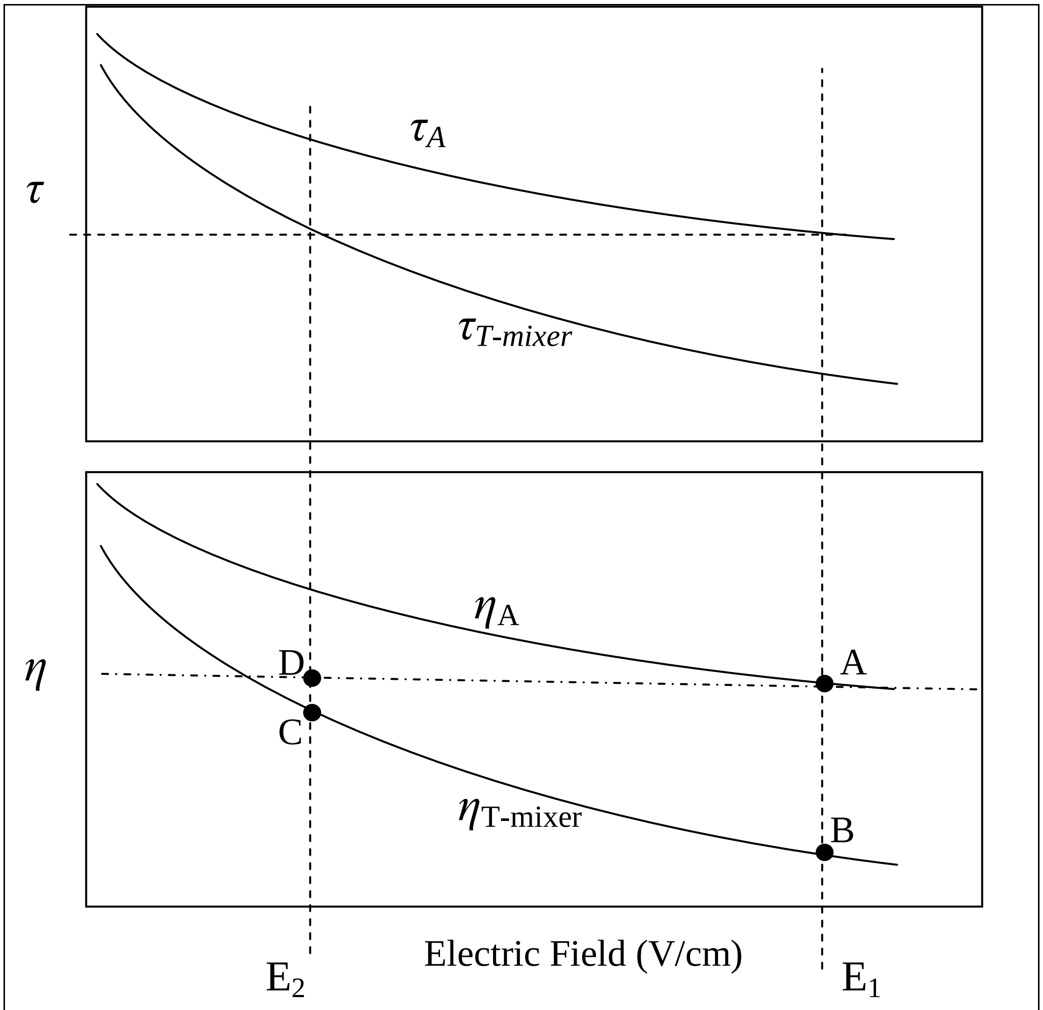

Figure 5.2: Graphical Interpretation for the proposed index. The proposed index considers residence time and hence identifies the true improvement over T-mixer.

Most of the reported studies compare mixing performance at a particular applied field without considering the residence time. Therefore, for a given field E_1, only points A and B are considered (Figure 5.2) and the difference is identified as mixing improvement over T-mixer. However, T-mixer requires a smaller applied field E_2 ($E_2 < E_1$) for same residence time as of design A. Hence, the proposed index considers points C and D (Figure 5.2) for comparative analysis for design *A* and T-mixer. It is evident that from Figure 5.2 that comparison based on η is inadequate and may mislead in terms of improvement in mixing performance over T-mixer (also demonstrated in results section).

5.3 Mathematical Model

The electrokinetic micro-mixers can be modeled using either full PNP model or using simplified Smoluchowski's slip velocity approach as mentioned in section 2.4. In this chapter, the analysis is carried out using Smoluchowski's slip velocity model (Lyklema 1995) for thin electric double layer (EDL) as our primary aim is to analyze micro-mixing performance using CMI. It is worth mentioning that several previous studies have utilized slip-velocity approach for modeling micro-mixing techniques (Biddiss et al. 2004; Wu and Li 2008a; Wu and Li 2008b; Jain et al. 2009a; Erickson and Li 2002).

The non-conducting channel walls are negatively charged with fixed zeta potential ς_f. The solution is assumed to be an incompressible, Newtonian fluid with fixed dielectric constant ε_r, viscosity μ, and density ρ. To describe the mathematical model, we introduce the following reference quantities and dimensionless variables:

$$L_{\mathrm{ref}} = W, \quad \psi_{\mathrm{ref}} = \frac{K_b T}{ze}, \quad c_{\mathrm{ref}} = c_{0,} \quad E_{\mathrm{ref}} = \frac{\psi_{\mathrm{ref}}}{L_{\mathrm{ref}}}, \quad u_{\mathrm{ref}} = \frac{\varepsilon_0 \varepsilon_r \psi_{\mathrm{ref}}}{\mu} E_{\mathrm{ref}} \text{ , and}$$

$$\bar{x} = \frac{x}{L_{ref}}, \quad \bar{y} = \frac{y}{L_{ref}}, \quad \bar{\psi} = \frac{\psi}{\psi_{ref}}, \quad \bar{u} = \frac{u}{u_{ref}}, \bar{E} = \frac{E}{E_{ref}}, \quad \bar{p} = \frac{p}{\rho u_{ref}^2}, \quad \bar{t} = \frac{t\,u_{ref}}{L_{ref}}$$

Here W is the channel width, $K_b, T, c_0, \varepsilon_0$ represent Boltzmann constant, absolute temperature, species concentration and permittivity of free space. Other notations/symbols and simulation parameters used in this study are listed in Table 5.1.

With the assumption of thin electric double layer (EDL) and uniform bulk conductivity, the electric potential distribution at steady state can be solved using the Laplace equation. In non-dimensional form, the Laplace equation is

$$\bar{\nabla}^2 \bar{\psi} = 0 \tag{5.4}$$

At the channel inlet, a constant potential V_0 relative to the outlet potential is applied, giving rise to a steady electric field E in the x direction and at the channel as well as the obstacle surface, normal component of electric field is specified as zero i.e. $n.\nabla\psi = 0$.

Table 5.1: Simulation Parameters (default values).

Parameter	**Value**	**Description**
W	100 μm	Width of the microchannel
L_c	2 mm	Length of microchannel
ς_f	-50 mv	Fixed zeta potential on channel walls
D_s	5e$-$11 m^2/s	Diffusivity of species to be mixed
a	25 μm	Radius of non-conducting obstacle (Figure 5.3a)
p	100 μm	Heterogeneous charged surface patch length (Figure 5.3c)

The flow field in the computational domain is governed by the continuity and Navier-Stokes equations. These equations, in their dimensionless forms, are

$$Re(\overline{u} \cdot \overline{\nabla}\overline{u}) = -\overline{\nabla}\overline{p} + \overline{\nabla}^2\overline{u} \tag{5.5a}$$

$$\overline{\nabla} \cdot \overline{u} = 0 \tag{5.5b}$$

In the above equations, *Re* is the Reynolds number (ratio of inertial to viscous forces). The slip velocity boundary condition (Helmholtz-Smoluchowski's equation) is used to account for the electrical body force term as shown below:

$$\overline{u} = \overline{\varsigma}\,\overline{E} \quad \text{where} \left\{ \begin{array}{l} \overline{\varsigma} = \overline{\varsigma}_f \text{ at non-conducting surface} \\ \overline{\varsigma} = \overline{\varsigma}_i \text{ at conducting surface} \end{array} \right\} \tag{5.6}$$

In the above equation, ς_f is the fixed zeta potential on the non-conducting surface, whereas ς_i is the induced zeta potential (for ICEO mixer) on the conducting surface. The induced zeta potential is estimated using the Correction method (Wu and Li 2008a). The Smoluchowski's slip condition (equation 5.6) is imposed at fluid-solid boundaries, while zero pressure conditions are imposed at the inlet and outlet.

The steady transport of species is governed by the convection-diffusion equation and can be written in terms of Peclet number Pe as:

$$Pe(\overline{u} \cdot \overline{\nabla}\overline{c}) = \overline{\nabla}^2\overline{c} \tag{5.7}$$

For species transport, a constant concentration condition is imposed at the channel inlets (i.e. scaled concentration of 1 and 0 at inlet 1 and inlet 2 respectively). The aforementioned condition is implemented at the inlet boundary using a smoothed Heaviside function (with continuous second derivative). At the conducting surfaces and non-conducting channel walls, zero flux condition is imposed for the species, while convective-flux only boundary condition is applied at the channel outlet. The above model is solved using the direct (UMFPACK) solver available within the commercial finite element method package, COMSOL 3.4. The numerical analysis is carried out with sufficiently fine mesh and reported numerical results are mesh-independent.

5.4 Results and Discussion

The proposed index is used for characterization of the following mixer types: (1) physical constriction or obstacle based micro-mixer, (2) conducting obstacle or induced charge electro-osmotic (ICEO) mixer, and (3) heterogeneously charged walls mixer. The design schematic (not drawn to scale) for the above mentioned micro-mixer types are shown in Figure 5.3.

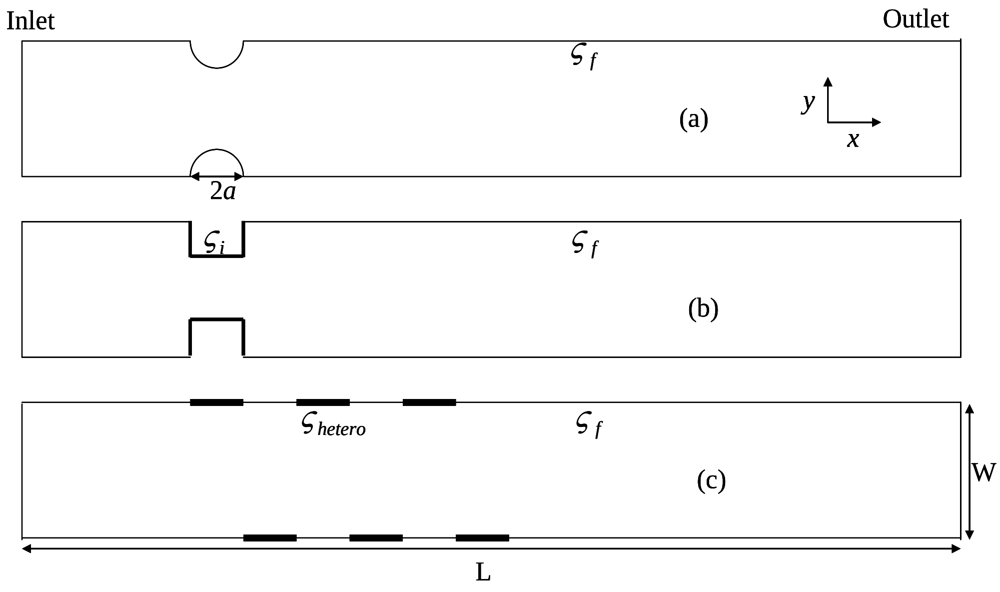

Figure 5.3: Micro-mixer design schematic for (a) Physical constriction mixer (characterized by fixed zeta potential ς_f); (b) ICEO mixer (characterized by induced zeta potential ς_i on conducting obstacle surface) and (c) Heterogeneously charged wall mixer (staggered arrangement, characterized by heterogeneous zeta potential ς_{hetero} on heterogeneous patch).

(a) Physical constriction / obstacle based mixer

Mixing performance can be enhanced by introducing non-conducting obstacles embedded on the micro-channel wall (Chang and Yang 2004; Chen and Cho 2007). It is shown that such obstacles/physical constrictions can reduce the diffusion length around the obstacle, which in turn enhances mixing. However, at the same time, these obstacles offer hydraulic resistance to flow and reduce the overall flow rate.

In this study, a micro-mixer with a pair of non-conducting semi-cylindrical obstacle (radius a) is analyzed (Figure 5.3a). The effect of obstacle radius on mixing performance is shown in Figure 5.4. The estimated CMI values are close to unity (see Figure 5.4), which indicates that physical constriction-type mixers do not offer any significant mixing benefits as compared to the T-mixer. The CMI analysis suggests that any increase in diffusive flux (due to obstacle) is offset by the additional flow resistance caused by the obstacle (also shown below using simple analysis). The mixing performance does not increase appreciably with the number of obstacle pairs, as shown in Figure 5.5. However, mixing performance can be improved with heterogeneously charged obstacles (Chang and Yang 2004; Chen and Cho 2007), where micro-vortices can be generated in the microchannel due to surface heterogeneity.

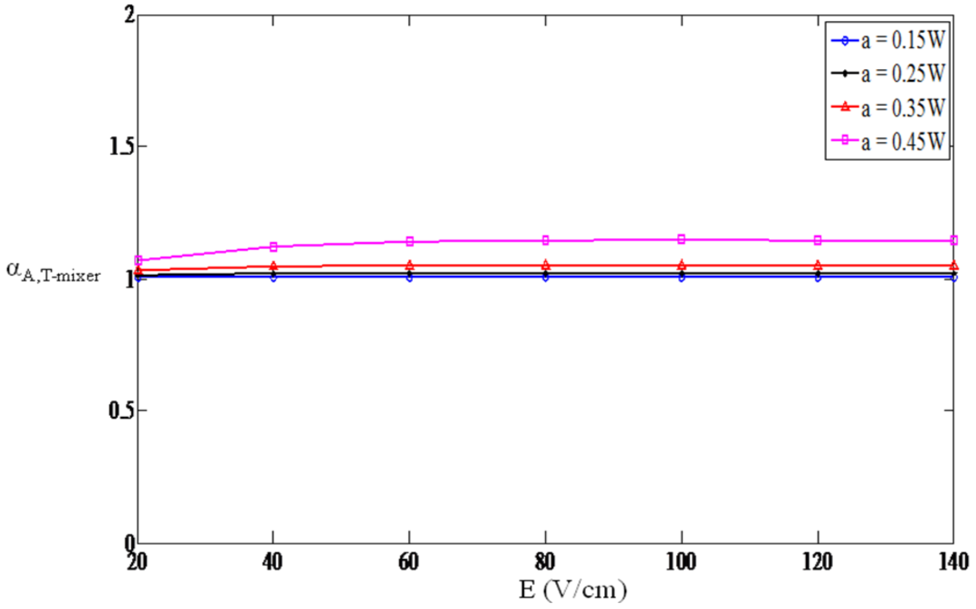

Figure 5.4: Comparative mixing index (CMI) is plotted for physical constriction mixer with variation in obstacle radius. CMI values suggest that mixing performance increases with obstacle radius though not significantly as compared to T-mixer.

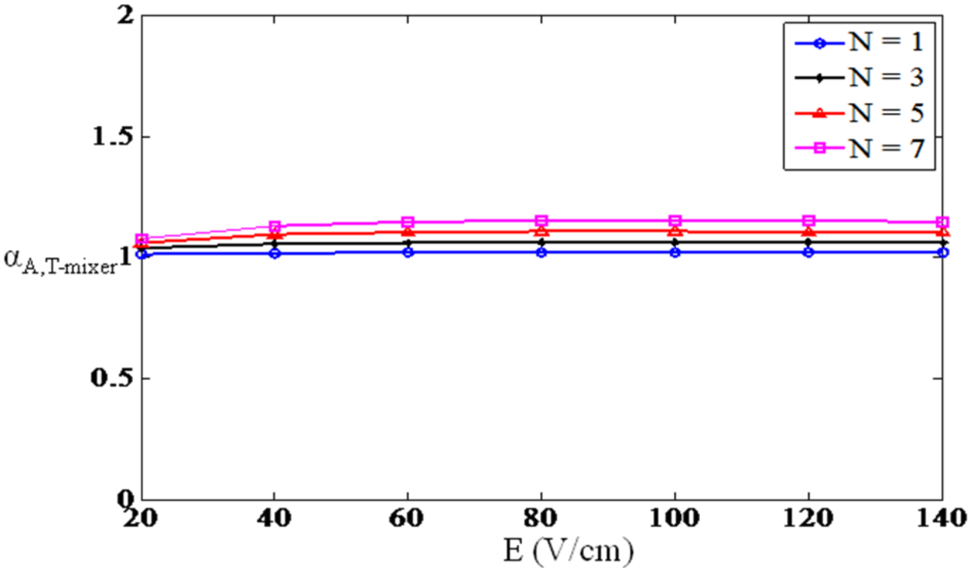

Figure 5.5: CMI plot for physical constriction mixer for different number of obstacle pairs with a = 0.25W. The maximum CMI value is 1.15 (for N = 7).

In a parallel flow type micro-mixer, if there are no flow circulations, η is dependent on transverse diffusive flux $(j_D)_y$ integrated over channel length L_c. Therefore, η and hydraulic resistance R_h for T-mixer can be written in terms of channel width w as follows:

$$\begin{aligned} \eta_{T-mixer} &\propto \int_0^{L_c} \left(j_d\right)_y \sim D\frac{\Delta c}{w}L_c \\ (R_h)_{T-mixer} &= \frac{\mu}{\varepsilon\varsigma}\frac{L_c}{w} \end{aligned} \tag{5.8}$$

For obstacle/ physical constriction micro-mixer, the variation in channel width can be accounted as follows:

$$\begin{aligned} \eta_{Obs-mixer} &\propto \int_0^{L_c} \left(j_d\right)_y \sim D\Delta c\int_0^{L_c} \frac{dx}{w(x)} \\ (R_h)_{Obs-mixer} &= \frac{\mu}{\varepsilon\varsigma}\int_0^{L_c} \frac{dx}{w(x)} \end{aligned} \tag{5.9}$$

Using equation 5.8 & 5.9, it can be shown that variation in width (obstacle) affects mixing performance and hydraulic resistance in same manner i.e.

$$\frac{\Delta\eta}{\eta_{T-mixer}} = \frac{\eta_{Obs-mixer} - \eta_{T-mixer}}{\eta_{T-mixer}} = \frac{(R_h)_{Obs-mixer} - (R_h)_{T-mixer}}{(R_h)_{T-mixer}} = \frac{\Delta(R_h)}{(R_h)_{T-mixer}} \tag{5.10}$$

Using the proposed CMI, it is shown that physical constriction type mixer doesn’t offer any significant mixing benefits as compared to T-mixer. Although the analysis is carried out for single obstacle, the results are equally valid for multiple obstacle case (Chang and Yang 2004; Chen and Cho 2007) provided that there are no flow circulations in the vicinity of obstacle.

(b) Induced charge electro-osmotic (ICEO)/ conducting obstacle mixer

Conducting obstacle-based mixers are also known as induced charge electro-osmotic (ICEO) mixers, as charges are induced on polarizable and electrically conducting surfaces by an externally applied electric field (Bazant and Squires 2004). Due to the induced charges, flow circulations are generated near the obstacle which enhances micro-mixing (Wu and Li 2008a; Wu and Li 2008b; Jain et al. 2009a; Jain et al. 2009b). The design schematic for ICEO mixer with rectangular conducting obstacle is shown in Figure 5.3b. The most critical parameter for ICEO mixers is the induced charge/induced zeta potential ς_i. The magnitude of ς_i is dependent on the applied electric field, as well as the obstacle size and shape. In this study, steady state induced zeta potential is estimated using the Correction method (Wu and Li 2008a).

In Figure 5.6a, the CMI is plotted for semi-cylindrical conducting obstacles with $a = 0.2\,W$ and $a = 0.4\,W$. The magnitude of the induced potential increases with the obstacle radius which in turn increases the ICEO transverse flow in the microchannel, resulting in better mixing as compared to T-mixer (Figure 5.6a). The corresponding η values are plotted for an ICEO mixer ($a = 0.4\,W$) and a T-mixer in Figure 5.6b. It is evident from the CMI and η plots (Figure 5.6) that ICEO mixers provide better mixing compared to T-mixers. The primary reason for enhanced mixing is the generation of micro-vortices due to induced charge electrokinetic flow. Moreover, the induced transverse ICEO velocity scales quadratically with respect to electric field resulting in superior mixing performance at higher fields.

Next, we analyze the effect of obstacle shape on mixing performance using CMI. Previous study (Jain et al. 2009b) has identified 'right triangle' as an optimal shape for maximizing mixing performance in ICEO mixers. The rectangular shape and the optimal shape (right triangle) are examined for a range of electric field values. As reported earlier (Jain et al. 2009b), the η plot (Figure 5.7a) suggests that the right-triangle shape obstacle provides better mixing than its rectangular counterpart. The reason for superior performance of the optimal shape is the increased species residence time. The optimal shape, due to its non-symmetric shape, reduces the overall flow rate by inducing ICEO back flow (Jain et al. 2009b). However as CMI normalizes the effect of residence time, the CMI values are higher for rectangular shape as demonstrated in Figure 5.7b. For the right-triangle shape, the CMI value approaches unity in the high field limit, resulting in equivalent mixing performance as for a T-mixer. Based on the η and CMI plots, the optimal range of operation for right-triangle shaped mixers appears to be between $E = 140$ and 180 V/cm.

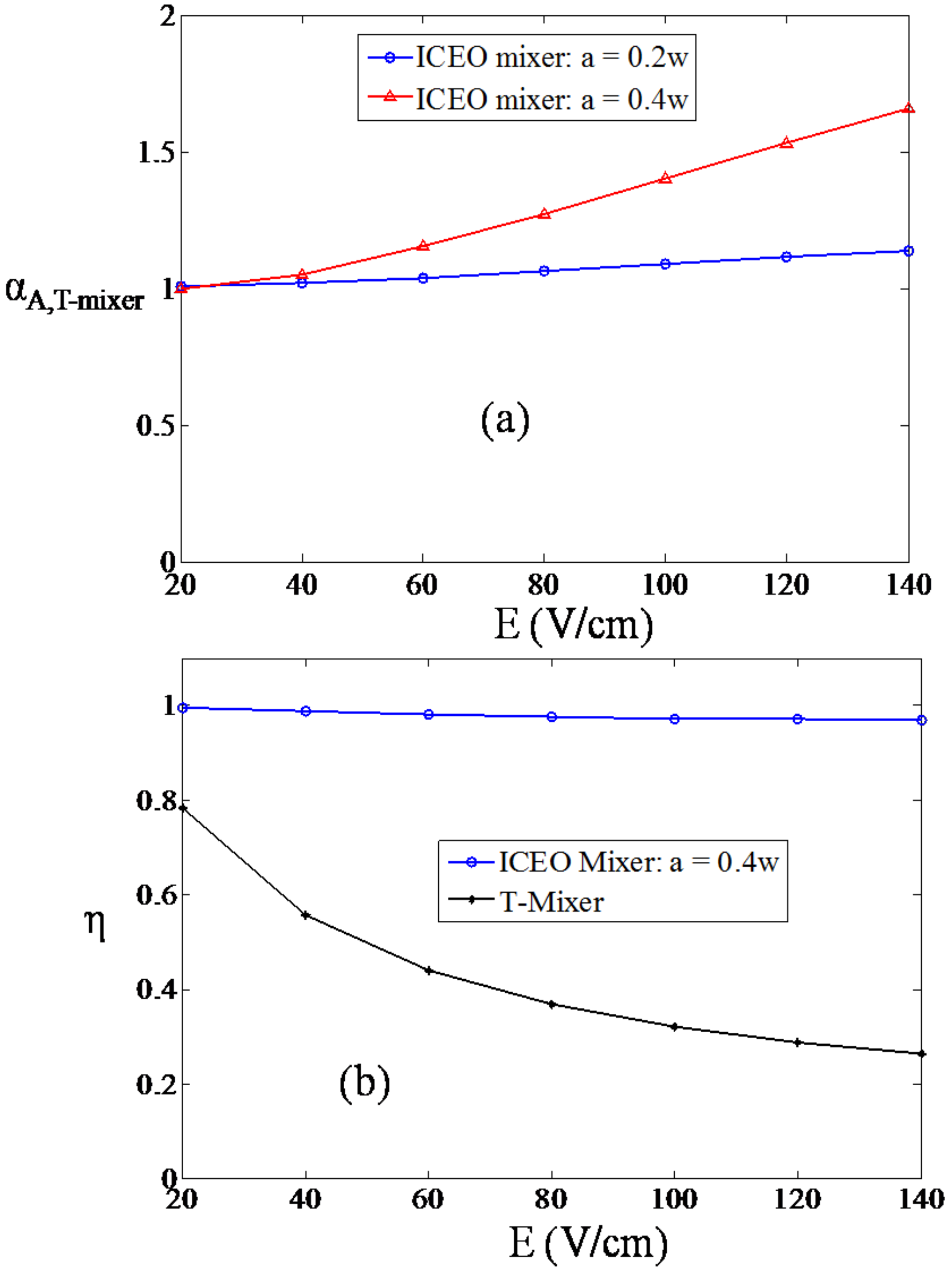

Figure 5.6: (a) CMI plot for ICEO mixer; mixing performance increases with conducting obstacle radius. (b) ICEO mixer and T-mixer is compared in terms of η values. Both CMI and η plots suggest that ICEO mixer provided superior mixing at higher electric fields as compared to T-mixer.

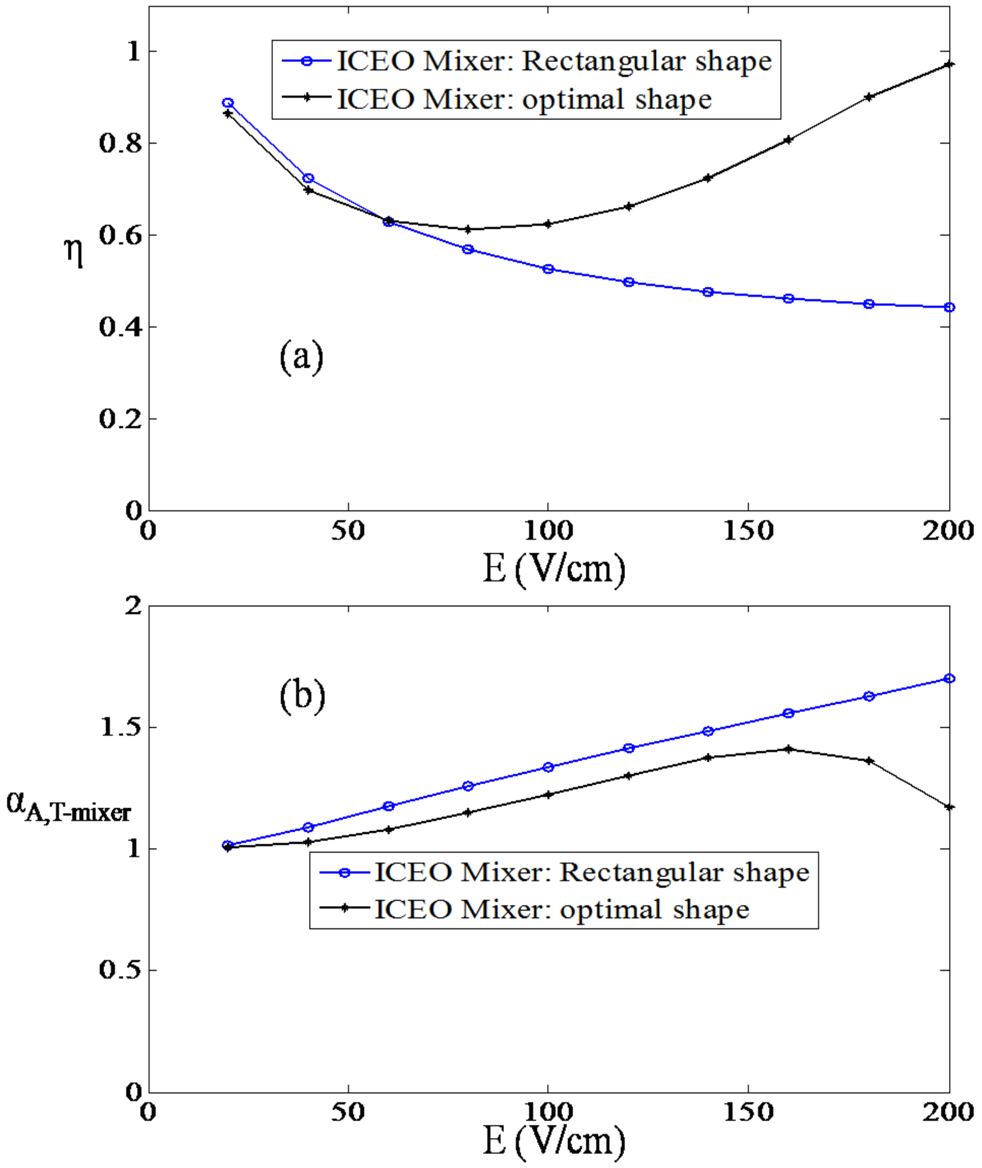

Figure 5.7: Rectangular shape and optimal (right-triangle) shape is examined using CMI and η plots for ICEO mixer. Although η values suggest that right-triangle shape provides superior mixing (a), CMI values are higher for rectangular shape (b). Upon further increase in electric field, CMI values for optimal shape will approach unity.

(c) Heterogeneous charged walls mixer

Heterogeneously charged patches can be used to generate flow circulations within a micro-channel; this in turn will enhance micro-mixing (Tian et al. 2005; Erickson and Li 2002). The patches are arranged in a staggered manner (Figure 5.3c), with opposing patches on the two walls having an offset that is equal to the patch length. (Here, N_p = number of patches, ς_{hetero} = zeta potential on the patch surfaces, L_p = length of each patch, which equals the channel width W). The mixing performance is examined for different ratios of zeta potential ($R = \varsigma_{hetero} / \varsigma_f$). The flow profile and species concentration surface plot are shown for different R values in Figure 5.8. It can be seen that the size of the vortices increases with negative values of R.

The CMI for various R values are plotted in Figure 5.9. In Figure 5.10a and 5.10b, η and CMI values are plotted for N_p = 3 and 6. Another interesting observation can be made with data points (Figure 5.10) corresponding to the electric field E = 40 V/cm. At this field strength, the η values suggest that the heterogeneously charged mixer (η = 0.96) is almost twice as good as the T-mixer (η = 0.55). However, for the same field strength, the CMI value is close to 1.1, which suggests similar mixing performance for the two designs. This implies that flow circulations, at this electric field strength, does not cause considerable mixing (by reducing diffusion length) but rather reduces the flow rate significantly (by acting as flow resistance). It is therefore beneficial to operate such mixers at higher field strengths (E > 60 V/cm), as suggested by the results in Figure 5.10.

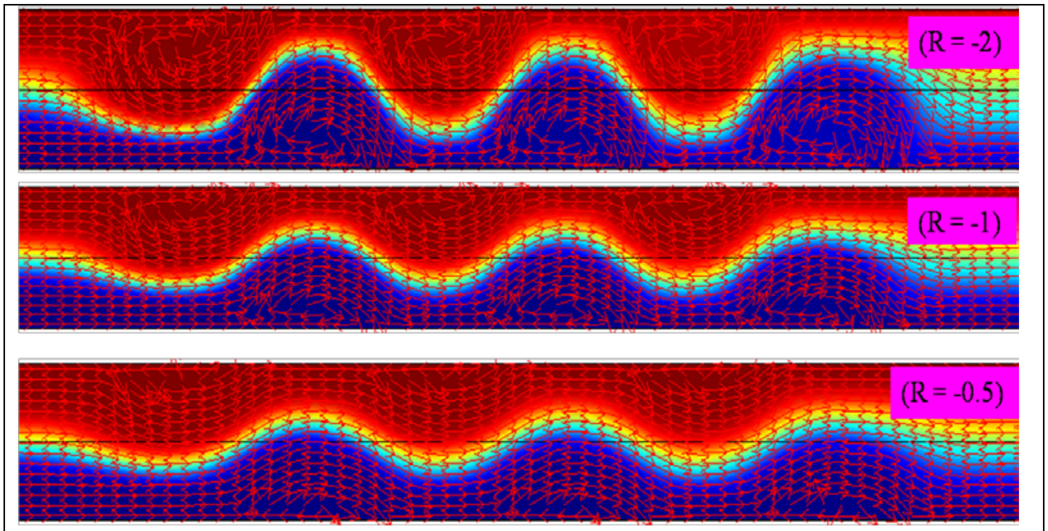

Figure 5.8: Species concentration surface plot and velocity arrow plot is shown for Heterogeneous charged walls mixer (Np = 3). The size of vortices increases with higher negative values of R resulting in better mixing.

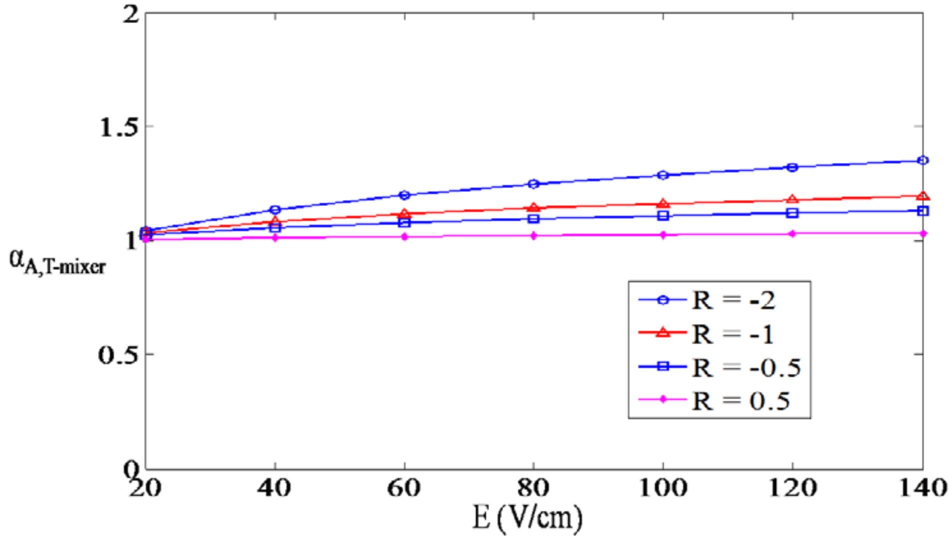

Figure 5.9: CMI plot for heterogeneous charged walls mixer for ratio of heterogeneous zeta potential to fixed zeta potential (R). The mixing performance increase with higher negative values of R.

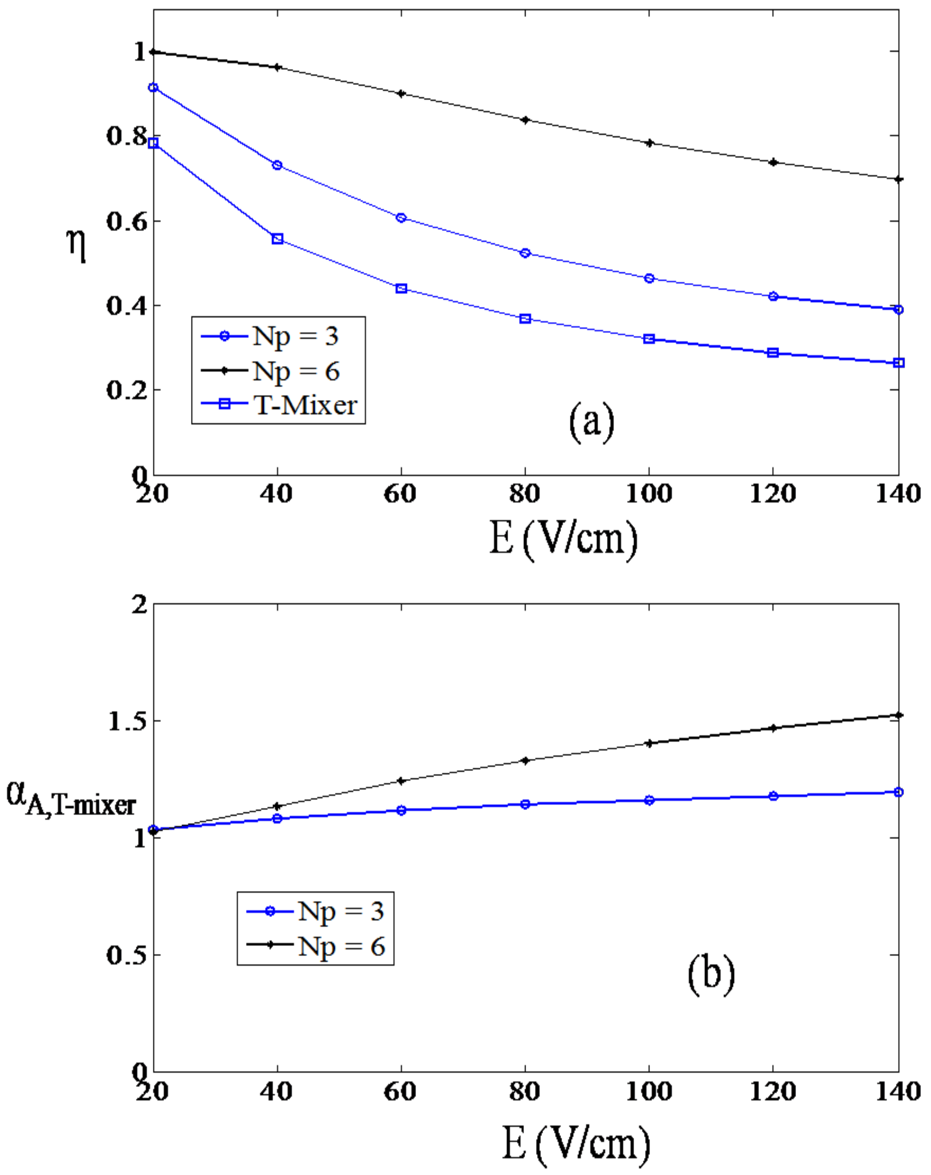

Figure 5.10: CMI and η values are plotted for heterogeneous charged wall mixer for Np = 3 and Np = 6. The mixing performance increases with number of heterogeneous patches. For E = 40 V/cm, though η values suggest superior mixing performance over T-mixer (a), CMI values implies a marginal improvement over T-mixer (b).

5.5 CMI dependence on electric field

The CMI dependence on electric field can be understood using scaling analysis presented below. The CMI can be alternatively written as follows:

$$\alpha_{A,T-mixer} = 1 + \frac{(\eta)_A\big|_{(L_c,\tau)} - (\eta)_{T-mixer}\big|_{(L_c,\tau)}}{(\eta)_{T-mixer}\big|_{(L_c,\tau)}} = 1 + \frac{\Delta\eta}{\eta_{T-mixer}}\Bigg|_{(L_c,\tau)} \tag{5.11}$$

The above equation relates the CMI to the relative increase in η value at same residence time. In the diffusion dominant conditions (at smaller fields), η_A, $\eta_{T\text{-}mixer}$ can be empirically related to the Peclet number (Pe) as:

$$\eta \sim \frac{a_1}{Pe^m} \sim a_1\left(\frac{D}{u_x w}\right)^m \tag{5.12}$$

Here m is the exponential factor representing the lumped effect of spatial concentration distribution and effective width (due to physical constriction and/or vortices) and a_1 is a constant (could be related to the interfacial contact area). For any arbitrary design A and T-mixer, η decreases with increase in electric field E, however, the CMI dependence on E is governed by the exponential factor m. For instance, η decay is slower for heterogeneous charged wall mixer as compared to a T-mixer ($m_{hetero} < m_{T\text{-}mixer}$), resulting in increase (positive $\Delta\eta$ in equation 5.11) in CMI value with electric field.

In the convective dominant regime (at higher electric fields), η would depend upon the dimensionless ratio of axial velocity to transverse velocity $\left(u_x/u_y\right)$ which is analogous to *Pe*. Therefore, equation 5.11 can be rewritten for convection dominant regime as follows:

$$\alpha_{A,T-mixer} \sim 1 + a_2\left[\frac{\Delta u_y}{u_x}\right] \sim 1 + a_2\left[\frac{\left(u_y\right)_A}{u_x}\right] \qquad \left[\because \quad \left(u_y\right)_{T-mixer} = 0\right] \tag{5.13}$$

Based on equations 5.12 and 5.13, the CMI dependence on electric field can be analyzed for various micro-mixers type. For ICEO micro-mixers, the ratio of transverse velocity to axial velocity scales linearly with electric field i.e. $\left(u_y/u_x \sim E^2/E \sim E^1\right)$ explaining the linear dependence of CMI on electric field (using equation 5.13) as shown in Figure 5.6a. In case of physical constriction and heterogeneous charge wall mixer, the transverse velocity as well as axial velocity scales linearly with electric field i.e. $\left(u_y/u_x \sim E/E \sim E^0\right)$. Therefore, at higher fields, CMI value should flatten out for both types of micro-mixer as observed in Figures 5.4 and 5.9.

5.6 Summary

A novel mixing index, based on residence time standardization, is proposed for micro-mixer performance evaluation. The proposed index identifies the true mixing benefits compared to the T-mixer by normalizing the effect of species residence time or reduced flow rate. The comparative mixing index (CMI) is employed for analyzing three electrokinetic mixing designs: (a) physical constriction mixer, (b) ICEO mixer, and (c) heterogeneously charged walls mixer. The equivalency of T-mixer and physical constriction type micro-mixer is shown using the proposed index. Various case studies demonstrate the advantage of CMI over the existing mixing index (η), as the former reveals the conditions under which a given mixing strategy is advantageous over a T-mixer. It is also demonstrated that comparisons based solely on the index η are inadequate and may be misleading in terms of mixing improvement over the T-mixer (see Figures 5.7 and 5.10). The CMI dependence on electric field is explained using scaling analysis in the limit of high electric field. The presented analysis can be extended to other mixing strategies and the CMI could be similarly useful for quantifying their performances.

Chapter 6

Induced Charge Electro-Osmotic Concentration Gradient Generator[#]

6.1 Introduction

Bio-molecule gradients play an important role in the understanding of various biological processes including wound healing, cancer metastasis, inflammation and embryogenesis. Typically, biological cells are exposed to linear and non-linear concentration gradients and their response is studied for understanding cell growth, cell migration and cell differentiation mechanisms. Several approaches are developed for bio-molecule gradient based studies such as Boyden chamber (Boyden 1962), Dunn chamber (Zicha et al. 1991), micro-pipettes (Ming et al. 2002) and hydrogels (Foxman et al. 1997). Although these conventional techniques are used for long time, these techniques have limitations in terms of gradient stability, reproducibility, predictability and controllability. For instance,

---

[#] A version of this chapter has been published. [M. Jain, A. Yeung and K. Nandakumar, Biomicrofluidics, 4, 014110 (2010)] the bio-molecules generated using hydrogels are highly variable and offers little control over the spatiotemporal gradient evolution. Such unpredictable quantitative nature and inability to establish user-defined gradients are not ideal for quantitative analysis of chemotaxis studies.

Recent advances in micro-fabrication technology have complemented this research field as many microfluidic devices are reported in the recent past for gradient generation (Jeon et al. 2002; Irimia et al. 2006; Li et al. 2007). Various microfluidic techniques are categorized into four different classes i.e. substrate-bound, time evolving, parallel flow, and flow resistive methods by Keenan and Folch (2008). As the name suggests, substrate-bound method involves binding of bio-molecules on the cell culture substrates via adsorption. This technique is found to be uncomplicated in terms of equipments and methods and gradients can be easily created. However, only limited gradient types can be generated owing to the technique dependence on various factors influencing adsorption kinetics such as temperature, number of functional sites, local concentration and steric hindrance. The time evolving gradient generators are appropriate for studies where temporal gradients are required and are not suited for studies where long exposure to a particular type of gradient is needed. In parallel flow type gradient generators, two or more solutions flow adjacently through a T-channel and gradient formation is due to transverse diffusion. Various modifications of basic T-channel gradient generator are reported which found to be adequate for generating various kinds of stable gradient patterns. Again, these types of generator require continuous supply of bio-molecules and exert flow induced forces on the biological cells. Lastly, flow resistive techniques provides near convection free gradient generation based on diffusion, however these methods found to be insufficient for complex gradient generation. Various conventional techniques and microfluidic techniques, their comparison and corresponding references can be found in an extensive review (Keenan and Folch 2008).

In this chapter, a novel microfluidic gradient generator is presented which utilizes the induced charge electro-osmotic flow to achieve stable, reproducible and dynamically controllable gradients. The proposed microfluidic device (details are presented in next section) is a modification of simplest parallel flow gradient generator, T- Sensor, with conducting obstacle suitably placed in the microchannel to exploit ICEK flows. Before we analyze the proposed design in detail, we review some of the most notable parallel flow type gradient generators with their advantages and limitations below.

In a T-sensor, the two confluent inlet streams of dissimilar fluids mix due to transverse diffusion and sigmoid shaped gradients can be generated. Various studies have used T-sensor based device to study bacterial chemotaxis (Mao et al. 2003), perform biological assays (Schilling et al. 2002) and cell chemotaxis with virus gradients (Walker et al. 2004). The main advantages of T-sensor are; simple geometric design which is easy to fabricate and generation of stable, reproducible gradients. On the downside, T-sensor requires high bio-molecule consumption due to continuous fluid flow. Jeon and coworkers (Jeon et al. 2002; Dertinger et al. 2001; Jeon et al. 2000) proposed a hierarchical network of T-channels, known as ‘Premixer Gradient Generator’, where solutions are splitted, mixed and recombined to arrive at a particular gradient type (Figure 6.1(a)). It was used to study the effect of bio-molecule gradients on neutrophil migration (Jeon et al. 2002), breast cancer cell chemotaxis (Saadi et al. 2006) etc. Although a variety of gradients can be generated with the proposed design, it is geometrically complex with limited dynamic controllability. In a similar study utilizing T-channel, Walker et al. (2004) observed the effect of virus gradients on biological cells. Another modification of the T-channel gradient generator is named as ‘Universal Gradient Generator’, shown in Figure 6.1(b) where Irimia et al. (2006) demonstrated the generation of complex gradient types. The user defined concentration profiles are developed by suitably positioning the dividers/walls to restrict the transverse diffusion. Again dynamic controllability is limited for the design as switching from one type of gradient to another type requires re-positioning of the dividers. Another study by Wang et al. (2006) provides a systematic representation of T-channel based gradient generators where the generator was decoupled into various microfluidic elements, which in turn were analytically modeled. Another study utilized stepwise addition of solute through micro-tunnel to achieve linear and non-linear axial gradients in microchannel (Li et al. 2007). All parallel flow type gradient generators provide stable gradients at the expense of continuous reagent consumption and are restricted in terms of dynamic controllability (Keenan and Folch 2008).

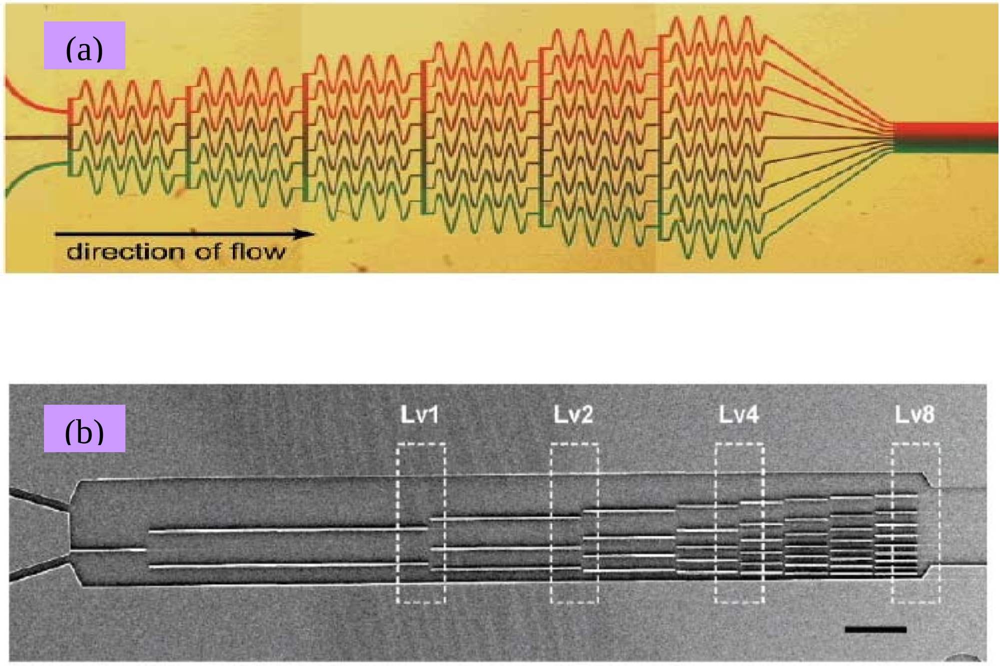

Figure 6.1: (a) 2D schematic of the ‘Premixer Gradient Generator’ (adapted with permission from Dertinger et al. 2001) and (b) A scanning electron micrograph of the ‘Universal Gradient Generator’ (adapted with permission from Irimia et al. 2006).

6.2 Proposed Design and Mathematical Model

The proposed design (top view shown in the Figure 6.2) consists of conducting half-cylinders, of radius *a*, embedded within the non-conducting channel wall. The conducting surface is assumed to be initially uncharged and highly polarizable, so that Faradaic reactions (i.e. electro-chemical reactions at the metal-electrolyte interface where electrons are transferred between the two phases by reduction or oxidation of ions in the electrolyte) at the interface are negligible. Although the flow in the channel is inherently three-dimensional, with the assumption of homogenous non-conducting top and bottom channel walls, essential flow features can be captured using a 2D model (Wu and Li 2008a) at considerably less computational effort, permitting a more detailed parametric study. A schematic of a sub-section is shown in Figure 6.3 to understand the FCEO and ICEO flow characteristics within the proposed design. The fixed negative charge will cause axial FCEO flow (linear dependence w.r.t. electric field), while the electric field will act on the induced charges to generate transverse ICEO flow (quadratic dependence w.r.t. electric field).

The characteristics of the developed concentration gradient are dependent upon the interplay between fixed charge electro-osmotic (FCEO) and ICEO flows. For the proposed design, the concentration gradient formation in the microchannel is governed by the following mechanisms; (a) transverse diffusion (b) axial convection due to FCEO flow and (c) transverse convection which originate due to ICEO flow.

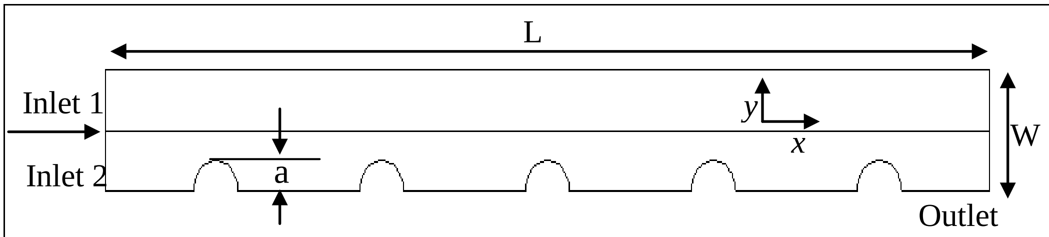

W: channel width, L: channel length, a: radius of conducting cylinder

Figure 6.2: Top-view of the proposed design.

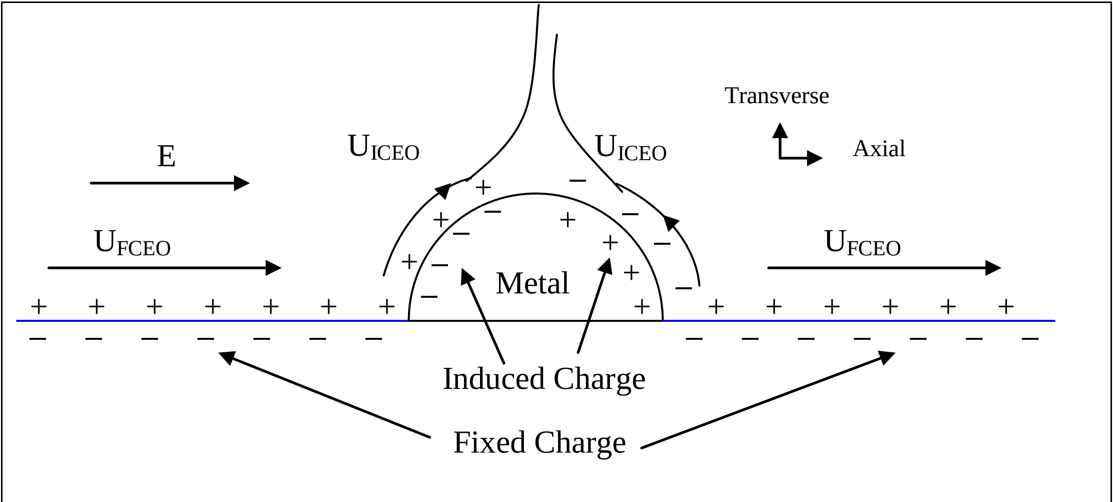

Figure 6.3: Schematic showing FCEO slip velocity on (fixed negatively charged) non-conducting wall and ICEO slip velocity on polarizable metal surface (charges are induced due to external electric field) in the design sub-section. The charges on the solid surface attract counter-ions from the electrolyte solution and form electric double layer (EDL).

With very weak external applied field, the FCEO and ICEO flow are weak due to linear and quadratic dependence on electric field respectively. Therefore for small field strength, diffusion is the dominant mechanism and yields a constant concentration profile at the exit. At intermediate field strength, FCEO flow will govern the gradient formation resulting in an error function type profile (which can be approximated as linear profile (Wang et al. 2006)) and at high fields, ICEO flow will induce transverse convection locally (near conducting obstacle) to generate asymmetric and non-linear gradients. Further, the degree of transverse flow in the microchannel can be altered by the magnitude of the applied field and by the shape of the conducting protrusion. The proposed design is geometrically simple and can switch between various gradients type just by altering applied electric field and more importantly, without altering the device geometry as demonstrated later in the results section. The small time scales associated with electro-kinetic and induced-charged electrokinetic flows (Squires and Bazant 2004) make it a promising candidate for achieving dynamic controllability while retaining the simple T-channel geometry.

To describe the mathematical model, we introduce the following reference quantities and dimensionless variables:

$$L_{ref} = W,\ \psi_{ref} = \frac{K_b T}{ze},\ c_{ref} = c_{0,}\ E_{ref} = \frac{\psi_{ref}}{L_{ref}},\ u_{ref} = \frac{\varepsilon_0 \varepsilon_r \psi_{ref}}{\mu} E_{ref} \quad \&$$

$$\overline{x} = \frac{x}{L_{ref}},\ \overline{y} = \frac{y}{L_{ref}},\ \overline{\psi} = \frac{\psi}{\psi_{ref}},\ \overline{c}_i = \frac{c_i}{c_{ref}},\ \overline{u} = \frac{u}{u_{ref}}, \overline{E} = \frac{E}{E_{ref}},\ \overline{p} = \frac{p}{\rho u_{ref}^2},\ \overline{q}_s = \frac{q_s L_{ref}}{\varepsilon_0 \varepsilon_r \psi_{ref}}$$

The notations/symbols, along with all default parameter values used in the simulation, used above are described in Table 6.1. The non-conducting channel walls are negatively charged, and the conducting metal surface will acquire surface charges as an electric field is applied. A 1:1 electrolyte is used in the simulation with constant diffusivity D for both types of ions. Also, the solution is assumed to be an incompressible, Newtonian fluid with fixed dielectric constant ε_r, viscosity μ, and density ρ.

As outlined earlier in section 2.4, the steady ICEO flow problem can be solved using two approaches: (1) The Poisson-Nernst-Planck (PNP) model, and (2) Correction potential method–slip velocity model. The full Poisson-Nernst-Planck model resolves the electric double layer and solves for electrolyte ion concentration distributions. The Poisson-Nernst-Planck model has been found to be computationally intensive as compared to the Correction method (Jain et al. 2009a). On the other hand, Correction method (Wu and Li 2008a; Wu and Li 2008b) is a numerical approach for estimating the induced zeta potential on a conducting surface and further utilizes it to estimate the slip velocity at a conducting surface (adopting the Smoluchowski limit for thin EDL). We have also utilized this approach to arrive at the optimal obstacle shape for ICEO mixers (Jain et al. 2009b) as outlined in chapter 4. In this study, we have used both models, initially PNP model to demonstrate the concept and correction method towards the end; for generation of user-defined concentration gradients.

Table 6.1: Simulation Parameters (default values)

Parameter	**Value**	**Description**
W	100 μm	Width of the microchannel
κW	100	Ratio of channel width to Debye length (PNP model)
a	25 μm	Radius of conducting half-cylinder
L	1 mm	Length of microchannel
D	1e-9 m^2/s	Diffusivity of electrolyte ions (PNP model)
D_s	1e-11 m^2/s	Diffusivity of the species (bio-molecule)
ς_f	-25 mv	Fixed zeta-potential on non-conducting wall

(a) Poisson – Nernst – Planck (PNP) model

In the fluid domain, the Poisson equation relates the electric potential ψ to the charge densities. In its non-dimensional form, the Poisson equation is:

$$\overline{\nabla}\cdot(-\overline{\nabla}\,\overline{\psi}) = \frac{1}{2}\kappa^2 W^2(\overline{c}_1 - \overline{c}_2) \tag{6.1}$$

The above equation relates the electric potential to the volumetric charge densities. In the above equation, $\overline{\nabla}$ is the dimensionless gradient operator, W is the channel width, $\overline{c}_1$ and $\overline{c}_2$ are the scaled concentration of positive and negative electrolyte ion respectively and κ is the inverse of Debye length given by

$$\kappa = \left(\frac{2z^2e^2N_Ac_0}{\varepsilon_0\varepsilon_rK_bT}\right)^{\frac{1}{2}} \tag{6.2}$$

In equation 6.2, z is the valence of the electrolyte ions, e is the elementary charge, N_A is the Avogadro number, c_0 is the bulk electrolyte concentration and K_b, T, ε_0 represent Boltzmann constant, absolute temperature and permittivity of free space.

As the electrolyte ions cannot penetrate inside the metal cylinders, the electric potential distribution is given by the Laplace equation inside the metal domain:

$$\overline{\nabla}\cdot(-\overline{\nabla}\,\overline{\psi}) = 0 \tag{6.3}$$

At the channel inlet, a constant potential V_0 relative to the outlet potential is applied, giving rise to a steady electric field *E* in the *x* direction. Also, a constant surface charge density q_s is imposed on the channel walls and potential continuity is applied at the metal-fluid interface. The electric displacement (D_E) may or may not be continuous at the metal-electrolyte interface depending upon the presence of surface charge. Considering an initially uncharged cylinder, the interfacial boundary condition can be written as $n.(D_1\text{-}D_2) = 0$, as used by Zhao and Bau (2007b).

The flow field in the fluid domain is governed by the continuity and Navier-Stokes equations. These equations, in their dimensionless forms, are:

$$Re(\overline{u} \cdot \overline{\nabla}\overline{u}) = -\overline{\nabla}\overline{p} + \overline{\nabla} \cdot (\overline{\nabla}\overline{u}) - \frac{1}{2}\kappa^2 W^2 (\overline{c}_1 - \overline{c}_2)\overline{\nabla}\,\overline{\psi} \tag{6.4a}$$

$$\overline{\nabla} \cdot \overline{u} = 0 \tag{6.4b}$$

In the equation 6.4a, the rightmost term is due to the electrical body force within EDL and *Re* is the Reynolds number (ratio of inertial forces to viscous forces) and can be written as:

$$Re = \frac{L_{ref} u_{ref} \rho}{\mu} = \frac{\varepsilon_0 \varepsilon_r W K_b T \rho}{ze\mu^2} \tag{6.5}$$

A steady state ion conservation equation can be written for electrolyte ions in domain 1, with the Peclet number Pe (ratio of convective transport to diffusive transport) appearing with the convective term as

$$Pe(\overline{u} \cdot \overline{\nabla}\overline{c}_i) = \overline{\nabla} \cdot (\overline{\nabla}\overline{c}_i) + \overline{\nabla} \cdot (\overline{c}_i \overline{\nabla}\,\overline{\psi}) \tag{6.6}$$

The Peclet number is defined as

$$Pe = \frac{u_{ref} L_{ref}}{D} = \frac{\varepsilon_0 \varepsilon_r \left(K_b T\right)^2}{\mu D \left(ze\right)^2} \tag{6.7}$$

For fluid flow, zero pressure conditions are imposed at the inlet and outlet, while the no slip condition is imposed at fluid-solid boundaries. Similarly, zero flux condition is imposed at the channel walls including metal surface for electrolyte ions and other species.

(b) Correction Potential method

Assuming thin EDL, the electric potential distribution at steady state can be described using the Laplace equation. In non-dimensional form, the Laplace equation is

$$\overline{\nabla}^2 \overline{\psi} = 0 \tag{6.8}$$

A steady electric field E is applied in the x direction (as mentioned earlier for PNP model) and at the channel as well as the obstacle surface, normal component of electric field is specified as zero i.e. $n.\nabla\psi = 0$.

The flow field in the computational domain is governed by the continuity and Navier-Stokes equations. These equations, in their dimensionless forms, are

$$Re(\overline{u}\cdot\overline{\nabla}\overline{u}) = -\overline{\nabla}\overline{p} + \overline{\nabla}^2\overline{u} \tag{6.9a}$$

$$\overline{\nabla}\cdot\overline{u} = 0 \tag{6.9b}$$

It should be noted that the electrical force term in the Navier-Stokes equation is accounted by the slip velocity boundary condition as given by the Helmholtz-Smoluchowski's equation:

$$\overline{u} = \overline{\varsigma}\,\overline{E} \quad where \begin{Bmatrix} \overline{\varsigma} = \overline{\varsigma}_f \ \ at\ non\text{-}conducting\ surface \\ \overline{\varsigma} = \overline{\varsigma}_i \ \ at\ conducting\ surface \end{Bmatrix} \tag{6.10}$$

In the above equation, ς_f is the fixed zeta potential on the non-conducting surface, whereas ς_i is the induced zeta potential on the conducting surface; the magnitude of ς_i is dependent on the applied electric field as well as on the obstacle shape.

The induced zeta potential is estimated using the Correction method (Wu and Li 2008a) as follows:

$$\bar{\varsigma}_i = -\overline{\psi} + \overline{\psi}_c \tag{6.11}$$

Here ψ_c is the constant correction potential given by

$$\psi_c = \frac{\int_s \psi \; dA}{A} \tag{6.12}$$

In the above equation, *A* represents the surface area of the conducting obstacle. At the inlet and outlet zero pressure conditions are imposed, while Smoluchowski's slip condition (equation 6.10) is imposed at fluid-solid boundaries. For calculation of slip velocity, fixed zeta potential ς_f is imposed on the non-conducting channel walls, whereas induced zeta potential ς_i is calculated using equations 6.11 and 6.12. It should be noted that ICEO slip velocity has quadratic dependence on electric field as induced zeta potential scales linearly with electric field. Therefore, at high electric fields ICEO flow dominates within the microchannel.

The steady state ICEO flow problem can be solved using any one of the models outlined above. Further, the steady transport of the species is governed by the convection-diffusion equation and can be written in dimensionless form as:

$$(\overline{u} \cdot \overline{\nabla} \overline{c}_s) = \overline{\nabla} \cdot (\overline{\nabla} \overline{c}_s) \frac{D_s}{u_{ref} L_{ref}} \tag{6.13}$$

In the above equation, $\overline{c}_s$ and D_s represent species concentration and diffusion coefficient, respectively. For species transport, a constant concentration condition is imposed at the channel inlets (i.e. scaled concentration of 1 and 0 at inlet 1 and inlet 2 respectively). The aforementioned condition is implemented at the inlet boundary using a smoothed Heaviside function (with continuous second derivative). Further, it is assumed that species concentration is sufficiently low such that it doesn't affect the flow profile. At the conducting surfaces and non-conducting channel walls, zero flux condition is imposed for the species, while convective-flux only boundary condition is applied at the channel outlet. The above model is solved using the direct (UMFPACK) solver available within the commercial finite element method package, COMSOL 3.4. Due to ICEO flows, the location of the interface between two streams varies spatially; hence adaptive meshing is employed for accurate solution near the interface. For full PNP model, fine meshes are used near wall and polarizable obstacles (so as to resolve the EDL accurately) and the results presented in the section below are mesh-independent.

6.3 Results and Discussion

Initially, the full PNP model is compared with correction potential approach for the proposed design and the results for exit species concentration profile are shown in Figure 6.4. The obtained results suggest a good agreement between two approaches even for induced zeta potential higher than thermal voltage. However, the error between the two approaches increases with increasing electric field/ induced zeta potential. To ensure accuracy, full PNP model is used for analysis, except for the optimization part, which requires iterative solution and correction approach is best suited in terms of computational effort.

In Figure 6.5, induced zeta potential is plotted along the length of conducting surface (L_{cs}) for various applied field strength. As evident from the Figure 6.5, the induced zeta potential increases linearly with applied field with close to 8 times of thermal voltage for E = 4000 V/m, whereas ς_f = –25mV. A very fine mesh (minimum element size ~ 1e-3) is employed at the solid-fluid boundary (Figure 6.6a), for accurate estimation of gradients in the EDL. The next plot (Figure 6.6b) shows the surface plot for α, where $\alpha = \overline{c}_1 - \overline{c}_2$ is the difference between positively and negatively charged electrolyte ion concentrations. The variable α represents the excess charge and takes on positive and negative values at the left and right half of the semi-cylinder, respectively (due to induced charges). Also, a cross-sectional plot for α is shown in Figure 6.6c. Both Figures 6.6b & 6.6c suggest that the α value goes to zero outside the EDL, confirming electro-neutrality (or uniform bulk conductivity) outside the EDL.

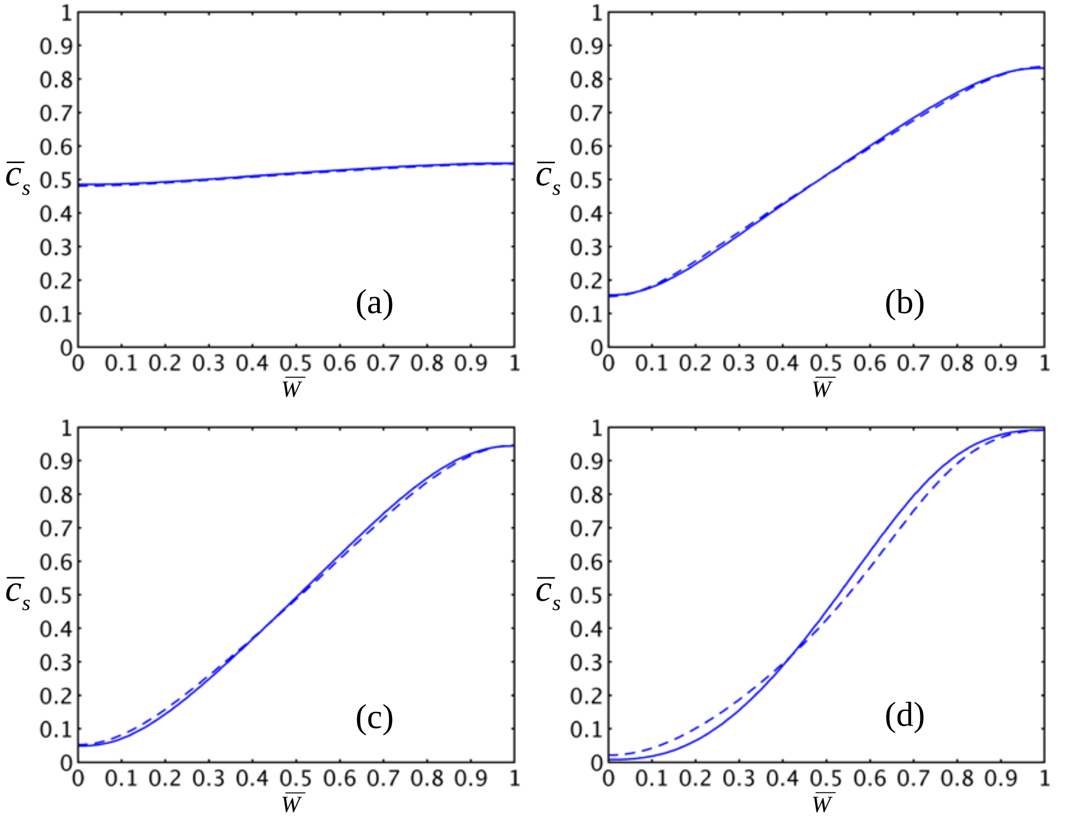

Figure 6.4: Comparison between full PNP model (dashed lines) and correction method (solid lines) for ς_f = –50mV at various fields i.e. (a) E = 200 V/m, (b) E = 1000 V/m, (c) E = 2000 V/m and (d) E = 4000 V/m. The error between the results increases as electric field/ induced zeta potential is increased. For E = 4000 V/m, the magnitude of ς_i ~ 8 times of thermal voltage (25mV) and error is 5.5%.

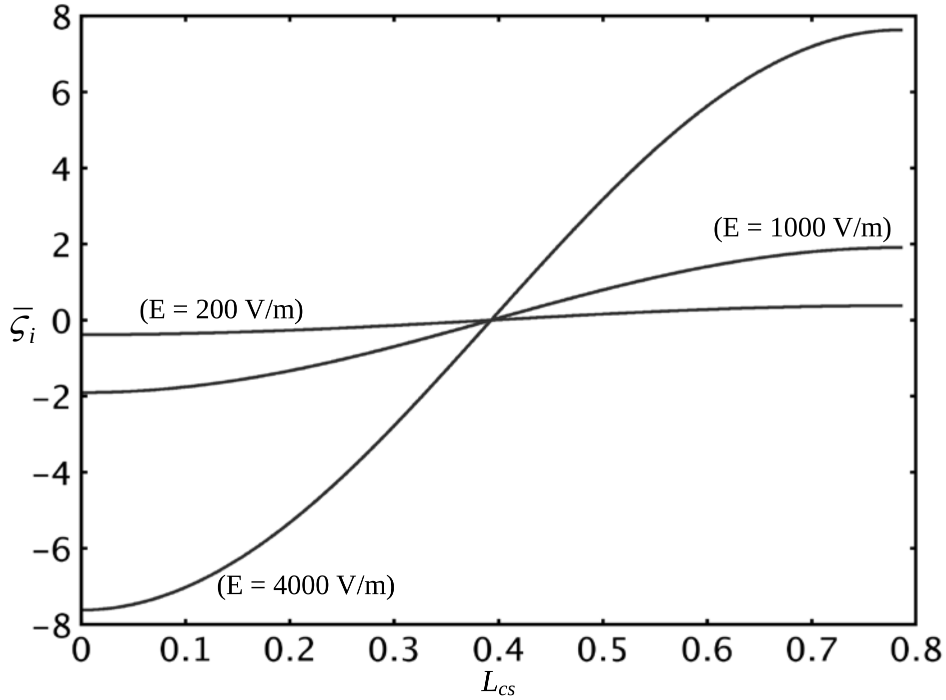

Figure 6.5: Induced zeta potential plotted along the conducting surface. The magnitude of induced zeta potential scales linearly with applied electric field.

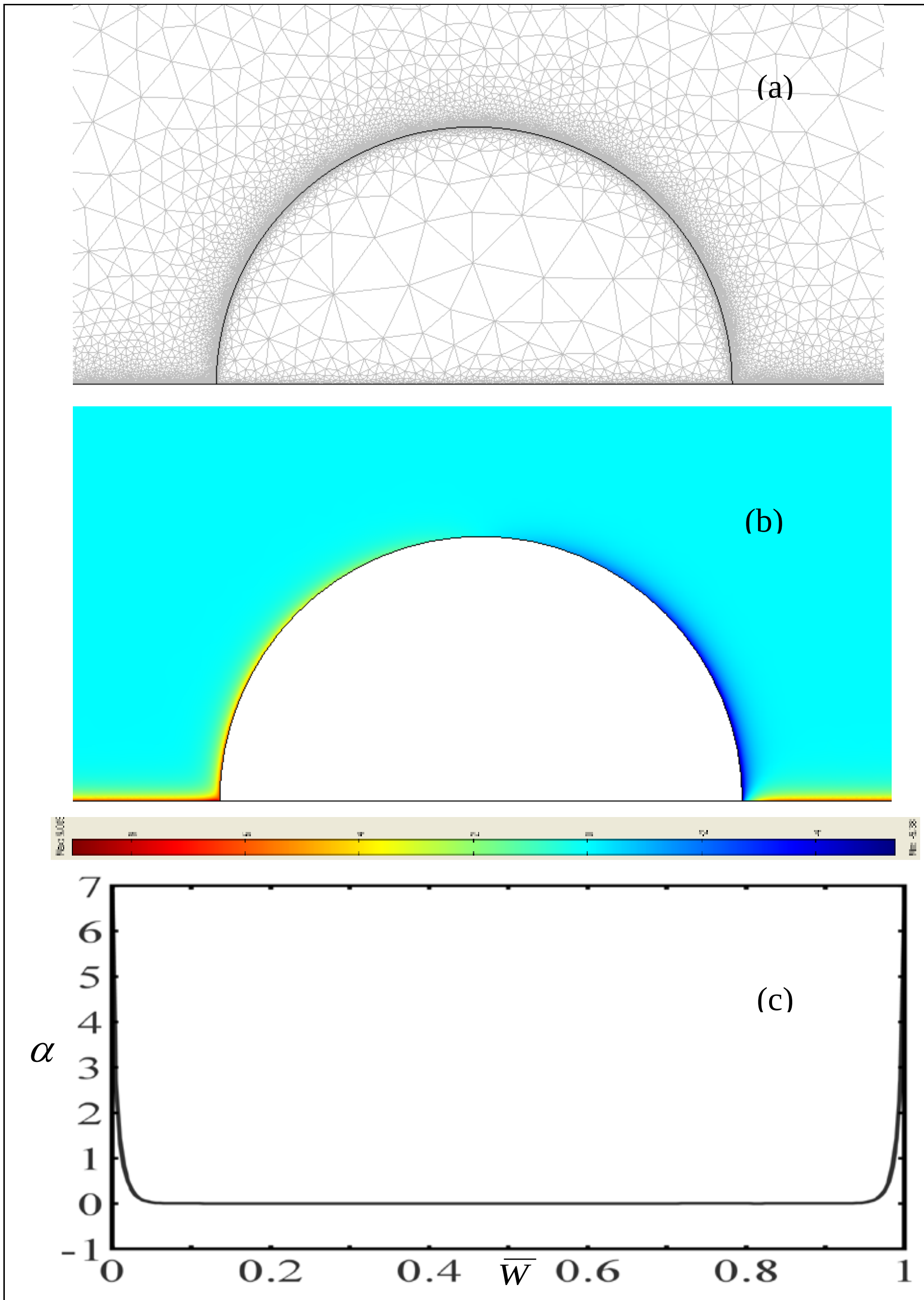

Figure 6.6: (a) The applied unstructured mesh is plotted near the interface. The extremely fine mesh at interface is used to capture the gradients in EDL (electric double layer). (b)The excess charge α is plotted as surface plot. (c) The cross-section plot for excess charge is shown. The excess charge is contained in the thin EDL and the bulk is electro-neutral corresponding to α = 0 as seen in (b) & (c).

Next we analyze the fluid streamlines near the conducting surface (Figure 6.7) and its effect on the species concentration (Figure 6.8 and Figure 6.9) with respect to the electric field strength. At small field strength (E = 200 V/m), the flow is weak and due to transverse diffusion, a constant concentration profile is obtained at the exit as shown in Figure 6.8a and profile (a) in Figure 6.9. With increase in electric field strength, the FCEO and ICEO flow starts to overcome diffusion, resulting in an error function concentration profile at the exit as observed in Figure 6.8b and profile (b) in Figure 6.9. Upon further increase in electric field, ICEO flow dominates near the conducting surface which results in an increased vortex size as seen in Figure 6.7. The strong circulations near conducting obstacle directly affect the species concentration as observed in Figure 6.8c and 6.8d. It should be noted that ICEO doesn’t mix the species rather alters their path by creating an additional resistance through flow circulations. The transverse convection generated due to non-linear slip at conducting surface can be utilized to generate asymmetric and non-linear gradients as observed in profile (c) in Figure 6.9. The non-linear and asymmetric nature of generated gradient (Figure 6.9c) is due to ICEO flow circulations and this non-linearity increases as the test cross-section is moved closer to obstacle as shown in Figure 6.10.

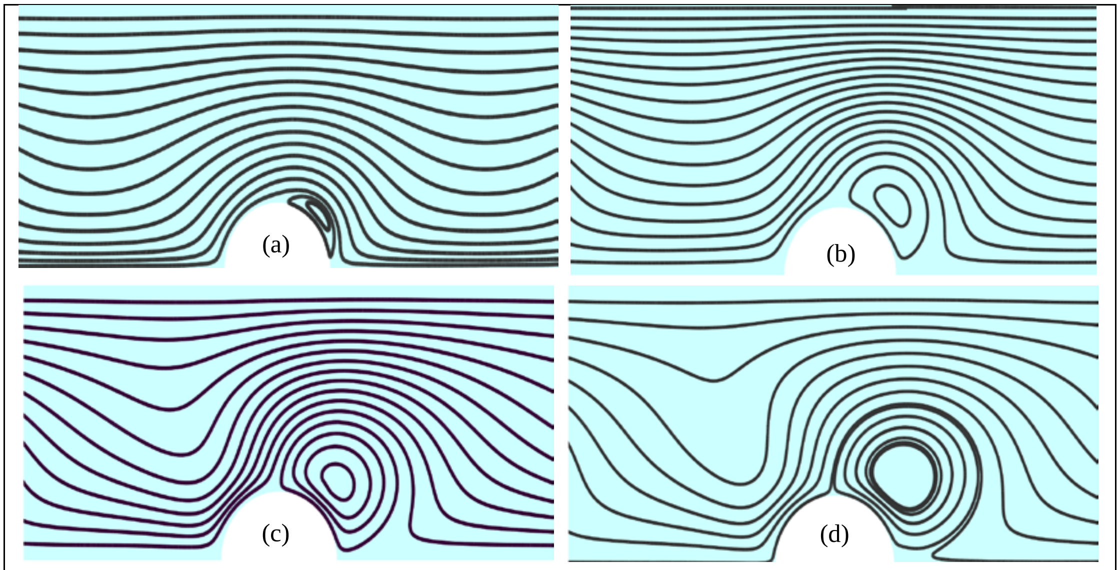

Figure 6.7: Fluid streamlines near the conducting obstacle corresponding to electric field of (a) 200 V/m, (b) 1000 V/m, (c) 4000 V/m and (d) 6000 V/m. The ICEO flow (and size of the vortex) increases with electric field. Further increase in electric field will generate another vortex to the left of conducting obstacle.

Further, the magnitude of the transverse velocity component can be altered by the applied field strength as well as by the shape of the conducting surface. Therefore, by employing a range of such conducting obstacles (with different shapes & sizes), transverse convection of varying magnitude can be introduced at different spatial locations in the channel and can be exploited to attain user-defined concentration profiles.

An optimization problem is formulated for generating user-defined profiles (Figure 6.11), where objective function is defined as the squared difference between the cross-section species concentration profile and the targeted user-defined function i.e. $e = \left(\bar{c}_s - c^*\right)^2$. The objective function is minimized using genetic algorithms with electric field (E) and conducting cylinder radii (a_i, $i = 1$-5) as parameters. The lower and upper bounds for a_i are chosen as [0.05w - 0.45w], while electric field could take any value between 10(*V/cm)* and 150(*V/cm).*

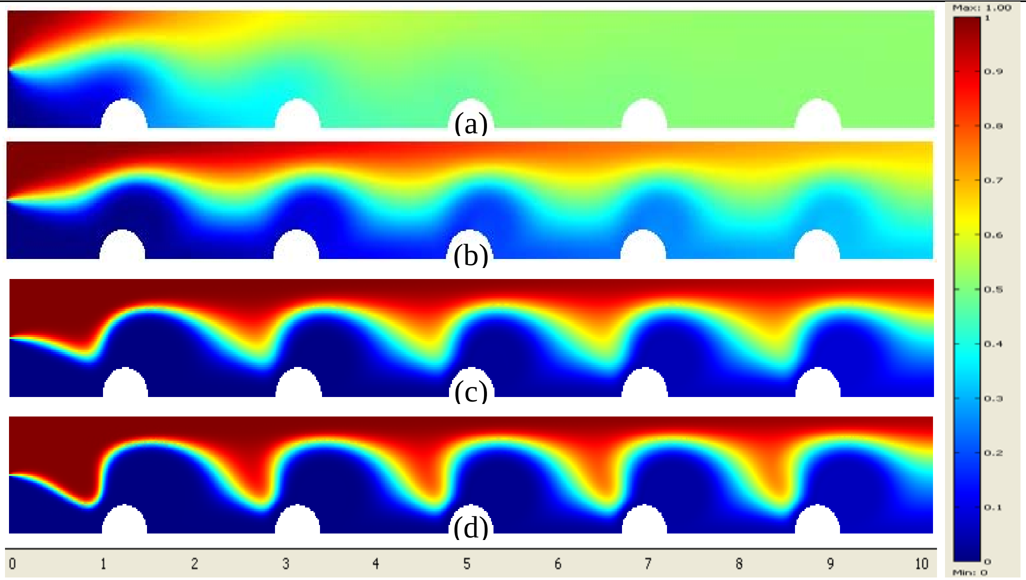

Figure 6.8: Species concentration surface plot for various regimes i.e. (a) diffusive regime (E =200 V/m), (b) FCEO flow regime (E = 1000 V/m) and (c) & (d) ICEO flow regime (E = 4000 V/m & E = 6000 V/m).

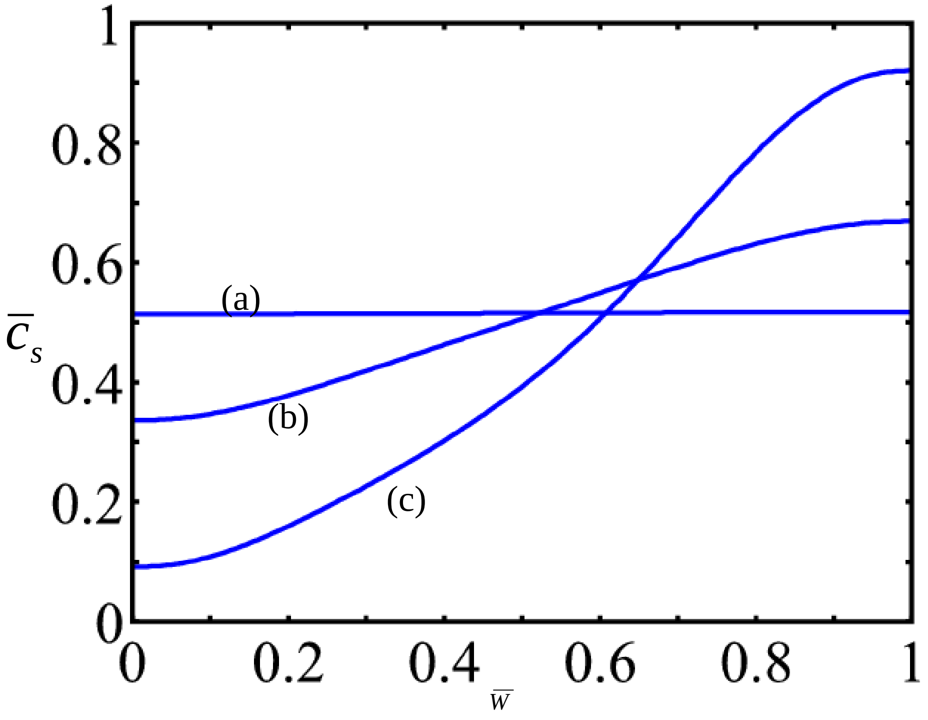

Figure 6.9: Cross-sectional species concentration profile at exit for (a) E = 200, (b) E = 1000 & (c) E = 4000 (in V/m). The obtained profiles correspond to diffusive, FCEO and ICEO dominant operating regimes respectively.

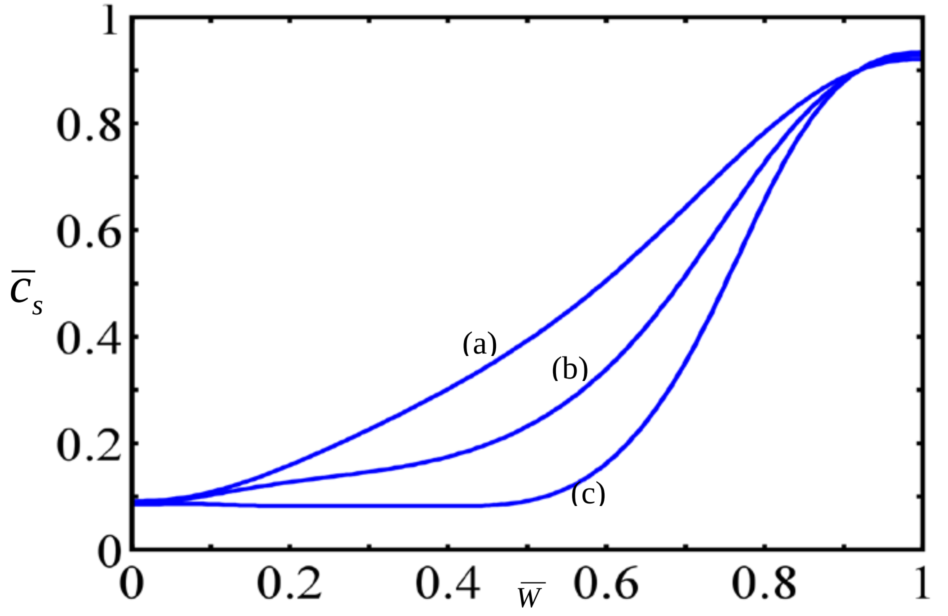

Figure 6.10: Cross-sectional species concentration profile for E = 4000 at various test cross-sections i.e. (a) at $\overline{L} = 10$ (exit); (b) at $\overline{L} = 9.5$ and (c) at $\overline{L} = 9.2$. The non-linearity and asymmetric nature of gradient increases for test-section closer to the obstacle.

As mentioned earlier, the gradient properties are governed by the interplay of diffusion, FCEO and ICEO. Therefore, it is important to note that there could be multiple solutions for obtaining a user-defined profile e.g. a similar profile can be obtained via an alternate combination of D_s, E, ς_f or with different shape/size of conducting obstacle. For example, if there is a different species with higher or lower diffusion coefficient, a similar concentration profile could be obtained with application of higher or lower electric field respectively. Further, the non-linearity in the gradient occurs with dominant ICEO flows which depend on size/shape of conducting obstacle and externally applied field. For instance, for a given electric field variation in obstacle radii will generate transverse flows of varying magnitude at different spatial location (Figure 6.11), thereby adding non-linearity to the gradient, which is the unique feature of the proposed design. The proposed design is also advantageous in terms of dynamic controllability, the ability to change the gradient during mid-experiments. As demonstrated earlier in Figure 6.8, just by altering the applied field strength and keeping all other parameters same, the proposed design can easily switch from linear gradient to a non-linear gradient. Also, the time scales associated with FCEO/ICEO flows are quite small (~ order of 10^{-4} sec, (Squires and Bazant 2004)), which suggests rapid formation of non-linear gradients and therefore offers an enhanced controllability for the proposed design.

(a) Linear profile (error = 2.74%)

$$c^*(y) = y$$

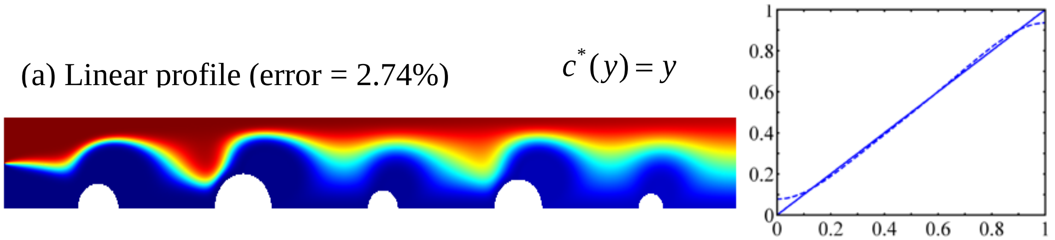

(b) Concave profile (error = 2.93%)

$$c^*(y) = y^{3/2}$$

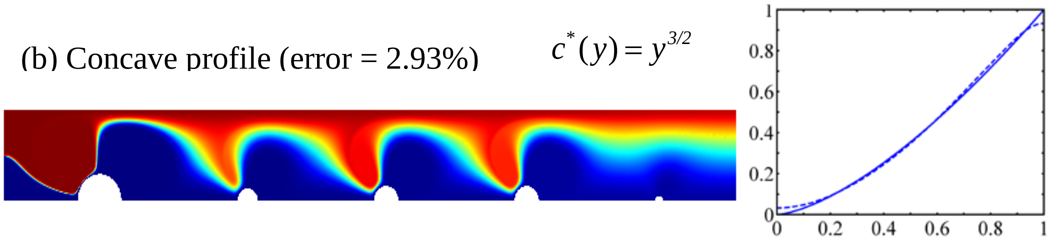

(c) Convex profile (error = 2.44%)

$$c^*(y) = \frac{erf(y)}{erf(1)}$$

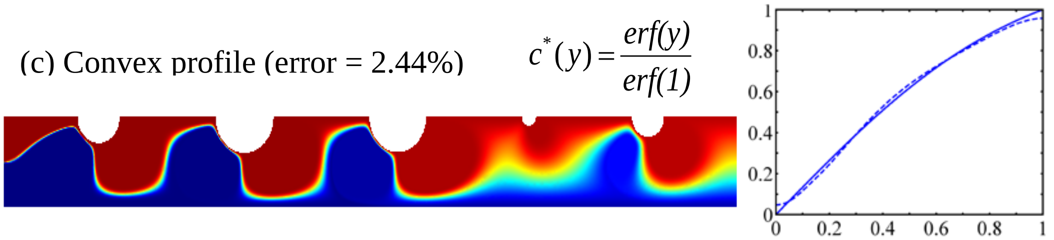

Figure 6.11: Concentration surface plots and comparison between targeted profile (solid line) and numerically obtained profile (dashed line).

6.4 Summary

A new microfluidic device is proposed for concentration gradient generation based on the interplay between Induced charge electro-osmotic (ICEO) and Fixed charge electro-osmotic (FCEO) flows. In comparison with the other reported designs, the proposed method is geometrically simpler and has the unique characteristic of inducing transverse flows locally which can be controlled by the magnitude of the applied field and by the shape of the conducting protrusion. For analysis, both full PNP (Poisson-Nernst-Planck) model and correction method based on slip-velocity approach are used to model the steady ICEO flow. It is shown that the proposed device is capable of generating variety of gradients and could switch between linear and non-linear gradients by simply altering the applied electric field, demonstrating the superior dynamic controllability of the proposed design.

Chapter 7

Conclusions and Outlook

7.1 Summary and key contributions

This study began with the development of numerical models for steady state ICEO flow. For analysis, both fully coupled non-linear PNP model and simplified slip-velocity models were developed and the results were validated with the analytical solution available for ICEO flow around a perfectly conducting (ideally polarizable) cylinder in infinite medium (section 2.6). The observed quadrupolar flow patterns and associated vortices in ICEO flows were immediately perceived as beneficial from micro-mixing perspective. Subsequently, a novel micro-mixing strategy was proposed based on ICEO flows (chapter 3). The proposed design was geometrically simpler and utilized symmetric micro-vortices in the vicinity of polarizable cylinder to enhance micro-mixing. Another unique feature of the proposed design was its ability to induce transverse flow locally which can be controlled by the magnitude of applied electric field.

The obstacle shape optimization study (chapter 4) for the ICEO mixer was driven by the fact that induced zeta potential or induced charge on the polarizable surface is the function of obstacle's shape. The distribution of induced charges on the polarizable surface governs the local flow patterns which in turn affects the mixing performance. NURBS (Non-Uniform Rational B-Splines) based shape optimization technique was utilized to identify the optimal obstacle shape for the ICEO mixer. The effect of obstacle shape on mixing performance was identified and the evolution of optimal shapes from a diffusive regime to an ICEO-dominant regime was demonstrated. It was shown that right triangle shaped obstacle provides optimal mixing performance at higher electric fields whereas the rectangular shape is optimal in the diffusive regime. By completely resolving the optimal obstacle shape problem, my study has provided design guidelines for an experimentalist to maximize/ design suitable ICEO based micro-mixer for any particular application.

The next part of this dissertation focused on identifying suitable measures for micro-mixing performance evaluation and was fuelled by the results obtained from the optimization study. In chapter 5, we proposed a novel index, based on residence time, for micro-mixing characterization and comparative analysis. The proposed comparative mixing index (CMI) is advantageous over existing indices as it identifies the non-diffusive mixing benefits by normalizing the effect of species residence time or reduced flow rate. The proposed index clearly identifies optimal regimes of operation and important design parameters for various types of micro-mixer. The most important advantage of this index is the decision support it can offer to the experimentalists/ design engineers for comparing various mixing strategies and to design/characterize micro-mixer for specific microfluidic application.

In chapter 6 of this thesis, a new design was introduced for microfluidic concentration gradient generator based on ICEO flows. The bio-molecule gradients are routinely used in experimental cell biology for studies involving growth, differentiation and migration of biological cells. The characteristics of the developed concentration gradient are dependent upon the relative strength of FCEO and ICEO flows. Using parametric optimization, the formation of user-defined concentration profiles (linear, convex & concave) was demonstrated. The proposed design was found to be superior to previously reported devices due to its uncomplicated geometry and better dynamic controllability.

In general, this study employed numerical simulations (using commercially available finite element solvers) to gain fundamental understanding of induced charge electrokinetic (ICEK) transport phenomena. The developed theoretical understanding of the phenomena was further applied to design ICEO micro-mixer and ICEO concentration gradient generator. The developed designs were further optimized (geometrically and parametrically) to attain optimal/ user defined functionality. Lastly, a novel performance indicator was developed for assessment of any parallel flow type micro-mixer design.

7.2 Recommendations for future research

ICEK is identified as one of the most promising technology for LOC devices (Squires 2009), ‘Induced-charge electrokinetic phenomena’ identified as fast moving front by Thompson Scientific (2007)). However, In comparison to linear/ classical electro-kinetics, the study of ICEK phenomena is still in its early stage. There are various opportunities/ challenges that need to be addressed before we can realize the full potential of ICEK in microfluidic-LOC devices.

From a theoretical viewpoint, there is a sufficiently wide gap between theory and experimental results (Squires 2009). For example, the strong dependence of ICEK velocities on electrolyte concentration is not theoretically explained. The observed ICEK velocities are found to be immeasurably small for salt concentration in excess of 10mM. Another challenge is the quantitative disagreement between theoretical and experimental magnitudes for ICEK velocities. While the observed qualitative and scaling features ($u \sim E^2$ and ICEK flow patterns) match well with theory, the experimentally measured ICEK velocities are always over predicted by the theoretical models within a range of factor of 3 and at times by orders of magnitude (Squires 2009; Bazant et al. 2009b; Bazant et al. 2009a) .The first quantitative agreement between theory and experiments (for nearly 1000 distinct experiments encompassing a wide range of conditions) has been recently reported (Pascall and Squires 2010b; Pascall and Squires 2010a) for ICEO flows over controllably contaminated surface. There are also very interesting non-linear effects such as ACEO flow reversal (observed experimentally at high voltages and high frequencies) which cannot be explained theoretically so far (Bazant et al. 2009a; Olesen et al. 2006; Gregersen et al. 2007). Only very few experimental (mostly ACEO flows) studies were reported with reference to ICEK flows. Most of the experimental studies are carried out with NaCl or KCl solution using gold/ platinum electrodes. Further exploration with additional electrode materials and other electrolytes may reveal some interesting results and enable the development of better theoretical models (Squires 2009). From applications perspective, the ICEK flows are largely unexplored and only few applications were reported in the field of pumping and mixing (Olesen et al. 2006; Urbanski et al. 2007; Bazant and Ben 2006; Lastochkin et al. 2004; Jain et al. 2009a; Jain et al. 2009b; Wu and Li 2008a; Harnett et al. 2008; Zhao and Bau 2007a). The development of theoretical models as well as experimental techniques for ICEK flows and ICEK motion of particles would definitely increase its applicability in field of biology and LOC devices.

Micromixing technology has experienced rapid development in the past few years (Nguyen and Wu 2005; Aubin et al. 2010; Chang and Yang 2007; Hardt et al. 2005). However, systematic evaluation of these techniques is required in order to clearly distinguish an appropriate mixing strategy for a given application. Another challenge is to develop high throughput continuous micro-mixing techniques since majority of electrokinetic micro-mixers have reported a trade-off between mixing and flow transport (Jain et al. 2009b; Chang and Yang 2007; Tian et al. 2005; Jain and Nandakumar 2010).

Bibliography

Ajdari, A. (1995). "Elctroosmosis on Inhomogeneously Charged Surfaces." *Phys.Rev.Lett.*, 75(4), 755-758.

Ajdari, A. (2000). "Pumping liquids using asymmetric electrode arrays." *Physical Review E,* 61(1), R45-R48.

Anderson, J. L. (1989). "Colloid Transport by Interfacial Forces." *Annu.Rev.Fluid Mech.,* 21 61-99.

Atalay, Y. T., Witters, D., Vermeir, S., Vergauwe, N., Verboven, P., Nicolai, B., and Lammertyn, J. (2009). "Design and optimization of a double-enzyme glucose assay in microfluidic lab-on-a-chip." *Biomicrofluidics,* 3(4), 044103.

Aubin, J., Ferrando, M., and Jiricny, V. (2010). "Current methods for characterising mixing and flow in microchannels." *Chemical Engineering Science,* 65(6), 2065-2093.

Bau, H. H., Zhong, J. H., and Yi, M. Q. (2001). "A minute magneto hydro dynamic (MHD) mixer." *Sensors and Actuators B-Chemical,* 79(2-3), 207-215.

Bazant, M. Z., and Squires, T. M. (2004). "Induced-charge electrokinetic phenomena: Theory and microfluidic applications." *Phys.Rev.Lett.,* 92(6), 066101.

Bazant, M. Z., and Ben, Y. X. (2006). "Theoretical prediction of fast 3D AC electro-osmotic pumps." *Lab on a Chip,* 6(11), 1455-1461.

Bazant, M. Z., Kilic, M. S., Storey, B. D., and Ajdari, A. (2009a). "Nonlinear electrokinetics at large voltages." *New Journal of Physics,* 11 075016.

Bazant, M. Z., Kilic, M. S., Storey, B. D., and Ajdari, A. (2009b). "Towards an understanding of induced-charge electrokinetics at large applied voltages in concentrated solutions." *Adv.Colloid Interface Sci.,* 152(1-2), 48-88.

Biddiss, E., Erickson, D., and Li, D. Q. (2004). "Heterogeneous surface charge enhanced micromixing for electrokinetic flows." *Anal.Chem.,* 76(11), 3208-3213.

Bilsel, O., Kayatekin, C., Wallace, L. A., and Matthews, C. R. (2005). "A microchannel solution mixer for studying microsecond protein folding reactions." *Rev.Sci.Instrum.,* 76(1), 014302.

Boyden, S. (1962). "Chemotactic Effect of Mixtures of Antibody and Antigen on Polymorphonuclear Leucocytes." *J.Exp.Med.,* 115(3), 453-&.

Brown, A. B. D., Smith, C. G., and Rennie, A. R. (2001). "Pumping of water with ac electric fields applied to asymmetric pairs of microelectrodes." *Physical Review E,* 63(1), 016305.

Burgreen, D., and Nakache, F. R. (1964). "Electrokinetic Flow in Ultrafine Capillary Slits." *J.Phys.Chem.,* 68(5), 1084-&.

Chang, C. C., and Yang, R. J. (2004). "Computational analysis of electrokinetically driven flow mixing in microchannels with patterned blocks." *J Micromech Microengineering,* 14(4), 550-558.

Chang, C. C., and Yang, R. J. (2007). "Electrokinetic mixing in microfluidic systems." *Microfluidics and Nanofluidics,* 3(5), 501-525.

Chang, H. C. (2006). "Electro-kinetics: A viable micro-fluidic platform for miniature diagnostic kits." *Can.J.Chem.Eng.,* 84(2), 146-160.

Chang, H. C. and Yeo, L. (2009), *Electrokinetically Driven Microfluidics and Nanofluidics,* Cambridge University Press, New York.

Chen, C. K., and Cho, C. C. (2007). "Electrokinetically-driven flow mixing in microchannels with wavy surface." *J.Colloid Interface Sci.,* 312(2), 470-480.

Chew, Y. T., Xia, H. M., and Shu, C. (2007). "Fluid micromixing technology and its applications for biological and chemical processes." *3rd Kuala Lumpur International Conference on Biomedical Engineering 2006,* 15 16-20.

Chew, Y. T., Xia, H. M., Shu, C., and Wan, S. Y. M. (2005). "Techniques to enhance fluid micro-mixing and chaotic micromixers." *Modern Physics Letters B,* 19(28-29), 1567-1570.

Coleman, J. T., McKechnie, J., and Sinton, D. (2006). "High-efficiency electrokinetic micromixing through symmetric sequential injection and expansion." *Lab on a Chip,* 6(8), 1033-1039.

Coleman, J. T., and Sinton, D. (2005). "A sequential injection microfluidic mixing strategy." *Microfluidics and Nanofluidics,* 1(4), 319-327.

Craighead, H. (2006). "Future lab-on-a-chip technologies for interrogating individual molecules." *Nature,* 442(7101), 387-393.

Daghighi, Y., and Li, D. (2010). "Induced-charge electrokinetic phenomena." *Microfluidics and Nanofluidics,* 9(4-5), 593-611.

deMello, A. J. (2006). "Control and detection of chemical reactions in microfluidic systems." *Nature,* 442(7101), 394-402.

Dertinger, S. K. W., Chiu, D. T., Jeon, N. L., and Whitesides, G. M. (2001). "Generation of gradients having complex shapes using microfluidic networks." *Anal.Chem.,* 73(6), 1240-1246.

Deval, J., Tabeling, P., and Ho, C. M. (2002). "A dielectrophoretic chaotic mixer." *Fifteenth Ieee International Conference on Micro Electro Mechanical Systems, Technical Digest,* 36-39.

Dittrich, P. S., and Manz, A. (2006). "Lab-on-a-chip: microfluidics in drug discovery." *Nature Reviews Drug Discovery,* 5(3), 210-218.

Dodge, A., Hountondji, A., Jullien, M. C., and Tabeling, P. (2005). "Spatiotemporal resonances in a microfluidic system." *Physical Review E,* 72(5), 056312.

Dukhin, A. S., and Murtsovkin, V. A. (1986). "Pair Interaction of Particles in Electric-Field .2. Influence of Polarization of Double-Layer of Dielectric Particles on their Hydrodynamic Interaction in a Stationary Electric-Field." *Colloid Journal of the Ussr,* 48(2), 203-209.

Erickson, D., and Li, D. Q. (2002). "Influence of surface heterogeneity on electrokinetically driven microfluidic mixing." *Langmuir,* 18(5), 1883-1892.

Feng, J. J., Krishnamoorthy, S., and Sundaram, S. (2007). "Numerical analysis of mixing by electrothermal induced flow in microfluidic systems." *Biomicrofluidics,* 1(2), 024102.

Foxman, E. F., Campbell, J. J., and Butcher, E. C. (1997). "Multistep navigation and the combinatorial control of leukocyte chemotaxis." *J.Cell Biol.,* 139(5), 1349-1360.

Frommelt, T., Kostur, M., Wenzel-Schafer, M., Talkner, P., Hanggi, P., and Wixforth, A. (2008). "Microfluidic mixing via acoustically driven chaotic advection." *Phys.Rev.Lett.,* 1(3), 034502.

Fu, L. M., Yang, R. J., Lin, C. H., and Chien, Y. S. (2005). "Novel microfluidic mixer utilizing electrokinetic driving forces under low switching frequency." *Electrophoresis*, 26(9), 1814-1824.

Fushinobu, K., and Nakata, M. (2005). "An experimental and numerical study of a liquid mixing device for microsystems." *Journal of Electronic Packaging*, 127(2), 141-146.

Gamayunov, N. I., Mantrov, G. I., and Murtsovkin, V. A. (1992). "Study of Flows Induced in the Vicinity of Conducting Particles by an External Electric-Field." *Colloid Journal of the Ussr*, 54(1), 20-23.

Gamayunov, N. I., Murtsovkin, V. A., and Dukhin, A. S. (1986). "Pair Interaction of Particles in Electric-Field .1. Features of Hydrodynamic Interaction of Polarized Particles." *Colloid Journal of the Ussr*, 48(2), 197-203.

Glasgow, I., and Aubry, N. (2003). "Enhancement of microfluidic mixing using time pulsing." *Lab on a Chip*, 3(2), 114-120.

Glasgow, I., Lieber, S., and Aubry, N. (2004). "Parameters influencing pulsed flow mixing in microchannels." *Anal.Chem.*, 76(16), 4825-4832.

Gonzalez, A., Ramos, A., Green, N. G., Castellanos, A., and Morgan, H. (2000a). "Fluid flow induced by nonuniform ac electric fields in electrolytes on microelectrodes. II. A linear double-layer analysis." *Physical Review E*, 61(4), 4019-4028.

Gonzalez, A., Ramos, A., Green, N. G., Castellanos, A., and Morgan, H. (2000b). "Fluid flow induced by nonuniform ac electric fields in electrolytes on microelectrodes. II. A linear double-layer analysis." *Physical Review E*, 61(4), 4019-4028.

Green, N. G., and Morgan, H. (1997). "Dielectrophoretic separation of nano-particles." *Journal of Physics D-Applied Physics*, 30(11), L41-L44.

Green, N. G., Morgan, H., and Milner, J. J. (1997). "Manipulation and trapping of sub-micron bioparticles using dielectrophoresis." *J.Biochem.Biophys.Methods*, 35(2), 89-102.

Green, N. G., Ramos, A., Gonzalez, A., Morgan, H., and Castellanos, A. (2000a). "Fluid flow induced by nonuniform ac electric fields in electrolytes on microelectrodes. I. Experimental measurements." *Physical Review E*, 61(4), 4011-4018.

Green, N. G., Ramos, A., and Morgan, H. (2000b). "Ac electrokinetics: a survey of sub-micrometre particle dynamics." *Journal of Physics D-Applied Physics,* 33(6), 632-641.

Green, N. G., Ramos, A., Gonzalez, A., Morgan, H., and Castellanos, A. (2002a). "Fluid flow induced by nonuniform ac electric fields in electrolytes on microelectrodes. III. Observation of streamlines and numerical simulation." *Physical Review E,* 66(2), 026305.

Green, N. G., Ramos, A., Gonzalez, A., Morgan, H., and Castellanos, A. (2002b). "Fluid flow induced by nonuniform ac electric fields in electrolytes on microelectrodes. III. Observation of streamlines and numerical simulation." *Physical Review E,* 66(2), 026305.

Gregersen, M. M., Olesen, L. H., Brask, A., Hansen, M. F., and Bruus, H. (2007). "Flow reversal at low voltage and low frequency in a microfabricated ac electrokinetic pump." *Physical Review E,* 76(5), 056305.

Gregersen, M. M., Okkels, F., Bazant, M. Z., and Bruus, H. (2009). "Topology and shape optimization of induced-charge electro-osmotic micropumps." *New Journal of Physics,* 11 075019.

Griffiths, S. K., and Nilson, R. H. (2001). "Low dispersion turns and junctions for microchannel systems." *Anal.Chem.,* 73(2), 272-278.

Hadd, A. G., Raymond, D. E., Halliwell, J. W., Jacobson, S. C., and Ramsey, J. M. (1997). "Microchip device for performing enzyme assays." *Anal.Chem.,* 69(17), 3407-3412.

Hardt, S., Drese, K. S., Hessel, V., and Schonfeld, F. (2005). "Passive micromixers for applications in the microreactor and mu TAS fields." *Microfluidics and Nanofluidics,* 1(2), 108-118.

Harnett, C. K., Templeton, J., Dunphy-Guzman, K. A., Senousy, Y. M., and Kanouff, M. P. (2008). "Model based design of a microfluidic mixer driven by induced charge electroosmosis." *Lab on a Chip,* 8(4), 565-572.

Harrison, D. J., Fluri, K., Seiler, K., Fan, Z. H., Effenhauser, C. S., and Manz, A. (1993). "Micromachining a Miniaturized Capillary Electrophoresis-Based Chemical-Analysis System on a Chip." *Science,* 261(5123), 895-897.

Henry, D. C. (1931). "The cataphoresis of suspended particles Part I - The equation of cataphoresis." *Proceedings of the Royal Society of London Series A-Containing Papers of a Mathematical and Physical Character,* 133(821), 106-129.

Hessel, V., Hofmann, C., Lowe, H., Meudt, A., Scherer, S., Schonfeld, F., and Werner, B. (2004). "Selectivity gains and energy savings for the industrial phenyl boronic acid process using micromixer/tubular reactors." *Organic Process Research & Development,* 8(3), 511-523.

Huang, M. Z., Yang, R. J., Tai, C. H., Tsai, C. H., and Fu, L. M. (2006). "Application of electrokinetic instability flow for enhanced micromixing in cross-shaped microchannel." *Biomed.Microdevices,* 8(4), 309-315.

Hunter, R. J. (1981), *Zeta Potential in Colloid Science*, Academic Press, London.

Irimia, D., Geba, D. A., and Toner, M. (2006). "Universal microfluidic gradient generator." *Anal.Chem.,* 78(10), 3472-3477.

Ismagilov, R. F., Stroock, A. D., Kenis, P. J. A., Whitesides, G., and Stone, H. A. (2000). "Experimental and theoretical scaling laws for transverse diffusive broadening in two-phase laminar flows in microchannels." *Appl.Phys.Lett.,* 76(17), 2376-2378.

Jacobson, S. C., McKnight, T. E., and Ramsey, J. M. (1999). "Microfluidic devices for electrokinetically driven parallel and serial mixing." *Anal.Chem.,* 71(20), 4455-4459.

Jacobson, S. C., and Ramsey, J. M. (1997). "Electrokinetic focusing in microfabricated channel structures." *Anal.Chem.,* 69(16), 3212-3217.

Jain, M., and Nandakumar, K. (2010). "Novel index for micromixing characterization and comparative analysis." *Biomicrofluidics,* 4(3), 031101.

Jain, M., Yeung, A., and Nandakumar, K. (2009a). "Efficient Micromixing Using Induced-Charge Electroosmosis." *J Microelectromech Syst,* 18(2), 376-384.

Jain, M., Yeung, A., and Nandakumar, K. (2009b). "Induced charge electro osmotic mixer: Obstacle shape optimization." *Biomicrofluidics,*3, 022413

Jain, M., Yeung, A., and Nandakumar, K. (2010). "Induced charge electro-osmotic concentration gradient generator." *Biomicrofluidics,* 4(1), 014110.

Janasek, D., Franzke, J., and Manz, A. (2006). "Scaling and the design of miniaturized chemical-analysis systems." *Nature,* 442(7101), 374-380.

Jeon, N. L., Baskaran, H., Dertinger, S. K. W., Whitesides, G. M., Van de Water, L., and Toner, M. (2002). "Neutrophil chemotaxis in linear and complex gradients of interleukin-8 formed in a microfabricated device." *Nat.Biotechnol.,* 20(8), 826-830.

Jeon, N. L., Dertinger, S. K. W., Chiu, D. T., Choi, I. S., Stroock, A. D., and Whitesides, G. M. (2000). "Generation of solution and surface gradients using microfluidic systems." *Langmuir,* 16(22), 8311-8316.

Jeong, G. S., Chung, S., Kim, C., and Lee, S. (2010). "Applications of micromixing technology." *Analyst,* 135(3), 460-473.

Johnson, T. J., and Locascio, L. E. (2002). "Characterization and optimization of slanted well designs for microfluidic mixing under electroosmotic flow." *Lab on a Chip,* 2(3), 135-140.

Johnson, T. J., Ross, D., and Locascio, L. E. (2002). "Rapid microfluidic mixing." *Anal.Chem.,* 74(1), 45-51.

Jones, T. B. (1995), *Electromechanics of Particles*, Cambridge University Press, Cambridge.

Kamholz, A. E., Weigl, B. H., Finlayson, B. A., and Yager, P. (1999). "Quantitative analysis of molecular interaction in a microfluidic channel: The T-sensor." *Anal.Chem.,* 71(23), 5340-5347.

Keenan, T. M., and Folch, A. (2008). "Biomolecular gradients in cell culture systems." *Lab Chip,* 8(1), 34-57.

Kutter, J. P., Jacobson, S. C., and Ramsey, J. M. (1997). "Integrated microchip device with electrokinetically controlled solvent mixing for isocratic and gradient elution in micellar electrokinetic chromatography." *Anal.Chem.,* 69(24), 5165-5171.

Lastochkin, D., Zhou, R. H., Wang, P., Ben, Y. X., and Chang, H. C. (2004). "Electrokinetic micropump and micromixer design based on ac faradaic polarization." *J.Appl.Phys.,* 96(3), 1730-1733.

Lee, N. Y., Yamada, M., and Seki, M. (2005). "Development of a passive micromixer based on repeated fluid twisting and flattening, and its application to DNA purification." *Analytical and Bioanalytical Chemistry,* 383(5), 776-782.

Lee, Y. K., Deval, J., Tabeling, P., and Ho, C. M. (2001). "Chaotic mixing in electrokinetically and pressure driven micro flows." *14th Ieee International Conference on Micro Electro Mechanical Systems, Technical Digest,* 483-486.

Levich, V. G. (1962), *Physicochemical Hydrodynamics*, Prentice-Hall, Englewood Cliffs.

Levitan, J. A., Devasenathipathy, S., Studer, V., Ben, Y. X., Thorsen, T., Squires, T. M., and Bazant, M. Z. (2005). "Experimental observation of induced-charge electro-osmosis around a metal wire in a microchannel." *Colloids and Surfaces A-Physicochemical and Engineering Aspects,* 267(1-3), 122-132.

Li, C., Chen, R., and Yang, M. (2007). "Generation of linear and non-linear concentration gradients along microfluidic channel by microtunnel controlled stepwise addition of sample solution." *Lab Chip,* 7(10), 1371-1373.

Li, D. (2004), *Electrokinetics in Microfluidics*, Academic Press, New York.

Lim, C. Y., Lam, Y. C., and Yang, C. (2010). "Mixing enhancement in microfluidic channel with a constriction under periodic electro-osmotic flow." *Biomicrofluidics,* 4(1), 014101.

Lin, H., Storey, B. D., Oddy, M. H., Chen, C. H., and Santiago, J. G. (2004). "Instability of electrokinetic microchannel flows with conductivity gradients." *Phys.Fluids,* 16(6), 1922-1935.

Lin, J. Y., Fu, L. M., and Yang, R. J. (2002). "Numerical simulation of electrokinetic focusing in microfluidic chips." *J Micromech Microengineering,* 12(6), 955-961.

Liu, L., Cao, W., Wu, J., Wen, W., Chang, D. C., and Sheng, P. (2008). "Design and integration of an all-in-one biomicrofluidic chip." *Biomicrofluidics,* 2(3), 034103.

Liu, R. H., Yang, J. N., Lenigk, R., Bonanno, J., and Grodzinski, P. (2004). "Self-contained, fully integrated biochip for sample preparation, polymerase chain reaction amplification, and DNA microarray detection." *Anal.Chem.,* 76(7), 1824-1831.

Liu, R. H., Yang, J. N., Pindera, M. Z., Athavale, M., and Grodzinski, P. (2002). "Bubble-induced acoustic micromixing." *Lab on a Chip,* 2(3), 151-157.

Lyklema, J. (1995), *Fundamentals of Colloid and Interface Science (Vol.2)*, Academic Press, London.

Lynn, N. S., and Dandy, D. S. (2007). "Geometrical optimization of helical flow in grooved micromixers." *Lab on a Chip,* 7(5), 580-587.

Manz, A., and Eijkel, J. C. T. (2001). "Miniaturization and chip technology. What can we expect?" *Pure and Applied Chemistry,* 73(10), 1555-1561.

Manz, A., Harrison, D. J., Verpoorte, E., and Widmer, H. M. (1993). "Planar Chips Technology for Miniaturization of Separation Systems - a Developing Perspective in Chemical Monitoring." *Adv.Chromatogr.,* 33 1-66.

Mao, H. B., Cremer, P. S., and Manson, M. D. (2003). "A sensitive, versatile microfluidic assay for bacterial chemotaxis." *Proc.Natl.Acad.Sci.U.S.A.*, 100(9), 5449-5454.

Masliyah, J. H., and Bhattacharjee, S. (2006), *Electrokinetic and Colloid Transport Phenomena*, John Wiley & Sons, New Jersey.

McDonald, J. C., Duffy, D. C., Anderson, J. R., Chiu, D. T., Wu, H. K., Schueller, O. J. A., and Whitesides, G. M. (2000). "Fabrication of microfluidic systems in poly(dimethylsiloxane)." *Electrophoresis*, 21(1), 27-40.

Ming, G. L., Wong, S. T., Henley, J., Yuan, X. B., Song, H. J., Spitzer, N. C., and Poo, M. M. (2002). "Adaptation in the chemotactic guidance of nerve growth cones." *Nature*, 417(6887), 411-418.

Morgan, H., and Green, N. G. (1997). "Dielectrophoretic manipulation of rod-shaped viral particles." *J.Electrostatics*, 42(3), 279-293.

Mpholo, M., Smith, C. G., and Brown, A. B. D. (2003). "Low voltage plug flow pumping using anisotropic electrode arrays." *Sensors and Actuators B-Chemical*, 92(3), 262-268.

Murtsovkin, V. A. (1996). "Nonlinear flows near polarized disperse particles." *Colloid Journal*, 58(3), 341-349.

Murtsovkin, V. A., and Mantrov, G. I. (1991). "Steady Flows in the Neighborhood of a Drop of Mercury with the Application of a Variable External Electric-Field." *Colloid Journal of the Ussr*, 53(2), 240-244.

Nadal, F., Argoul, F., Kestener, P., Pouligny, B., Ybert, C., and Ajdari, A. (2002). "Electrically induced flows in the vicinity of a dielectric stripe on a conducting plane." *European Physical Journal E*, 9(4), 387-399.

Nagaki, A., Togai, M., Suga, S., Aoki, N., Mae, K., and Yoshida, J. (2005). "Control of extremely fast competitive consecutive reactions using micromixing. Selective Friedel-Crafts aminoalkylation." *J.Am.Chem.Soc.*, 127(33), 11666-11675.

Nguyen, N. T., and Wu, Z. G. (2005). "Micromixers - a review." *J Micromech Microengineering*, 15(2), R1-R16.

Niu, X. Z., and Lee, Y. K. (2003). "Efficient spatial-temporal chaotic mixing in microchannels." *J Micromech Microengineering*, 13(3), 454-462.

Norris, J. V., Evander, M., Horsman-Hall, K. M., Nilsson, J., Laurell, T., and Landers, J. P. (2009). "Acoustic Differential Extraction for Forensic Analysis of Sexual Assault Evidence." *Anal.Chem.,* 81(15), 6089-6095.

Oddy, M. H., Santiago, J. G., and Mikkelsen, J. C. (2001). "Electrokinetic instability micromixing." *Anal.Chem.*, 73(24), 5822-5832.

Okkels, F., and Tabeling, P. (2004). "Spatiotemporal resonances in mixing of open viscous fluids." *Phys.Rev.Lett.,* 92(3), 038301.

Olesen, L. H., Bruus, H., and Ajdari, A. (2006). "ac electrokinetic micropumps: The effect of geometrical confinement, Faradaic current injection, and nonlinear surface capacitance." *Physical Review E,* 73(5), 056313.

Paik, P., Pamula, V. K., and Fair, R. B. (2003a). "Rapid droplet mixers for digital microfluidic systems." *Lab on a Chip,* 3(4), 253-259.

Paik, P., Pamula, V. K., Pollack, M. G., and Fair, R. B. (2003b). "Electrowetting-based droplet mixers for microfluidic systems." *Lab on a Chip,* 3(1), 28-33.

Pascall, A. J., and Squires, T. M. (2010a). "An automated, high-throughput experimental system for induced charge electrokinetics." *Lab on a Chip,* 10(18), 2350-2357.

Pascall, A. J., and Squires, T. M. (2010b). "Induced Charge Electro-osmosis over Controllably Contaminated Electrodes." *Phys.Rev.Lett.,* 104(8), 088301.

Patankar, N. A., and Hu, H. H. (1998). "Numerical simulation of electroosmotic flow." *Anal.Chem.,* 70(9), 1870-1881.

Peigl, L. and Tiller, W. (1997), *The NURBS Book,* Springer-Verlag, New York.

Pethig, R., and Markx, G. H. (1997). "Applications of dielectrophoresis in biotechnology." *Trends Biotechnol.,* 15(10), 426-432.

Pethig, R. (2010). "Review Article-Dielectrophoresis: Status of the theory, technology, and applications." *Biomicrofluidics*, 4(2), 022811.

Pohl, H. A. (1978), *Dielectrophoresis,* Cambridge University Press, Cambridge.

Ramos, A., Gonzalez, A., Castellanos, A., Green, N. G., and Morgan, H. (2003). "Pumping of liquids with ac voltages applied to asymmetric pairs of microelectrodes." *Physical Review E,* 67(5), 056302.

Ramos, A., Morgan, H., Green, N. G., and Castellanos, A. (1999). "AC electric-field-induced fluid flow in microelectrodes." *J.Colloid Interface Sci.,* 217(2), 420-422.

Rice, C. L., and Whitehead, R. (1965). "Electrokinetic Flow in a Narrow Cylindrical Capillary." *J.Phys.Chem.,* 69(11), 4017-4024.

Saadi, W., Wang, S. J., Lin, F., and Jeon, N. L. (2006). "A parallel-gradient microfluidic chamber for quantitative analysis of breast cancer cell chemotaxis." *Biomed.Microdevices,* 8(2), 109-118.

Saintillan, D. (2008). "Nonlinear interactions in electrophoresis of ideally polarizable particles." *Phys.Fluids,* 20(6), 067104.

Saintillan, D., Darve, E., and Shaqfeh, E. S. G. (2006). "Hydrodynamic interactions in the induced-charge electrophoresis of colloidal rod dispersions." *J.Fluid Mech.,* 563 223-259.

Sanders, G. H. W., and Manz, A. (2000). "Chip-based microsystems for genomic and proteomic analysis." *Trac-Trends in Analytical Chemistry,* 19(6), 364-378.

Saville, D. A. (1997). "Electrohydrodynamics: The Taylor-Melcher leaky dielectric model." *Annu.Rev.Fluid Mech.,* 29 27-64.

Schilling, E. A., Kamholz, A. E., and Yager, P. (2002). "Cell lysis and protein extraction in a microfluidic device with detection by a fluorogenic enzyme assay." *Anal.Chem.,* 74(8), 1798-1804.

Sia, S. K., and Whitesides, G. M. (2003). "Microfluidic devices fabricated in poly(dimethylsiloxane) for biological studies." *Electrophoresis,* 24(21), 3563-3576.

Squires, T. M., and Bazant, M. Z. (2004). "Induced-charge electro-osmosis." *J.Fluid Mech.,* 509 217-252.

Squires, T. M., and Quake, S. R. (2005). "Microfluidics: Fluid physics at the nanoliter scale." *Reviews of Modern Physics,* 77(3), 977-1026.

Squires, T. M. (2009). "Induced-charge electrokinetics: fundamental challenges and opportunities." *Lab on a Chip,* 9(17), 2477-2483.

Stone, H. A., and Kim, S. (2001). "Microfluidics: Basic issues, applications, and challenges." *AICHE J.,* 47(6), 1250-1254.

Stone, H. A., Stroock, A. D., and Ajdari, A. (2004). "Engineering flows in small devices: Microfluidics toward a lab-on-a-chip." *Annu.Rev.Fluid Mech.*, 36 381-411.

Stroock, A. D., Dertinger, S. K. W., Ajdari, A., Mezic, I., Stone, H. A., and Whitesides, G. M. (2002). "Chaotic mixer for microchannels." *Science*, 295(5555), 647-651.

Stroock, A. D., Weck, M., Chiu, D. T., Huck, W. T. S., Kenis, P. J. A., Ismagilov, R. F., and Whitesides, G. M. (2000). "Patterning electro-osmotic flow with patterned surface charge." *Phys.Rev.Lett.*, 84(15), 3314-3317.

Stroock, A. D., and Whitesides, G. M. (2003). "Controlling flows in microchannels with patterned surface charge and topography." *Acc.Chem.Res.*, 36(8), 597-604.

Studer, V., Pepin, A., Chen, Y., and Ajdari, A. (2004). "An integrated AC electrokinetic pump in a microfluidic loop for fast and tunable flow control." *Analyst*, 129(10), 944-949.

Studer, V., Pepin, A., Chen, Y., and Ajdari, A. (2002). "Fabrication of microfluidic devices for AC electrokinetic fluid pumping." *Microelectronic Engineering*, 61-2 915-920.

Tabeling, P. (2005), *Introduction to Microfluidics*, Oxford University Press, New York.

Tang, G., Yan, D., Yang, C., Gong, H. Q., Chai, J. C., and Lam, Y. C. (2006). "Assessment of Joule heating and its effects on electroosmotic flow and electrophoretic transport of solutes in microfluidic channels." *Electrophoresis*, 27, 628–639.

Thamida, S. K., and Chang, H. C. (2002). "Nonlinear electrokinetic ejection and entrainment due to polarization at nearly insulated wedges." *Phys.Fluids*, 14(12), 4315-4328.

Thomspon Scientific (2007), [*http://www.esi-topics.com/fmf/2007/september07-MartinZBazant.html*](http://www.esi-topics.com/fmf/2007/september07-MartinZBazant.html)

Tian, F. Z., Li, B. M., and Kwok, D. Y. (2005). "Tradeoff between mixing and transport for electroosmotic flow in heterogeneous microchannels with nonuniform surface potentials." *Langmuir*, 21(3), 1126-1131.

Urbanski, J. P., Levitan, J. A., Burch, D. N., Thorsen, T., and Bazant, M. Z. (2007). "The effect of step height on the performance of three-dimensional ac electro-osmotic microfluidic pumps." *J.Colloid Interface Sci.*, 309(2), 332-341.

Urbanski, J. P., Thorsen, T., Levitan, J. A., and Bazant, M. Z. (2006). "Fast AC electro-osmotic micropumps with nonplanar electrodes." *Appl.Phys.Lett.,* 89(14), 143598.

Walker, G. M., Ozers, M. S., and Beebe, D. J. (2004). "Cell infection within a microfluidic device using virus gradients." *Sens.Actuator B-Chem.,* 98(2-3), 347-355.

Wang, S. C., Chen, H. P., Lee, C. Y., Yu, C. C., and Chang, H. C. (2006). "AC electro-osmotic mixing induced by non-contact external electrodes." *Biosens.Bioelectron.,* 22(4), 563-567.

Wang, Y., Mukherjee, T., and Lin, Q. (2006). "Systematic modeling of microfluidic concentration gradient generators." *J Micromech Microengineering,* 16(10), 2128-2137.

Wen, C., Yeh, C., Tsai, C., and Fu, L. (2009). "Rapid magnetic microfluidic mixer utilizing AC electromagnetic field." *Electrophoresis,* 30(24), 4179-4186.

Whitesides, G. M. (2006). "The origins and the future of microfluidics." *Nature,* 442(7101), 368-373.

Whitesides, G. M., and Stroock, A. D. (2001). "Flexible methods for microfluidics." *Phys Today,* 54(6), 42-48.

Wu, C. H., and Yang, R. J. (2006). "Improving the mixing performance of side channel type micromixers using an optimal voltage control model." *Biomed.Microdevices,* 8(2), 119-131.

Wu, J. (2006). "Biased AC electro-osmosis for on-chip bioparticle processing." *Ieee Transactions on Nanotechnology,* 5(2), 84-89.

Wu, Z., Gao, Y., and Li, D. (2009). "Electrophoretic motion of ideally polarizable particles in a microchannel." *Electrophoresis,* 30(5), 773-781.

Wu, Z., and Li, D. (2008a). "Mixing and flow regulating by induced-charge electrokinetic flow in a microchannel with a pair of conducting triangle hurdles." *Microfluidics and Nanofluidics,* 5(1), 65-76.

Wu, Z., and Li, D. (2008b). "Micromixing using induced-charge electrokinetic flow." *Electrochimica Acta,* 53(19), 5827-5835.

Wu, Z., and Li, D. (2009). "Induced-charge electrophoretic motion of ideally polarizable particles." *Electrochim.Acta,* 54(15), 3960-3967.

Xia, H. M., Wan, S. Y. M., Shu, C., and Chew, Y. T. (2005). "Chaotic micromixers using two-layer crossing channels to exhibit fast mixing at low Reynolds numbers." *Lab on a Chip*, 5(7), 748-755.

Yager, P., Edwards, T., Fu, E., Helton, K., Nelson, K., Tam, M. R., and Weigl, B. H. (2006). "Microfluidic diagnostic technologies for global public health." *Nature*, 442(7101), 412-418.

Yang, R. J., Chang, C. C., Huang, S. B., and Lee, G. B. (2005). "A new focusing model and switching approach for electrokinetic flow inside microchannels." *J Micromech Microengineering*, 15(11), 2141-2148.

Yang, Z., Matsumoto, S., Goto, H., Matsumoto, M., and Maeda, R. (2001). "Ultrasonic micromixer for microfluidic systems." *Sensors and Actuators A-Physical*, 93(3), 266-272.

Yariv, E. (2005). "Induced-charge electrophoresis of nonspherical particles." *Phys.Fluids*, 17(5), 051702.

Yariv, E. (2009). "Boundary-induced electrophoresis of uncharged conducting particles: remote wall approximations." *Proceedings of the Royal Society A-Mathematical Physical and Engineering Sciences*, 465(2103), 709-723.

Yea, K., Lee, S., Kyong, J. B., Choo, J., Lee, E. K., Joo, S. W., and Lee, S. (2005). "Ultra-sensitive trace analysis of cyanide water pollutant in a PDMS microfluidic channel using surface-enhanced Raman spectroscopy." *Analyst*, 130(7), 1009-1011.

Yossifon, G., Frankel, I., and Miloh, T. (2007). "Symmetry breaking in induced-charge electro-osmosis over polarizable spheroids." *Phys.Fluids*, 19(6), 068105.

Yossifon, G., Frankel, I., and Miloh, T. (2006). "On electro-osmotic flows through microchannel junctions." *Phys.Fluids*, 18(11), 117108.

Zhao, H., and Bau, H. H. (2007a). "Microfluidic chaotic stirrer utilizing induced-charge electro-osmosis." *Physical Review E*, 75(6), 066217.

Zhao, H., and Bau, H. H. (2007b). "On the effect of induced electro-osmosis on a cylindrical particle next to a surface." *Langmuir*, 23(7), 4053-4063.

Zicha, D., Dunn, G. A., and Brown, A. F. (1991). "A New Direct-Viewing Chemotaxis Chamber." *J.Cell.Sci.*, 99 769-775.